Technology
Arts Sciences
TH Köln

TH Köln, University for Applied Science
Faculty of Plant, Energy and Machine Systems

DLR

Deutsches Zentrum für Luft- und Raumfahrt e.V.
Institute for Solar Research

Bachelor Thesis

Performance Benchmark of Radiometers for Solar Applications under the Influence of Meteorological Parameters

To achieve the first academic degree Bachelor of Engineering (B.Eng.)

Degree Program: Mechanical Engineering

Felix Maas
Matr.Nr.: 11131764

Cologne, 06.02.2023

This thesis was elaborated at the Institute of Solar Research of the German Aerospace Center (Deutsches Zentrum für Luft- und Raumfahrt e.V., DLR) on the Plataforma Solar de Almería in Tabernas, Spain, and submitted to the University of Applied Science Cologne (TH Köln) in Cologne, Germany.

I hereby declare that I have written the submitted thesis during the reported period of time without outside help and that I have not used any other aids and sources than those indicated.

Felix Maas

Cologne, 06.02.2023 Signature: _____

1st Referee:	Prof. Dr. -Ing. Stefan Benke, TH Köln
2nd Referee:	M.Sc. Niklas Blum, DLR
Date of registration	20.12.2022
Date of submission:	06.02.2023

Acknowledgment

Zunächst möchte ich mich ganz herzlich bei dem Meteorologie Team des DLR für die Möglichkeit bedanken, meine Bachelorarbeit auf der Plataforma Solar de Almería geschrieben haben zu dürfen. Dies war für mich ein absolut einmaliges und unvergessliches Erlebnis. Ein großer Dank gebührt dabei meinem Betreuer Niklas Blum für die über die Maße sehr gute und enge inhaltliche Betreuung. Ich bin äußerst dankbar für seine Denkanstöße, ebenso wie für seine Zeit und Geduld. Aus dem Team des DLR möchte ich mich außerdem bei Sergio Gonzalez Rodriguez, David Muruve Tejada und Rafal Broda für die wertvolle und stetige Unterstützung bedanken.

Für die Zeit während des Studiums richtet sich ein großes Dankeschön zudem an Ulli Sandtner, Tobias Geschonneck, Cristian Karolys sowie Rebecca Tänzer. Persönlich gilt mein Dank aber vor allem meinen Eltern, die während des Studiums immer für mich da waren und mir dieses überhaupt erst ermöglicht haben.

Abstract

Accurate measurements of direct normal irradiance (DNI) and diffuse horizontal irradiance (DHI) are essential for the planning and operation of solar power plants as well as for climate monitoring. The use of Sun trackers in combination with pyranometers and pyrheliometers of the highest quality class according to ISO 9060, currently provides the most accurate data. At the same time, however, this measurement equipment is always associated with high acquisition and maintenance costs. In this thesis, the performance of a total of four radiometers for solar applications is evaluated and the influence of various atmospheric conditions on the measurement accuracy is estimated. The sensors investigated include a rotating shadowband pyranometer (RSP) equipped with an LI-COR 200R, an SPN1 from Delta-T Devices, the comparatively new MS-90 from EKO Instruments Co., Ltd., and the recently developed, camera-based, PyranoCam method from DLR. The study is carried out in a semi-desert climate in Tabernas, Spain. Performance is evaluated using the error metrics RMSD, MAD, BIAS, and the 95% prediction interval (PI_{95}), representative for the measurement uncertainty. The evaluation of the dependence on meteorological influences is done mathematically using Spearman's rank correlation coefficient as well as visually with the help of scatter density plots. For DNI performance under all-sky conditions, the PyranoCam method shows the best results with an RMSD of 3.4% and a MAD of 2.4%. This is followed by the RSP and the MS-90. SPN1 performs worst (RMSD=13.2%, MAD=10.4%). The narrowest PI_{95} can be found for the RSP (-39.2 to 11.4 W/m^2), closely followed by PyranoCam. The widest PI_{95} is between -32 and 140.2 W/m^2 for SPN1. For DHI measurement, RSP shows the smallest RMSD (4.7%) and MAD (3.6%). PyranoCam is in second place. MS-90 shows due to its high RMSD (22.9%) and MAD (14.5%) values the worst results. Here too, RSP provides the narrowest PI_{95} (16.7 to 3.2 W/m^2), once more, followed by PyranoCam. The largest measurement uncertainty occurs when measuring DHI with the MS-90 (-71.4 to 56.2 W/m^2). Regarding the atmospheric dependencies, the PyranoCam method is most strongly influenced by the hourly-averaged DNI clear sky index, which reflects the cloudiness level, in both the DNI and DHI measurements. However, since the cloudiness of the sky has a significant influence on the spectral composition of the radiation, it could be that the overestimation of PyranoCam's DHI is presumably caused by a higher weighting of the solar spectrum in the red region. The RSP shows for both, the DNI and DHI measurement, a moderate dependence on the Sun's elevation angle. While for DNI, the circumsolar radiation affects SPN1's measurement the most, for DHI it is the DNI clear sky index representative for the effective wavelength, which marks the main influence. With respect to the MS-90, circumsolar radiation is the main influence here for the measurement of both DNI and DHI.

Präzise Messungen der direkten normalen Bestrahlungsstärke (DNI) und der diffusen horizontalen Bestrahlungsstärke (DHI) sind sowohl für die Planungssicherheit und den Betrieb von Solarkraftwerken, sowie für die Klimaüberwachung, unerlässlich. Der Einsatz von Sun Trackern, in Kombination mit Pyranometern und einem Pyrheliometer der höchsten Qualitätsklasse nach ISO 9060, liefert derzeit die genauesten Daten. Gleichzeitig sind diese Messapparaturen jedoch auch mit hohen Anschaffungs- und Instandhaltungskosten verbunden. In dieser Thesis wird die Performance von insgesamt vier Radiometern für die solare Anwendungen evaluiert und der Einfluss diverser atmosphärischer Bedingungen auf die Messgenauigkeit abgeschätzt. Bei den untersuchten Sensoren handelt es sich um ein rotierendes Schattenbandpyranometer (RSP) in Kombination mit einem LI-COR 200R, ein SPN1 der Firma Delta-T Devices, das vergleichsweise neue MS-90 des japanischen Unternehmens EKO Instruments Co., Ltd. und das ebenfalls neu entwickelte kamerabasierte PyranoCam-Verfahren des DLR. Die Studie wird im halb-wüsten ähnlichen Klima in Tabernas, Spanien durchgeführt. Die Performance wird dabei anhand der Fehlermetriken RMSD, MAD, BIAS sowie dem 95% Prediction Interval PI_{95} evaluiert, wobei letzteres die Messunsicherheit der Sensoren widerspiegelt. Die Abhängigkeit der Messgenauigkeit von meteorologischen Einflussfaktoren wird einerseits mathematisch auf Basis von Spearman's Rang Korrelationskoeffizienten und andererseits visuelle mit Hilfe von Streudiagrammen bewertet. Hinsichtlich der DNI Performance unter allgemeinen atmosphärischen Bedingungen zeigt die PyranoCam Methode mit einem RMSD von 3.4% und einem MAD von 2.4% die besten Ergebnisse gefolgt vom RSP und dem MS-90. Das SPN1 schneidet am schlechtesten ab (RMSD=13.2%, MAD=10.4%). Die geringste Messunsicherheit liefert das RSP innerhalb eines Intervalls von -39.2 bis 11.4 W/m^2. Knapp dahinter befindet sich PyranoCam. Mit der größten Messunsicherheit zwischen -32 und 140.2 W/m^2 ist bei dem SPN1 zu rechnen. Bezüglich der Messung der diffusen Strahlungskomponente performt das RSP (RMSD = 4.7%, MAD = 3.6%) am besten gefolgt von der PyranoCam Methode. Das MS-90 liefert die schlechtesten Ergebnisse (RMSD = 22.9%, MAD = 14.5%). Die geringste Messunsicherheit wird unter Verwendung des RSP verzeichnet (16.7 to 3.2 W/m^2). Das MS-90 zeigt dagegen mit -71.4 bis 56.2 W/m^2 das größte PI_{95}. Hinsichtlich der Untersuchung der atmosphärischen Abhängigkeiten wird die PyranoCam Methode sowohl bei der DNI als auch bei den DHI Messung am stärksten vom dem DNI Clear Sky Index beeinflusst, der den Bewölkungsgrad repräsentiert. Da die Bewölkung des Himmels jedoch einen erheblichen Einfluss auf die spektrale Zusammensetzung der Strahlung aufweist, ist es möglich, dass die Überschätzung der DHI durch PyranoCam auch durch eine höhere Gewichtung des Sonnenspektrums im roten Bereich verursacht wird. Das RSP zeigt sowohl für die DNI als auch für die DHI Messung eine moderate Abhängigkeit vom Elevationswinkel der Sonne. Während bei der DNI Messung die zirkumsolare Strahlung die Messung des SPN1 am stärksten ablenkt, ist es bei DHI der DNI Clear Sky Index, welcher den Haupteinfluss markiert. Das MS-90 wird für die DNI als auch für die DHI Messung hauptsächlich von der zirkumsolare Strahlung beeinflusst.

Contents

1 Introduction

Accurate, reliable, robust, and, as far as possible, inexpensive measurements of solar irradiation play an essential role in a wide variety of areas, such as:

- Planning and operation of solar power plants and PV (**p**hoto**v**oltaics) systems
- Profitability
- Climate monitoring

For the planning and operation of solar power plants, the evaluation and monitoring of the available solar resource are essential. Concentrating solar power plants, for example, can only convert direct radiation into electricity [1, p.14ff]. In contrast, electrical energy can be generated with the help of photovoltaic modules from diffuse radiation as well as direct radiation. In the photovoltaic sector, in particular, the ratio of diffuse and direct radiation prevailing at the location determines both the choice of semiconductor material and the possibility of using new technologies such as bifacial PV modules [2] [3, p.207ff]. In addition, solar conditions determine whether PV modules track the sun or are fixed at a certain tilt. Tracking promises more energy yield but also increases the measurement, control, and maintenance effort. In order to start up a new production facility, these findings must then be submitted to banks and other lenders to ensure creditworthiness [4]. Another great aspect is that in today's world, where renewable energy plants are expected to provide most of the power in the electrical grid in the long term, predictions of power production become more important than ever for the stabilization of the electrical grids (as discussed in [5]). Accurate real-time forecasts help to better handle the fluctuations caused by sun and wind and prevent possible resulting outages in the electricity supply [6]. Finally, monitoring the global climate system is also an important task for the 21st century. To ensure this, solar radiation was defined as one of the essential climate variables within the framework of the Global Climate Observing System (GCOS) [6]. The current state of the art in terms of solar radiation measurement are so-called Sun trackers, which follow the Sun's path and are always associated with high acquisition and maintenance costs [7]. Additionally, pyrheliometers are far more impacted by soiling than comparable sensors [8]. Alternatives examined in this thesis are characterized by lower costs, simpler and more robust constructions, and low energy consumptions [6] [7].

Hence, a benchmark of these measurement systems at a single site is required. The aim of this work is, therefore, to evaluate and compare a total of four radiometers for solar applications:

- **SPN1** of the British company Delta-T Devices
- **MS-90** from the Japanese manufacturer EKO Instruments Co., Ltd.
- **RSP** (**R**otating **S**hadowband **P**yranometer) equipped with an LI-COR 200R of the homonymous US-American company LI-COR.
- **PyranoCam** as a newly developed measurement method from DLR

and to consider the following two research questions:

1. How do the individual sensors perform against a reference system when applying various deviation metrics?
2. Do the measurement deviations of the individual sensors correlate with various meteorological parameters? If so, which influencing factors affect the sensors most strongly, and to what is this dependence related?

The sensors listed here are selected because they are all in a similar price range and therefore in direct competition with each other. Originally, the CaptPro sensor from the company sunto should also be evaluated. However, this sensor already performed so poorly in the initial phase that it is not considered competitive at this stage.

In the scope of this work, the performance is only evaluated for diffuse and direct irradiation. Of particular interest are the results for the MS-90 as well as for the PyranoCam method, as these have not yet been compared to other radiometers.

The work is structured as follows. Chapter 2 presents the current state of the art. Subsequently, the "Experimental Setup and Data Processing" is explained in Chapter 3. Here, information about the data sets used for the analysis is provided, among others. Chapter 4 includes the performance analysis, and Chapter 5 the correlation analysis. A short discussion is given at the end of both respective Chapters. The findings obtained in this thesis are summarized in Chapter "Conclusion". The work closes with the outlook and the consideration of possible sources of errors in Chapter 7. In order to maintain the flow of reading and the thread within the thesis, some explanations, figures, and tables have been separated into the corresponding chapters in the appendix.

2 State of the Art

At the beginning of Chapter "State of the Art", important basics about solar radiation are discussed. This is followed by the presentation and explanation of the meteorological influences investigated in the "Correlation Analysis and Evaluation". Also essential for this thesis is the knowledge about "Standard Gauges for Solar Irradiance". Since the evaluation results of the later "Performance Analysis and Evaluation" should be compared to previous works and findings, those are presented in the last Section 2.4.

2.1 Fundamentals of Solar Radiation

For a general understanding of solar radiation, its physical background is briefly discussed in the following. Moreover introduced and of particular relevance for this work, are the three different types of radiations on Earth: GHI (**G**lobal **H**orizontal **I**rradiance), DNI (**D**irect **N**ormal **I**rradiance), and DHI (**D**iffuse **H**orizontal **I**rradiance).

Solar radiation is the result of nuclear fusion processes in the Sun and always occurs as an electromagnetic wave or, according to wave-particle duality, as a photon [3, p.71f]. An electromagnetic wave can be characterized by its wavelength λ or by its frequency f, which are related to each other via the speed of light c:

$$c = \lambda * f \tag{2.1}$$

Depending on the wavelength or frequency, electromagnetic waves have a different energy level E_{em} [3, p.193]:

$$E_{em}(\lambda) = h * f = h * \frac{c}{\lambda} \tag{2.2}$$

where h is Planck's constant ($6.63*10^{-34}$ Js). This energy expresses itself in the range of light visible to humans primarily through color: While short wavelengths appear blue, long wavelengths have red color properties (cf. Fig. 2.1). Considering the radiant power density received from the Sun at a certain wavelength gives the so-called solar spectrum as is visualized in dark grey in Fig. 2.1. As shown, the solar spectrum can be divided into the ultraviolet range (≈ 280nm to 380nm), the visible range (≈ 380nm to 780nm) and the infrared range

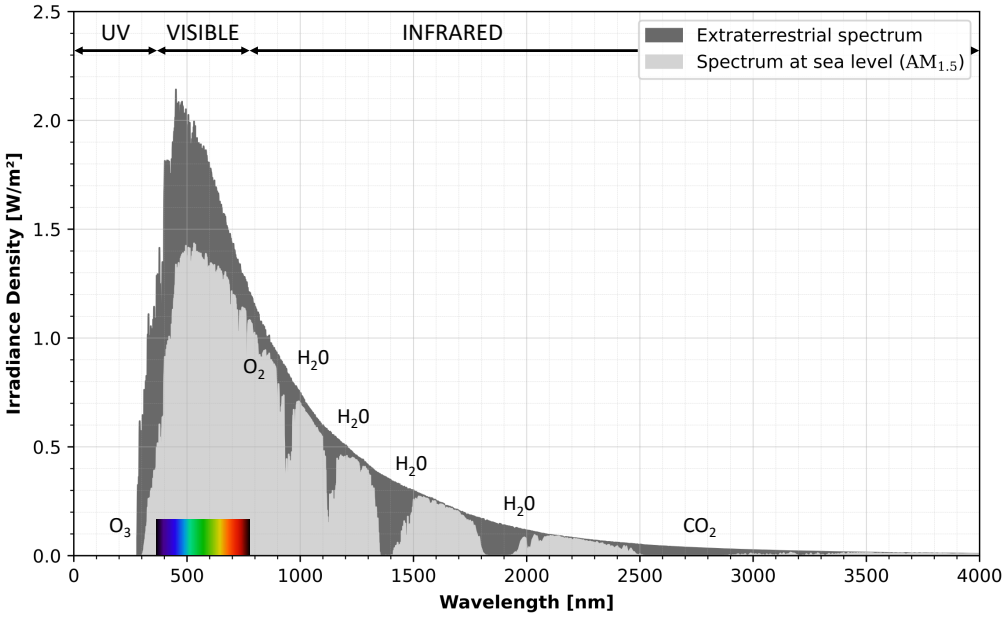

Figure 2.1: Comparison of the solar spectrum inside and outside the atmosphere. In addition to the ultraviolet, infrared, and visible ranges, the regions of absorption by H_2O, O_2, O_3 and CO_2 are also marked. This figure was created by the author himself and inspired by [9, p.7]. The data for the figure were taken from NREL [10]. Furthermore, the visualization of the spectral colors is a graphic taken from DLR [11].

(from ≈ 780nm). It gets obvious, that the spectrum at sea level ($AM_{1.5}$) is different from the extraterrestrial one and thus contains less power [9, p.7ff][1]. The reason for this is absorption, reflection, and scattering by water (H_2O), oxygen (O_2), ozone (O_3), carbon dioxide (CO_2) and dust particles as light travels through the atmosphere to the Earth's surface [12, p.44]. Therefore, from the original 1367 W/m², only about 61% reaches the surface[2]. This fact proves that the natural composition of the atmosphere (about 80% N_2 and 20% O_2) already leads to a significant reduction of the available solar resource. On top of that, not only do the concentration of aerosols and the humidity of the air have a direct influence on the amount of solar energy available, but also influence the spectral composition of the sunlight. This is explained in more depth in Section 2.4. The reduction of solar irradiance density due to scattering can be explained mainly by two phenomena: Rayleigh[3] and Mie[4] scattering. Briefly, Rayleigh scattering is the interaction of light photons with molecular components of air, whose diameter is much smaller than the wavelength of light. In the case of Mie scattering, the opposite is the case. Here, the interaction occurs between light and dust particles whose diameter is larger than the wavelength of light [3, p.75]. These two phenomena are thus mainly responsible for the occurrence of diffuse radiation on the Earth's surface. The diffuse radiation, received by a horizontal surface, is DHI. The direct radiation, received by a

[1] The abbreviation AM stands for air mass and represents the distance radiation has to travel from space to the surface through the atmosphere. A detailed explanation can be found in Appendix A.1
[2] The specification refers to the standardized $AM_{1.5}$ spectrum.
[3] John William Strutt, 3rd Baron Rayleigh (1842-1919), English physicist
[4] Gustav Adolf Feodor Wilhelm Ludwig Mie (1868-1957), German physicist

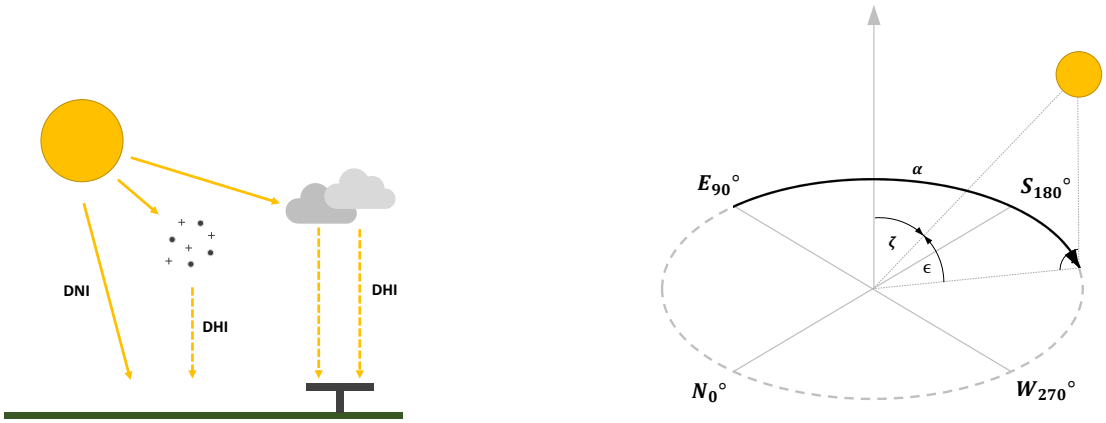

(a) Origin and definition of DNI and DHI

(b) Illustration of Sun's angles

Figure 2.2: Origin and definition of DNI and DHI and illustration of the zenith angle ζ, the elevation angle ϵ, and the azimuth angle α. The zenith and azimuth angles vary depending on longitude, latitude, and time of year. The zenith angle takes values between min. 0° and 90° (Sun at the horizon). The azimuth angle is defined as 90° in the east, 180° in the south, and 270° in the west.

plane perpendicular to the solar disk is called the DNI. Both are illustrated in Fig. 2.2a. The total incident radiation on a horizontal plane is called global horizontal irradiance (GHI). Consequently, GHI results from the combination of DHI and DNI, taking into account the zenith angle ζ of the Sun (visualized in Fig. 2.2b):

$$GHI = DHI + DNI * \cos\zeta \tag{2.3}$$

2.2 Meteorological Parameters of Influence

Based on the results of the literature review, the alternative radiometers are expected to be affected by one or more of the following atmospheric and astronomic parameters:

- Ambient temperature ϑ_{amb}
- Elevation angle ϵ
- Azimuth angle α
- Circumsolar irradiance CSI
- Linke turbidity T_L
- Effective wavelength λ_{eff}
- DNI clear sky index $k_{c,DNI}$

No further explanation is required for the ambient temperature ϑ_{amb}. All other environmental influences are shortly explained in the following sections. To answer the question of why exactly those parameters have been chosen, it can be stated, that...

a) ... some of the parameters are already mentioned as possible influences in the studies [3], [4], [6], [13, p.128ff] and [14], although not analyzed further.

b) ...all parameters affect one of the quality criteria of radiometers according to ISO 9060 [15]. These include errors due to a varying light spectrum, solar elevation, or temperature. The ISO is considered in more detail in Section 2.3.4

2.2.1 Elevation and Azimuth Angle

The elevation angle ϵ and the azimuth angle α are drawn in Fig. 2.2b and represent Sun's spherical polar coordinates. As visible in Fig. 2.3, both change with the date and time, because of Earth's orbit. α and ϵ vary depending on latitude, longitude, and the time of the year.

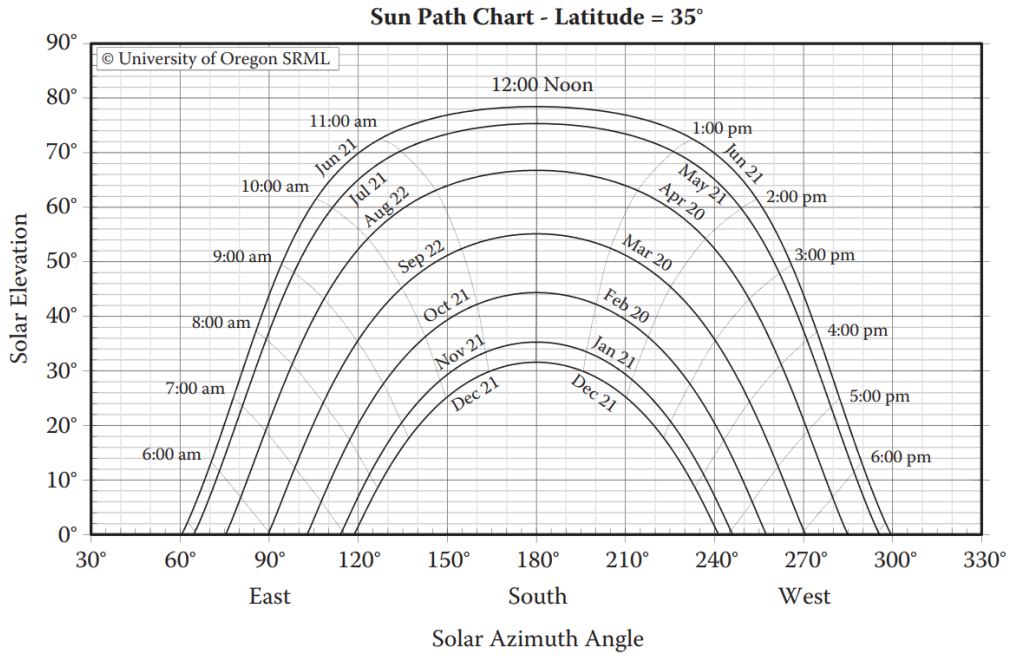

Figure 2.3: Sun path chart for latitude 35°N [9, p.18]

2.2.2 Circumsolar Irradiance

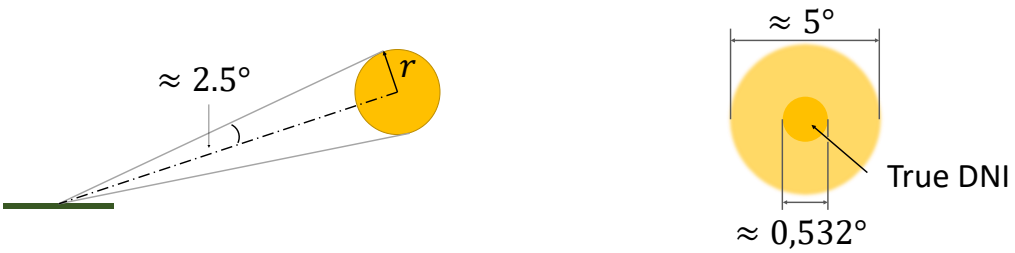

(a) Angular radius of the solar disk

(b) Assumed and actual angular radius

Figure 2.4: Illustration of the assumed angular radius of the solar disk in comparison to its actual size. The difference results from the scattering of the light, when traveling through the atmosphere.

DNI is the part of the radiation, that reaches Earth's surface without scattering (see also Section 2.1 and Fig. 2.2a). According to ISO 9060 [15] and the WMO (**W**orld **M**eteorological **O**rganization) [16], direct radiation is defined as the part of the radiation received within an angular radius of ≈ 2.5° from the center of the solar disk, as depicted in Fig. 2.4a. In fact, however, this value results from the observation of the solar disk on Earth, where its angular diameter, due to the scattering of light in the atmosphere, appears almost 10 times larger than outside the atmosphere (see Fig. 2.4b[5]) [13, p.29f]. Measurements of DNI, thus, include scattered radiation from the angular region near the Sun. This type of radiation is therefore called circumsolar irradiance. That the WMO still specifies an angle of 2.5° has practical reasons: Slight tracking errors are expected because the equipment used for measuring DNI (especially pyrheliometers (cf. Section 2.3.1) must track or follow the Sun's path. Such tracking inaccuracies are less noticeable due to the pyrheliometers' comparatively broad FOV (**F**ield **o**f **V**iew) [13, p.29f]. More information on circumsolar irradiance can be taken from [13, p.143].

[5]Note, that the value of 0.532° is the annual average, and not a constant, which is why the circumsolar irradiance has to be measured, to receive a correct and reliable value.

2.2.3 Linke Turbidity

The Linke turbidity T_L is a measure of the opacity of the sky under cloudless conditions. It represents the number of ideal clean and dry atmospheres, that absorb, reflect, and scatter direct radiation in the same way as an actual, cloudless and soiled atmosphere does. This relationship is demonstrated in simplified form in Fig. 2.5. In the given example, the Linke turbidity factor is T_L=3, since it takes three stacked ideal clean and dry atmospheres to represent a soiled one (Fig. 2.5b). Karl Wilhelm Franz Linke[6] first introduced this factor in [17, p.91-103]. In the present thesis, however, a corrected factor for T_L is used, according to [18]. This corrected factor is independent of the Sun's elevation angle as well as of the air mass. Furthermore, it has also been used in other previous DLR studies such as [19], which investigated the performance of several RSPs.

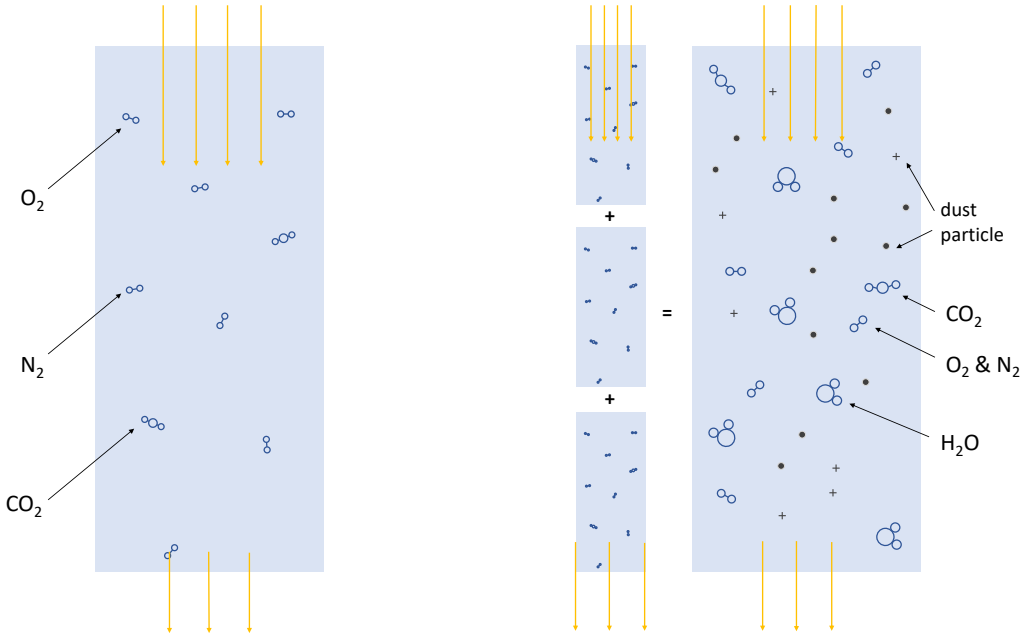

(a) Clear and dry atmosphere, only consisting of N_2, O_2, CO_2 and tracer gases

(b) Actual, cloudless and soiled atmosphere, also consisting of H_2O and dust particle

Figure 2.5: Illustration of the Linke turbidity T_L: An actual, cloudless, and soiled atmosphere represents the number of ideal clean and dry atmospheres, that absorb, reflect, and scatter the radiation in the same way. In this example, the Linke turbidity is T_L=3.

[6] Karl Wilhelm Franz Linke (1878-1944), German geophysicist and meteorologist

2.2.4 Effective Wavelength

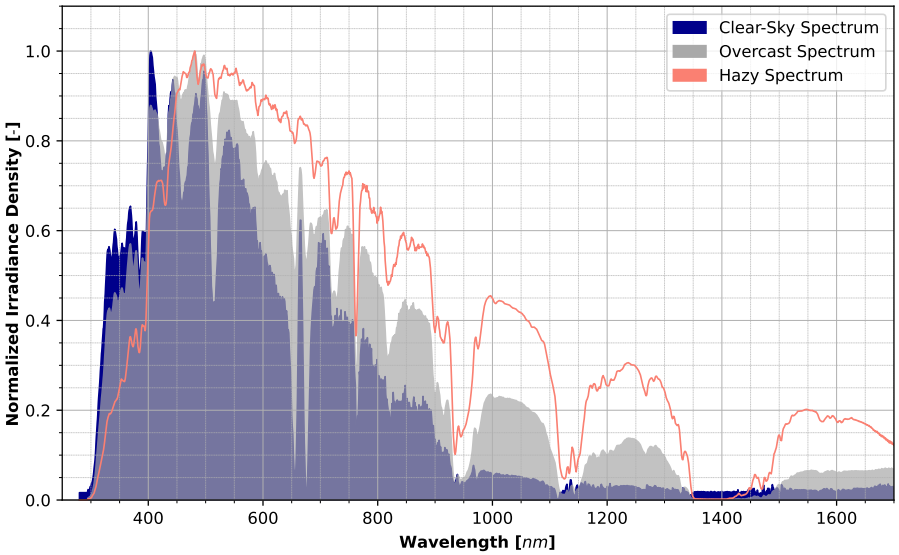

Figure 2.6: Comparison of the DHI solar spectrum for clear-sky, overcast and turbid conditions. The data were recorded in Tabernas, Spain, and normalized for visual comparison. All spectra represent an air mass value of $AM_{1.5}$. The Fig. was created by the author himself, using data from DLR, but inspired by [20].

The $AM_{1.5}$ standard solar spectrum is plotted in Fig. 2.1. Due to different Sun angles and atmospheric conditions, the composition of the light may differ from this standard. As shown in Fig. 2.6, for example, there is a higher weighting of the solar spectrum in the red region for cloudy and especially for hazy sky conditions when considering the diffuse spectrum. [20] provides more detail on this phenomenon. For the data visualized in the above Figure, the atmospheric conditions are shown in the corresponding ASI (**A**ll-**S**ky-**I**mager) photographs in Fig. 2.7. Since the spectrum considered over time is always a two-dimensional matrix consisting of wavelength and time, previous works, such as [21] and [22], reduced the matrix to one dimension, in order to analyze the respective sensors' measurement deviation over a changing spectrum. In accordance with [21, p.8], an effective wavelength can be determined

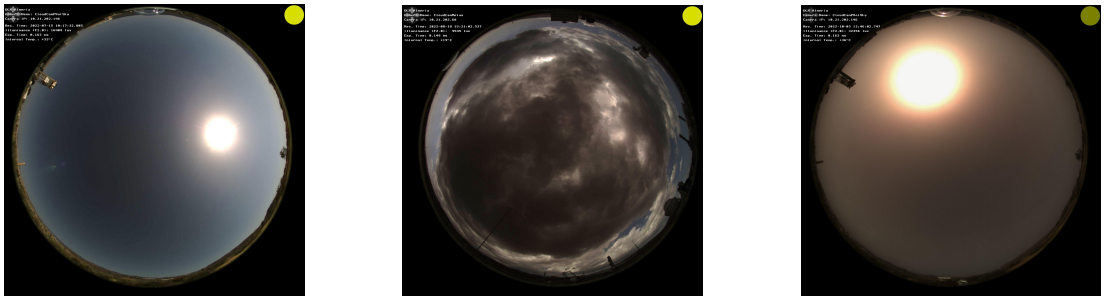

(a) Clear-sky atmosphere **(b)** Overcast atmosphere **(c)** Hazy atmosphere

Figure 2.7: Illustration of a clear-sky, overcast, and hazy atmosphere

for each spectrum at time t_i with:

$$\lambda_{eff,t_i} = \frac{\int_a^b \lambda * E(\lambda) d\lambda}{\int_a^b E(\lambda) d\lambda} \tag{2.4}$$

where a and b indicate the lower and upper wavelength limits of broadband irradiance [15] (a=280nm, b=4000nm), and $E(\lambda)$ is the spectral irradiance for a given wavelength λ. The effective wavelength λ_{eff}, hence, represents the wavelengths' distribution in the solar spectrum in only one scalar.

2.2.5 DNI Clear Sky Index

The DNI Clear Sky Index $k_{c,DNI}$ is the ratio of measured DNI (DNI_{meas}) and theoretical DNI (DNI_{theo}) under clear-sky conditions, depending on the day and Sun's position:

$$k_{c,DNI} = \frac{DNI_{meas}}{DNI_{theo}} \tag{2.5}$$

It takes values between 0 and 1 and hence, represents the degree of cloudiness. The index is used in the work from Schroedter-Homscheidt [5].

2.3 Gauges and Measuring Principles in Solar Applications

This section first gives an overview of the standard measurement devices used in solar applications as well as their quality characteristics. Knowledge of these characteristics is relevant in order to understand the behavior and possible shortcomings of the individual radiometers in the subsequent analyses. The last section then deals with the "Considered and Evaluated Radiometers in this Benchmark" and explains their technical design and physical measurement principles, among others.

2.3.1 Standard Gauges for Solar Irradiance

So-called radiometers are devices designed to measure all types of radiation [13, p.37]. In solar applications, there are mainly two gauges considered to be the standard measurement devices; pyranometers and pyrheliometers. Both sensors have a unique design, which allows them to receive solar radiation from different parts of the sky [13, p.37]. Pyrheliometers[7] are used to measure the DNI, while a pyranometer[8] is designed to measure the GHI or the DHI, depending on the measuring setup. They are usually based on either the photoelectric

[7] Greek terms for measure, Sun, and fire [13, p.37]
[8] Greek terms for measure and fire [13, p.37]

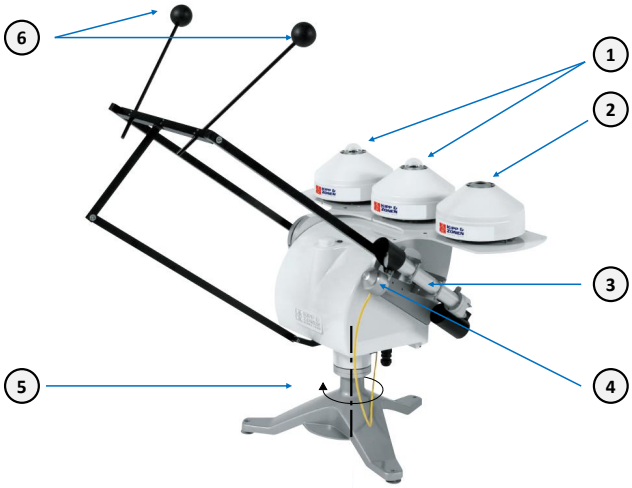

Figure 2.8: Exemplary Sun tracker(Solys-2-Sun-Tracker from Kipp & Zonen): (1) Shaded and unshaded thermopile pyranometer, (2) shaded pyrgeometer, (3) Pyrheliometer, (4) Sun sensor, (5) Vertical rotation axis, (6) Shadow balls. Fig. is taken from [24]

or thermoelectric effect [3, p.103], which will be described down below. Unlike photoelectric radiometers, thermopile sensors have the ability to measure broadband irradiance. They are defined as the radiometers with the highest accuracy according to the WMO [16, p.266] and hence, used in the considered reference system in this study. This reference setup consists of a total of three sensors attached to the sun tracker, which is shown in Fig. 2.8 [23] [24]. Two pyranometers are located at position (1). One of them stays free from shadowing in order to examine GHI, while the other pyranometer is shaded by one of the shadow balls in position (6) in terms of measuring DHI (see Fig. 2.9a and 2.9b). Located in (2) a shaded pyrgeometer can be used for correcting the pyranometers' thermal offsets by gauging longwave irradiance. Pyrgeometers will not be considered in the scope of this study but can be looked up in [13, p.55]. Moreover, detailed information about thermal offsets is given in Appendix A.2.2. Continuing, a pyrheliometer (3) estimates the DNI (see Fig. 2.9c). This is made possible by tracking the Sun with a Sun sensor (4) and by regulating the pyrheliometer's orientation via the vertical rotating axis (5) and the horizontal one, not visible here. It is located directly next to the pyrheliometer and raises or lowers the black strut construction. Thus, the horizontal rotation axis also ensures the correct shadowing of the DHI pyranometer.

As already mentioned above, there exist quality differences for radiometers, which mainly result from the technical design and the physical measuring principle, among other things. Classical radiometers (pyranometers and pyrheliometers) are thus divided into thermopile and silicon sensors. Habte et al. show in their 2016 study, that while certain silicon instruments outperform some thermopile sensors, the best thermopile radiometers perform better than the best silicon instruments overall [4]. Furthermore, acquisition and installation costs, measurement uncertainty, and the availability of resources for maintenance should all be considered [4, p.23]. In the following, the two types of sensors will be presented in more

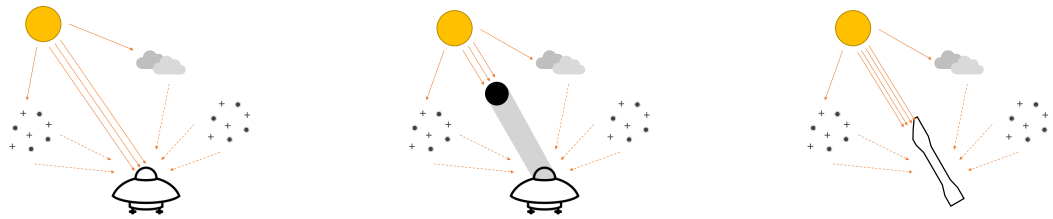

(a) Measuring GHI with an unshaded, static thermopile pyranometer.

(b) Measuring DHI with a shaded, Sun-tracking thermopile pyranometer.

(c) Measuring DNI with a Sun tracking thermopile pyrheliometer.

Figure 2.9: Visualization of the general measurement set up for the determination of GHI, DHI, and DNI

detail. However, technical data and illustrations only provide a rough guide and are not manufacturer-specific. These follow in Section 2.3.5. Please note, that for the sake of convenience, the physical measuring principle and the basic technical design are presented for a pyranometer. However, all explanations can be applied equivalently to a pyrheliometer[9].

2.3.2 Thermopile Sensors

Thermopile sensors are based on the so-called thermoelectric, respectively Seebeck effect. The basic principle is as follows: If two wires of different materials are welded together at one end, a small thermoelectric voltage U_{th} can be measured at the free ends, which increases proportionally to the temperature difference ΔT between the measuring and reference junction: $U_{th} \sim \Delta T$. Such a configuration is also known as a thermocouple [25, p.476f]. For valid and correct measurements, the reference temperature of the junction must be known and kept as constant as possible [25, p.476f]. In thermopile sensors, the thermoelement is located between a thermal receiver and a compensation element (see Fig. 2.10). The thermal receiver corresponds to a black surface, which, imitating an ideal black body, absorbs a wide band of the solar spectrum (280nm to 2800nm) [4, p.22]. The radiation then heats the black surface, which is thermally isolated by two glass domes as shown in Fig. 2.10. A thermocouple on the back of the receiver converts the temperature difference into a voltage signal, for which applies: $U_{th} \sim E_G$, where E_G is the total radiation power. The advantage of this type of sensor is, due to the black surface, a uniform spectral sensitivity over a wide range of wavelengths (Fig. 2.12) and, when leveled correctly, also a nearly constant directional response (see Section A.2.4)[10]. In general, the directional response is the response of the sensor signal to incident

[9] Detailed information about the design and construction of a pyrheliometer can be found in [9, p.72]
[10] Manufacturers also supply suitable correction function on request.

direct radiation at a zenith angle ζ. This makes this sensor more accurate, especially under constant radiation conditions. Moreover, their readings can be adjusted for temperature and thermal offsets (Appendix A.2.2). A disadvantage is the inertia of the sensor. Thus, depending on the design, it can take up to one minute to reach the correct final value [3, p.104], which is a shortcoming, especially under unstable sky conditions.

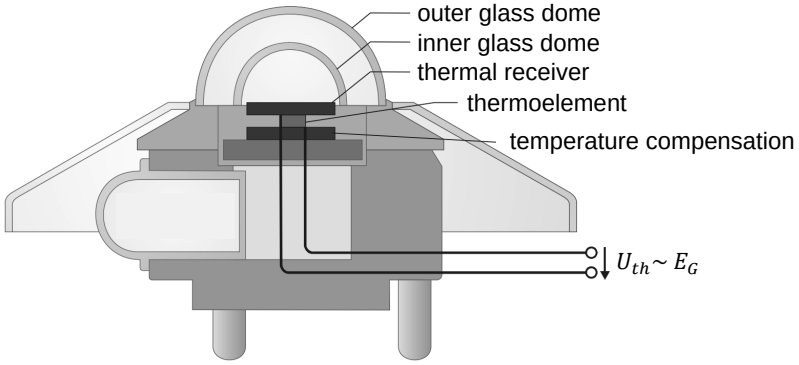

Figure 2.10: General, simplified thermopile sensor design using the example of a pyranometer. The figure was taken from [3, p.103] and the labels translated.

2.3.3 Silicon Sensors

In contrast to thermal sensors, silicon sensors do not provide a temperature-dependent voltage, but a short-circuit current I_{e^-}, which is directly proportional to the incident solar radiation E_G and based on the photoelectric effect[11], which is why they are also called photoelectric sensors [3, p.104]. As the name already suggests, silicon sensors are typically composed of semiconductor materials, just like photovoltaic solar cells. A simplified representation of a silicon sensor is shown in Fig. 2.11. By using a relatively tiny low-impedance shunt and converting the current into a voltage signal, the sensor may be operated close to the short circuit. The sensor temperature should be noted and the observed value afterward modified for accurate readings since semiconductor sensors are likewise sensitive to temperature fluctuations. The measuring current typically rises by $0.15\%/°C$. Since semiconductor materials do not respond to incident spectral radiation of different wavelengths to an identical extent, the result is an inhomogeneous spectral response to only about $\frac{3}{4}$ of the Sun's entire spectrum between 300nm - 1200nm [27, p.3] [4, p.23]. This can be seen in Fig. 2.12 and is known as spectral error. Furthermore, photoelectrical sensors need a diffusor as shown in Fig. 2.11 to ensure well-directional response characteristics, which still cannot match the ones of thermal sensors. A detailed definition of directional response is given in Appendix A.2.4. However, these measurement errors can be corrected to a certain level as, for instance, introduced by

[11] In 1905, the German physicist Albert Einstein discovered that light quanta of certain wavelengths transfer all or part of their energy to the electrons contained in the absorbing material in the form of kinetic energy, resulting in an electric current [26, p.132-148]. This discovery was named the photoelectric effect.

Stefan Wilbert et al. in [19]. Moreover, in comparison, to their competitors, semiconductor materials show the fastest response time (< 1ms), nearly no zero offsets [4, p.23], and cost around 10% of a thermopile sensor [27, p.3].

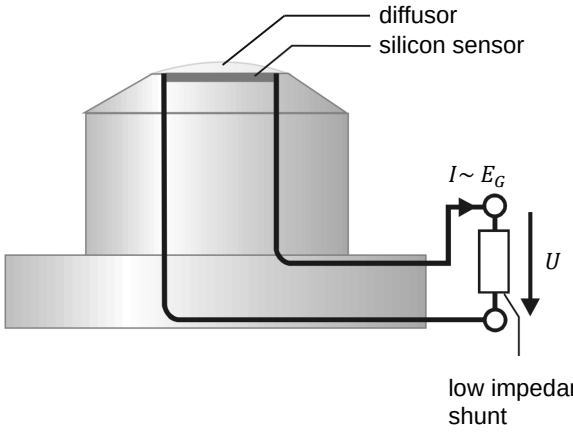

Figure 2.11: General, simplified silicon sensor design using the example of a pyranometer. The figure was taken from [3, p.103] and the labels translated.

2.3.4 Quality Characteristics of Radiometers

Requirements for radiometers for solar applications are defined in ISO 9060 [15]. This standard differentiates between secondary standard, first- and second-class sensors. Secondary standard sensors offer the highest accuracy. However, even in this accuracy class, a measurement uncertainty of ±1 to ±3% is to be expected when determining the daily irradiation [3, p.104]. The criteria by which radiometers are evaluated include:

- Response time
- Zero offset
- Non-Stability
- Non-Linearity
- Directional response
- Spectral error
- Temperature response
- Tilt response
- Additional signal processing errors

Knowledge of the quality properties is therefore important, as they can influence an instrument's performance depending on the atmospheric conditions. A detailed explanation of the individual quality criteria can be found in Appendix A.2.

2.3.5 Considered and Evaluated Radiometers in this Benchmark

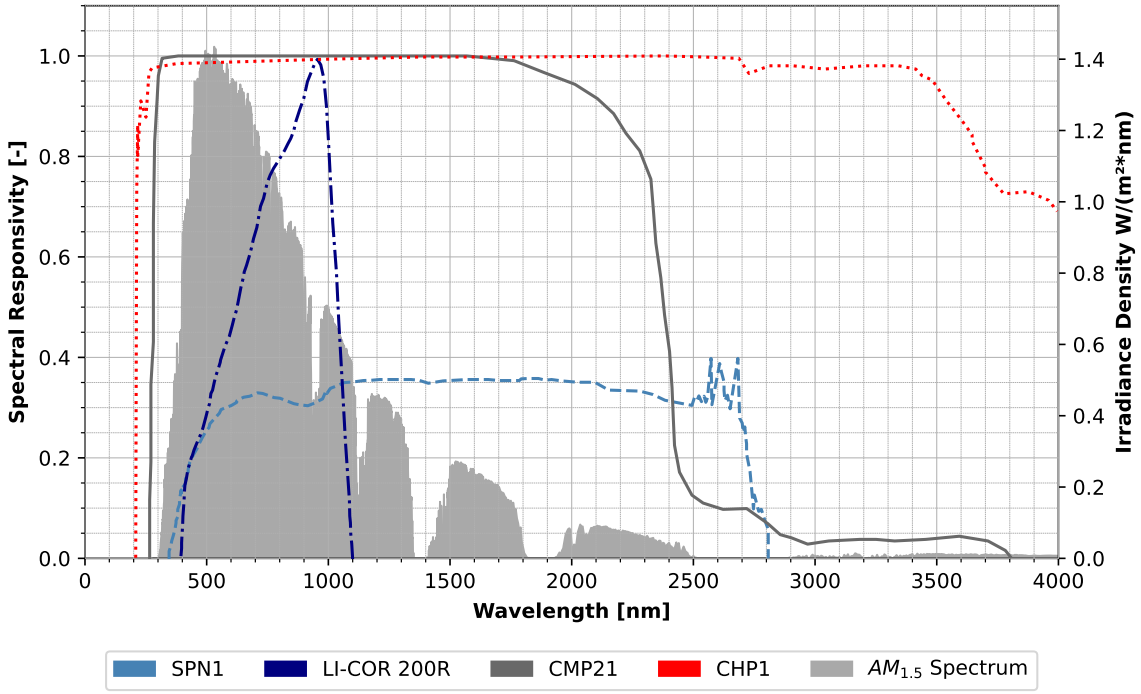

Figure 2.12: Spectral responsivity of the SPN1, LI-COR 200R, CMP21, CHP1, plotted over the $AM_{1.5}$ Spectrum. The data were taken from [28] (SPN1), [29] (LI-COR 200R), [30] (CMP21), [31] (CHP1) and [10] ($AM_{1.5}$).

This section gives an overview of radiometers, promising for solar applications, and considered and evaluated in this benchmark. In general, the technical design and the physical measuring principle are explained. Besides that, the sensors' spectral responses (Fig. 2.12), their compliance with ISO 9060, and other relevant characteristics can be looked up in Table C.1.

Fig. 2.12 shows the spectral response of all considered radiometers in this benchmark over the wavelength. Not included is the MS-90, since no information is available on that. The standard $AM_{1.5}$ spectrum is also shown in grey. This serves as a reference point, as it indicates which irradiation per wavelength is present and what the corresponding response of a sensor is.

2.3.5.1 SPN1

The SPN1 from the British company Delta-T Devices is a static sensor for measuring global and diffuse radiation on a horizontal plane. According to the manufacturer, the SPN1 provides advantages at both big measuring sites and distant sites with little access to maintenance, since it contains no moving parts and requires no orientation over the north. [32, p.3]. As shown in Fig. 2.13, the sensor consists of seven thermocouples in total, which are located in a hexagonal array under a specially shaped shadow mask. The shadow mask is designed in such a way, that:

Figure 2.13: General technical design of Delta-T Devices' SPN1. Image taken from [32, p.3]

- at least one of seven thermocouples is directly irradiated by the Sun and thus measures the incident direct radiation in the horizontal plane plus a part of the diffuse radiation.
- at least one of seven thermocouples is not directly irradiated by the Sun and, thus, measures a fraction of the diffuse radiation.
- all seven thermocouples are irradiated by the diffuse component of the solar irradiance in a nearly equal way [32, p.3].

Therefore the lowest voltage output U_{min} corresponds to half of the actual DHI and the highest voltage output U_{max} corresponds to the DNI in the horizontal plane plus half of the actual DHI:

$$U_{min} \triangleq 0.5 * DHI$$
$$U_{max} \triangleq DNI * \cos(\zeta) + 0.5 * DHI$$

Thus, the three radiation components can be determined as:

$$\begin{aligned} DHI &\triangleq 2 * U_{min} \\ DNI &\triangleq \frac{U_{max} - U_{min}}{\cos(\zeta)} \\ GHI &\triangleq U_{max} + U_{min} \end{aligned} \tag{2.6}$$

Even though SPN1's measurement principle is based on the thermoelectrical effect, it shows a not completely uniform spectral response as illustrated in Fig. 2.12. Rather, it falls stepwise to the shorter wavelengths. With the exception of the so resulting spectral error, which is about ±10% across 400nm to 2700nm, the SPN1 pyranometer equals or surpasses the ISO's requirements for a first-class pyranometer.

2.3.5.2 MS-90

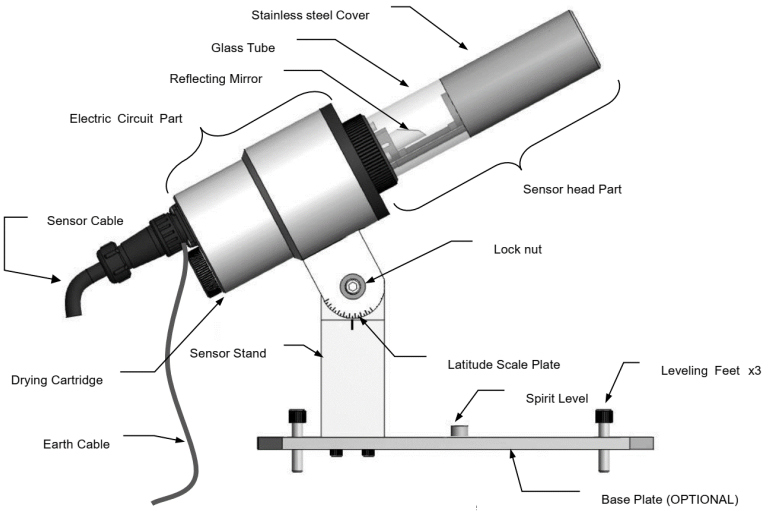

Figure 2.14: General technical design of EKO's MS-90 [33, p.9]

The MS-90 is a DNI sensor from the Japanese manufacturer EKO Instruments Co., Ltd. DNI's estimation is based on the length of sunshine. Like the SPN1 and the RSP, this instrument offers a reasonably inexpensive way to measure direct radiation since it does not require a dynamic tracking system, like the Kipp & Zonen SOLYS-2-Tracker, to align the sensor's aperture with the Sun disk [34]. In combination with any pyranometer for measuring the GHI, the DHI can afterward be calculated. Unlike most common radiometers in the field of solar energy, the MS-90 exploits the pyroelectric effect, which can be looked up in [35, p.69ff; p.627]. Fig. 2.14 illustrates the MS-90's general technical design. Inside the sensor's head part exists a mirror, which rotates with a periodic time of 15s. It is manufactured with diffuse characteristics parallel to its plane of symmetry. DNI is, therefore, measured as the following. If the sun is within the symmetry plane of the mirror, the incident direct radiation is scattered on the mirror and directed to the absorber inside the upper sensor head part. This is the case for a short time in each period. During the rest of the rotation period, diffuse sources of radiation (such as clouds) are located in the symmetry plane. In this case, diffuse radiation falls on the mirror and is directed to the absorber. Both cases are illustrated in Fig. 2.16. Thermal energy is then converted into an electrical voltage signal by the pyroelectrical sensor. The thermoelectric voltage is proportional to the change in thermal energy and consequently, to the change in incident radiation, during the rotation [33, p.14]. Since diffuse radiation also reaches the sensor, while the Sun stays outside the sensor's symmetry plane, EKO uses the convention of the WMO, which defines direct solar radiation only from an irradiance value up from $120\,\mathrm{W/m^2}$ [36]. The according measurement cycle is shown in Fig. 2.15 in a simplified way. Here, the curve's peak corresponds to the second case in Fig. 2.16 and the other way round, the first case belongs to the timestamps, where the curve stays below $120\,\mathrm{W/m^2}$. According to [33, p.14], the final DNI value is then determined

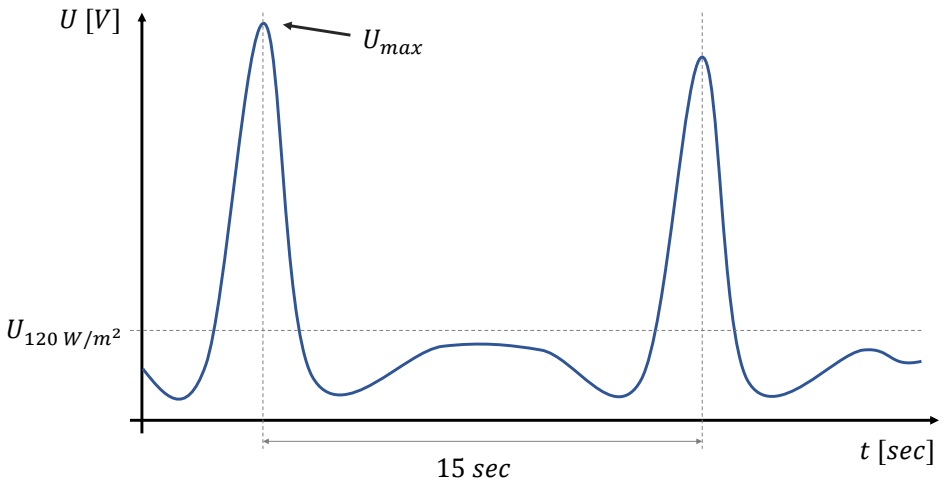

Figure 2.15: MS-90's measurement cycle, illustrated as the output signal over time [34]. Ideally, the curve's peaks correspond to the case, that the Sun is within the mirror's symmetry plane. If this is not the case, the curve stays below 120 W/m². The final DNI value is determined by the maximum output of the measurement signal within one revolution of 15s.

by the maximum output of the measurement signal within one revolution:

$$DNI_j \triangleq \max_{t_i} U_j(t_i) \tag{2.7}$$

where j defines one time period of 15s and i defines a time step within, as recommended by the manufacturer. Unfortunately, EKO does not provide sufficient information about the technical properties, regarding the quality criteria, of the radiometer in [33], [34], [37] or [38]. However, [37] states, that the MS-90's technical design does not meet the requirements of ISO 9060. Based on the measurement principle described, it is clear that the MS-90 can deliver erroneous measurements if the most intense radiation source is not the Sun (cloud enhancement effect), or if there is a high proportion of diffuse radiation from the direct area of the solar disk (and thus within the symmetry plane of the mirror), as is the case with circumsolar radiation. Clouds of a certain kind can increase sunlight by more than 1.5 times when light particles are scattered in optically thin clouds in the close area around the Sun. This is known as the cloud enhancement effect. Based on the speed of the clouds, the bursts might range from seconds to minutes [39].

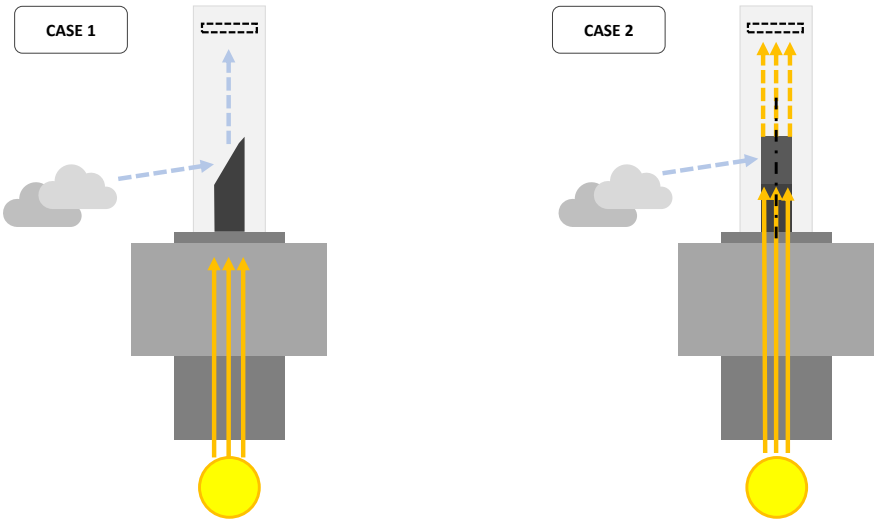

Figure 2.16: Consideration of two possible mirror positions of the MS-90: In case 1, clouds are within the symmetry plane of the mirror - diffuse radiation falls on the mirror and is directed to the sensor. In case 2, the Sun is within the symmetry plane of the mirror - direct radiation falls on the mirror, is scattered there, and is directed to the sensor. The latter one is illustrated by the dashed rectangular.

2.3.5.3 Rotating Shadowband Pyranometer with a LI-COR 200R

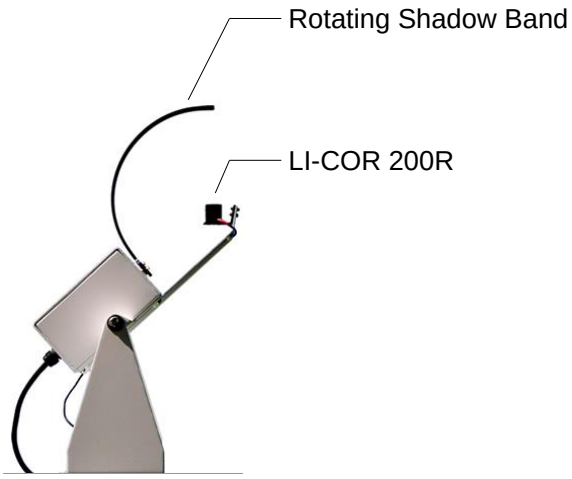

Figure 2.17: General technical design of the RSP in combination with a LI-COR 200R [40].

The RSP is a radiometer, equipped with an LI-COR 200R silicon pyranometer from the USA company LI-COR (Fig. 2.17) and with a periodically rotating shadow band. The physical measuring principle and the technical design of the LI-COR 200R correspond to those already discussed in Section 2.3.3. Within one period, the pyranometer measures consequently the GHI when unshaded (cf. Fig. 2.18 and 2.19a). Once the shadowband starts rotating and the shadow reaches the pyranometer, its output signal drops immediately, due to the fast response time of silicon sensors (cf. Fig. 2.18 and 2.19b). Not only for accurate measurement but also

to prevent an overestimation of the DHI, the fast response time is crucial. The resulting local minimum thus corresponds to the DHI for a period of duration. However, since the shadowband covers more of the hemisphere than it actually should, some corrections have to be applied to the read value [13, p.55ff]. The DNI is subsequently calculated from the DHI and the GHI, by applying Equation 2.3. Due to the unequal spectral sensitivity (see Fig. 2.12), the LI-COR 200R does not meet the requirements of ISO 9060. As has been already stated in Section 2.3.3, silicon sensors require several correction functions to ensure an accurate measurement. Examples of the correction of temperature dependency, spectral, directional, and air mass response are developed and introduced in [19], [41], and [42]. The RSP shown in Fig. 2.17 is a representative of several other concepts with rotating shadowband, which can be found for instance in [13, p.55ff], [43] and [44].

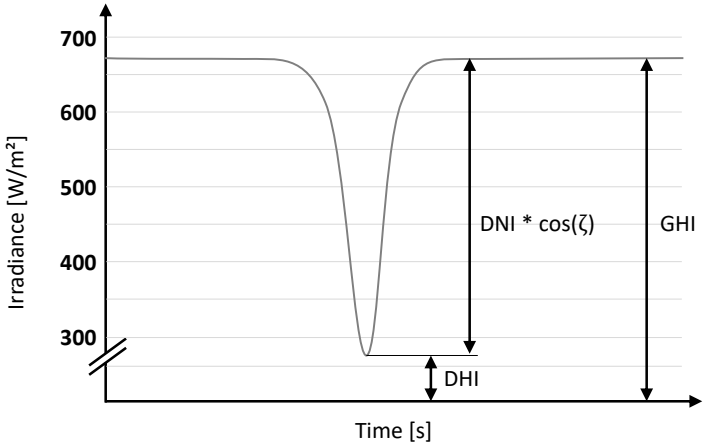

Figure 2.18: RSP's ideal measurement cycle. The shading of the silicon sensor leads to a rapid drop in the measurement signal. The figure was created by the author by inspired by [13, p.57]

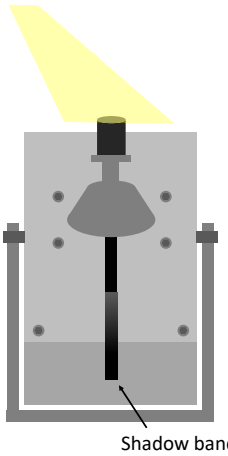

(a) RSP in front view with the shadow band in a neutral position: GHI falls on the LI-COR 200R.

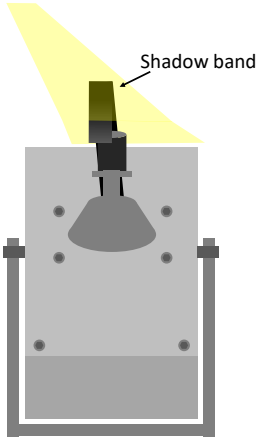

(b) RSP in front view with the shadow band rotating and shading the LI-COR 200R: Only DHI falls on the LI-COR 200R.

Figure 2.19: RSP in front view with the shadow band in **(a)** neutral position and **(b)** in position, where it shades the LI-COR 200R.

2.3.5.4 PyranoCam

Figure 2.20: Illustration of the exemplary set-up of the PyranoCam method, consisting of an all-sky-imager in combination with a secondary standard thermopile pyranometer in a photovoltaic power plant, Photo @ Niklas Blum

DLR's PyranoCam method is based on a combination of an all-sky-imager for estimating DHI and a secondary-standard pyranometer for measuring GHI. Its general setup is shown in Fig. 2.20. In-depth, it is described in [7] and [45]. The all-sky-imager, with a field of view of 180°, takes a photo of the entire sky every 30s (see Fig. 2.7). A physics-based camera model establishes a relationship between the incident radiance and the intensity of the three color channels of the RGB color space. Subsequently, based on the knowledge of the spectral composition of daylight, the broadband irradiance is estimated pixel by pixel. Finally, using knowledge of the camera optics, the sky areas are related to the individual distorted pixels of the ASI image. In simplified terms, the radiance values of the individual pixels are projected into the horizontal plane and integrated to estimate the DHI. The secondary-standard pyranometer measures the GHI, which is used for camera self-calibration and corrections to approximate sky radiance more accurately [7]. Moreover, the accuracy of PyranoCam's measurement is increased by a machine-learning-based correction from [45]. Here, a CNN is trained using transfer and supervised learning. With the help of this correction, PyranoCam's performance can be improved significantly.

2.4 Previous Findings of Sensor Performances

Various studies have been conducted in the past, comparing the performance of radiometers in solar applications. The studies listed in Table 2.1 and briefly explained below are relevant in the context of this work. [14] investigates the SPN1's uncertainties, error sources, and clues for development. Due to the design of the shadow mask and its not perfectly homogenous spectral response (see Fig. 2.12), the SPN1 consistently underestimates the DHI and, thus, overestimates the DNI (cf. Equation 2.6). The reason for this is that SPN1's shadow mask leads to an effective aperture between ±5° and ±25° (depending on Sun's position), in contrast to 2.5°, recommended by the WMO [16]. Hence, a not insignificant large region around the Sun is excluded when measuring DHI but at the same time included when estimating DNI. Therefore, the SPN1 can be expected to be sensible to the influence of circumsolar irradiance. Because of the shortcoming in the spectral response, the SPN1 misses portions of the blue end of the solar spectrum. Under extremely clear skies or at high altitudes, this may result in an underestimation of the diffuse component [14]. Consequently, a dependence on the effective wavelength, respectively the influences that can lead to a stronger weighting of the red or blue part in the spectrum (like the T_L or $k_{c,\,DNI}$), is to be expected. Also visible in [14] is an oscillating curve of the DHI over the azimuth angle. This is explained by the orientation of the sensor over north and occurs for each positioning of the shadow mask since the manufacturer defines no specifications on this.

Within the framework of [6], the performance of SPN1s and RSPs is evaluated. Important findings here are, above all, the confirmation of the results for SPN1 from [14]; It systematically underestimates the DHI and overestimates the DNI, both with a high degree of uncertainty. The RSP's DHI signal shows, moreover, a dependence on the elevation angle ϵ, which according to [6] results from the spectral and directional response. The study [19] proves that the performance of RSPs depends significantly on the quality of the correction functions for these influences. [6] also proposes, in addition, to investigate the dependence of the radiometers on the influence of the spectral composition of the radiation as well as on CSI in a further study. While data in [6] are considered in 1-minute resolution, [4] investigates the performance of SPN1s and RSPs in 10 and 60-minute resolution. Both works are therefore interesting for a quantitative comparison. This not only enables the verification of the experimental procedure in this thesis but also provides conclusions about possible factors influencing the measure-

Table 2.1: Overview of relevant previous works.

Study	Content
[4]	Intercomparison of RSPs and SPN1s, among others
[6]	Performance Evaluation of RSPs and SPN1s
[7]	Introduction and evaluation of the PyranoCam method
[19]	Investigation of the uncertainty of RSPs
[34]	Introduction and evaluation of the MS-90
[45]	Improvement of the PyranoCam method with the help of a machine-learning-based correction
[14]	Determination of SPN1's uncertainties, error sources and clues for development

ment, if the results diverge due to the different climatic conditions (see Chapter 4). [6] and [4] evaluate the sensors' performance by applying the Root-Mean-Squared-Deviation (RMSD), the Mean-Averaged-Deviation (MAD) and the BIAS.

The previous works [34] and [45] give the performance of the PyranoCam method, also using the metrics RMSD and BIAS. Moreover, [45] evaluates qualitatively possible atmospheric influences on accuracy. It states an overestimation of DHI and an increasing dispersion due to the number of saturated pixels. The reasons given for the high degree of saturation are optically thin clouds as well as cloud enhancement effects. Besides that, the influence of the Linke turbidity is given as a reason for the increased measurement deviation in the DHI. However, this is only a qualitative assessment and cannot be confirmed by the corresponding Fig. 5.5b) in his thesis. In addition, only 2 months of data are available for the evaluation of the influences, which clearly limits the reliability of the results. Regarding a later quantitative comparison, it should be noted that these data refer to the same measurement site in Tabernas, Spain, where the benchmark considered in this thesis is conducted. However, the camera was placed in a different location at the site and the sun tracker used for evaluation then is not the same as the one used for this thesis.

Finally, the findings from [34] should be observed at the end of this Section. In the work, the MS-90's deviation from the reference is indicated with a value of ±5% for high elevation angles and high DNI values. This deviation doubles for decreasing DNI values and elevation angles. Thus, an influence of $k_{c,\,DNI}$ or ϵ on the measurement of the DNI can be suspected. Nonetheless, the reliability of [34] is limited due to the small data set.

3 Experimental Setup and Data Processing

Chapter 3 explains first the physical setup of the measuring station in Tabernas, Spain, to ensure the reproducibility of the work. Afterwards, the procedure for data collection and data processing is explained as well as the used filters. Finally, the data sets are presented with regard to their respective properties and the data distributions.

3.1 Physical Setup of the Measuring Station

Table 3.1: Geographical data of the PSA.

Geographical variable	Value
Latitude	7.094° N
Longitude	-2.355° E
Altitude	≈ 500m

The test site is located in Tabernas, Spain, at the PSA (**P**lataforma **S**olar de **A**lmería)[1]. Its geographical data can be taken from Table 3.1. Fig 3.1 shows a drone shot of the test bench at the PSA and the symmetrical arrangement of the relevant sensors at the height of 175cm. They are spaced 50cm apart on the left side of the vertical profile, while on the right side, the distance is 66cm. The spatial arrangement of the sensors on the test bench and the Solys-2-Sun-Tracker is designed so that the sensors do not shade each other. As the daily data checks show, this still happens at certain times. These periods are, as a matter of course, sorted out during the data preprocessing (cf. Section 3.2). The RSP at position (5) protrudes 20cm beyond the horizontal metal profile. An additional height of 13cm is added by the rotating shadow band of the RSP. The thermocouples of the SPN1 (4) and the rotating mirror of the MS-90 (3) are estimated to be 17cm above the test bench construction. The radiometers at positions (1) and (2) are at a distance, where they cannot be shaded at any time of the day and year, and their measurement is affected as little as possible by obstacles, limiting the free field of vision. The site is mostly free of shading obstacles. However, a CSP tower[2], among others, stands at a distance of approximately 132m and a height of 43m [46]. This leads to a critical elevation angle of 18.04°. At this point, it must be mentioned that the pyranometer at position

[1]The PSA is operated and owned by CIEMAT (Centro de Investigaciones Energéticas, Medioambientales y Tecnológicas)

[2]The tower is referred to as SSPS Tower (`https://www.dlr.de/sf/desktopdefault.aspx/tabid-7176/11942_read-28189/`, Accessed on: 01/02/2023)

Table 3.2: Overview of the manufactured characteristic angles for the small and wide shade of the circumsolar measuring setup.

	Small shade	Wide shade
Field of view	2.23° - 2.77°	4.71° - 5.28°
Slope angle	1.37° - 1.90°	3.85° - 4.41°
Limit angle	3.09° - 3.64°	5.56° - 6.14°

(2) was relocated during the ongoing measurements on 05/10/2022 and is henceforth located on the Sun tracker. All sensors are cleaned on a week-daily basis. Position (8) indicates a setup, which allows measuring the circumsolar irradiance. In generalized terms, these are two shaded pyranometers that track the Sun. The characteristic angles of a pyrheliometer, as presented in [47], define the angular range around the Sun in which the radiometer receives radiation. In the construction developed here and shown in Fig 3.2, the specifications of the angles correspond to the reverse case, namely which area of the Sun is shadowed and thus not received by the pyranometers. These are noted in Table 3.2. The upper pyranometer in position (3) in Fig 3.2, thus, has a FOV of ≈ 2.5° and the lower one at position (4) of ≈ 5°, meaning that circumsolar irradiance is measured in a range between both opening angles. For more details regarding the construction, calculation, and plausibility checks of the two signals, see [48]. The ambient temperature and the spectral composition of light are measured at other places on the PSA. While the HygroThermo7419 for temperature reading is located at a distance of ≈ 112m from the test site, two WISER spectroradiometers are at a distance of nearly 840m. An MS711 spectroradiometer measures spectra from 300nm to ≈ 950nm and an MS712 spectroradiometer operates from ≈ 900nm to 1700nm at a wavelength interval of around 0.3nm. Wavelengths between 1700nm - 4000nm are modeled. For more information and technical specifications on the WISERs see [48] and [49]. Used hardware and its settings are summarized in Table 3.3. The reference radiometers have not only a temperature correction but also a physical HVU (**H**eat and **V**entilation **U**nit). All correction functions used for the RSP except spectral corrections are based on [41]. The latter is based on [42].

Table 3.3: Used hardware

Sensor	Logger	Transmission	Sampling Rate	Corrections
CMP21 (GHI)	CR3000	Analog	1s	HVU, Temp.
CMP21 (DHI)	CR3000	Analog	1s	HVU, Temp.
CHP1 (DNI)	CR3000	Analog	1s	HVU, Temp.
SPN1	CR800	Digital	1s	Spectral
MS90	CR800	Analog	15s	-
RSP	CR1000	Analog	1min	For DHI: Temp., Spectral, Air Mass For GHI: Temp., Cosine, Air Mass
Mobotix Q26B-6D	-	Digital	30s	-

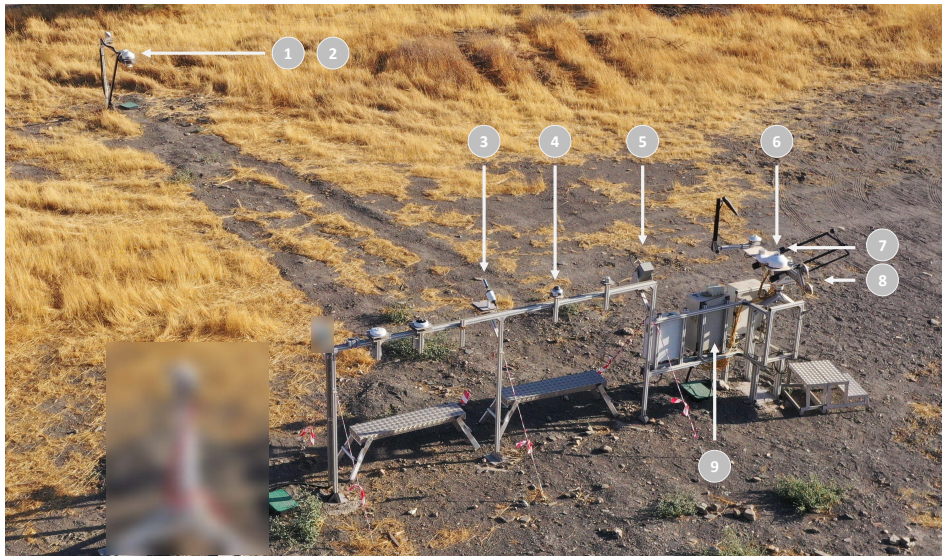

Figure 3.1: Test bench setup at CIEMAT's PSA : (1) PyranoCam ASI, (2) Reference GHI, (3) MS-90, (4) SPN1, (5) RSP with LI-COR 200R, (6) Reference DHI, (7) Reference DNI, (8) Circumsolar radiation measuring setup, (9) Data loggers, Photo @ Niels Algner, DLR.

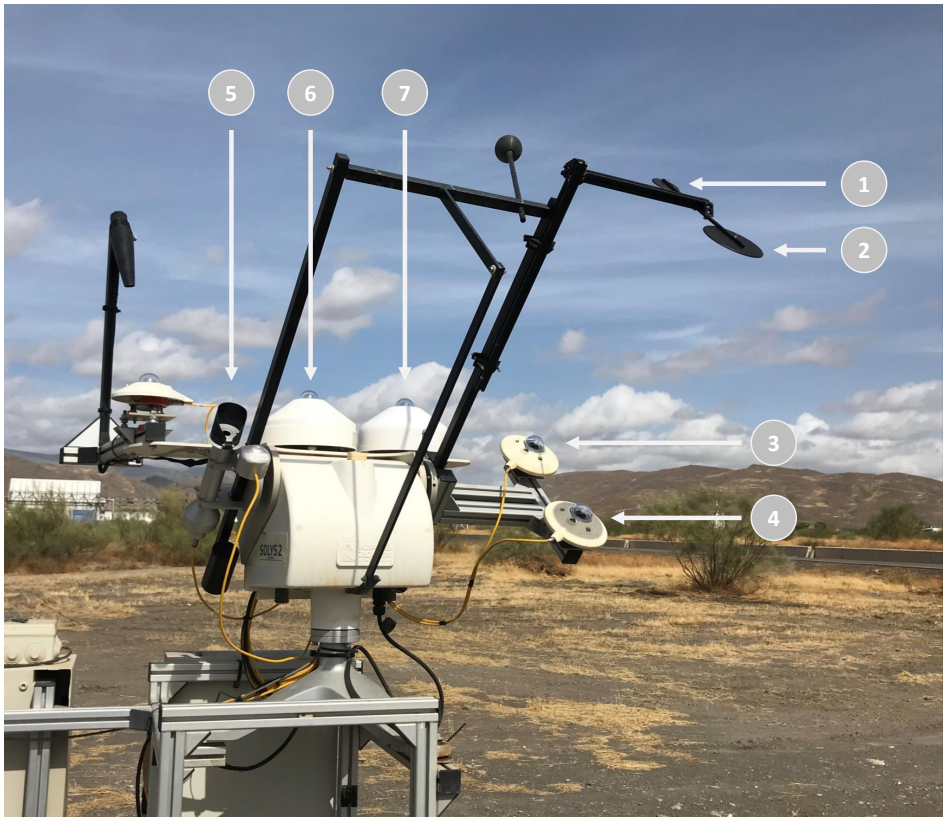

Figure 3.2: Used Sun tracker at the test site at CIEMAT's PSA, extended by the circumsolar irradiance measurement setup in the positions (1) to (4): (1) Small shade, (2) Wide shade, (3) pyranometer with an opening angle of ≈ 2.5°, (4) Pyranometer with an opening angle of ≈ 5°, (5) Pyrheliometer for reference DNI, (6) Pyranometer for reference GHI (moved on the tracker on 05/10/2022), (7) Pyranometer for reference DHI.

3.2 Data Acquisition and Data Preprocessing

The raw data have to be processed and filtered at the first step, in order to receive valid and reproducible data sets. For instance, timestamps, for which...

- ...DHI is greater than GHI,
- ...great negative values are present,
- ...sensor outages appear,

are considered invalid. Moreover, if data, measured at another location on the PSA, are used, then it must be ensured that the weather conditions at both locations are identical at a considered timestamp. Otherwise, the plausibility and reproducibility of the results are not given. The process of filtering is hence explained in Sections 3.2.1.1 to 3.2.1.3. Furthermore, there are several measurands, which are either measured on the test bench and stations nearby or which have to be calculated. Table 3.4 gives an overview of these variables. Their acquisition is explained in Section 3.2.2. Finally, the preparation of the different data sets will subsequently be expounded in Section 3.2.3.

Table 3.4: Additionally measured and calculated variables for the data analysis

Measured Variable	Calculated Variable
Circumsolar irradiance	Elevation Angle
Spectral composition of light	Zenith angle
Ambient temperature	Azimuth Angle
	Linke turbidity
	DNI clear sky index
	Variability Classes

3.2.1 Data Rejection and Filter

To achieve clean data, the following filters are applied: Daily data checks (see Section 3.2.1.1), handling of negative values (Section 3.2.1.2) as well as zenith filter as described in Section 3.2.1.3. In addition, three more filters are set to ensure the plausibility of the data and to exclude illogical time stamps (Section 3.2.1.4). Altogether, the preprocessing explained in this section discards 26.3% of all available data during daylight ($\zeta < 90°$).

3.2.1.1 Daily Data Checks

The data from the sensors and the measuring systems for the meteorological parameters are checked daily both automatically and manually. The requirements and standards for automatic data flagging can be found in [49, p.43ff; p.46ff] and are mainly based on the work of [50]. When checking the data manually, those data are rejected, which show a sensor

outage, shadowing, soiling, persons, or other obstacles such as animals in the ASI's field of view and also periods in which construction or electrical works took place.

3.2.1.2 Handling Negative Values

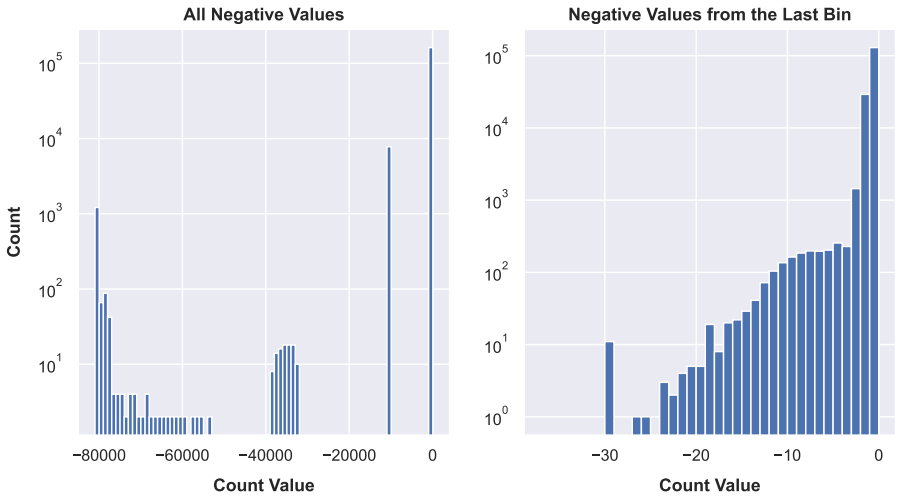

Figure 3.3: Distribution of negative values in the data set. On the left side, the number of negative values is clustered into bins. Since only small negative values might be considered as valid data, the last bin from the left histogram is plotted in high-level resolution on the right side.

Setting all negative values consistently to NaN[3]-values can be problematic. For example, it could be that the true value is 0. Since a sensor can always have both a positive and a negative deviation, it is also possible in this particular case that it outputs a negative value (e.g. -0.2 W/m²) within the scope of its measurement uncertainty. This value is not necessarily wrong. It is therefore important to define an appropriate threshold. Hence, the statistical distribution of the negative values must be considered first and is shown in Fig 3.3. From the distribution, the following can be concluded: Negative readings typically occur with a small magnitude of a few Watts per square meter typically down to - 3 W/m² and some outliers down to -30 W/m². These deviations can result from thermal radiation welling up from the instrument or inconsistent calibrations if an irradiance component is calculated from data from multiple sensors. Further, negative deviations with a much larger magnitude are observed. Those are linked to invalid readings. As these classes are separated, readings of less than -30 W/m² can be connected to invalid readings. Since bins -12 to -4 W/m² have rather similar and low frequencies, a threshold of -3 W/m² is chosen. This means that all data $<$ -3 W/m² are assigned to NaN-values.

[3]NaN = **N**ot **a** **N**umber

3.2.1.3 Zenith Filter

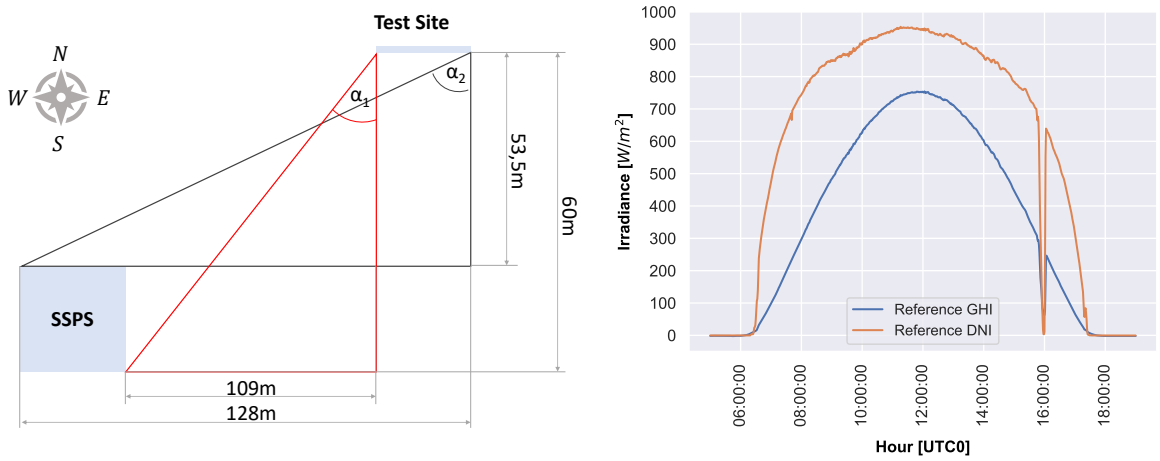

(a) Calculation of the critical azimuth angle range between $[\alpha_1, \alpha_2]$

(b) Shadowing of the reference GHI and DNI by the SSPS tower, on a clear-sky day

Figure 3.4: Determination and visualization of the critical azimuth angle range, in which the SSPS tower shades the test site. The red triangle represents the smallest extreme value of the azimuth angle from which the shadow of the SSPS tower can shade the sensors, depending on the Sun elevation ζ and starting from the right, rear corner. The black triangle represents the largest extreme value of the azimuth angle.

To exclude values at night, timestamps with $\zeta > 90°$ are rejected. Besides that, additional obstacles near the horizon affect the measurements during low Sun elevation, which is why the zenith threshold has to be increased. [30, p.14] suggests 85° for measuring sites, that are not free of obstacles, in general. At PSA, the already introduced SSPS tower stands pretty close to the PyranoCam test bench. As reviewed in Section 3.1, the critical zenith angle is around 72° for an azimuth angle between 241° and 247°. This critical azimuth angle range can be calculated using the site's geometry from Fig 5.7a and verified by identifying the time of shadowing as can be seen in Fig 5.7b. Screening the data for the critical azimuth range, it gets clear, that for the observed time period (01/08/2022 to 11/12/2022), the zenith angle varies between 24.6° and 90°. However, setting the zenith filter to 72° would be fatal, as this would exclude shadow-free periods in both the morning and evening. Timestamps for $\zeta = 72°$ and $\alpha \in [241° ; 247°]$ are, hence, sorted out manually. Besides the correlation analysis, the main purpose of this study is to compare the performance of various sensors with each other and a reference system of thermopile sensors. Since silicon sensors have a very different directional response compared to thermopile sensors [30, p.3], [41, p.3], [42], it is not constructive to exclude the early morning and late evening hours. Therefore, [4], [30] and [45] are taken as reference and a threshold of $\zeta = 85°$ is chosen.

3.2.1.4 Control Plausibility

Even though the automatic and manual data flagging should ensure, that implausible data are rejected, a total of three filters are still added, to guarantee verisimilitude.

1. Detect possible outages by rejecting timestamps where the sensors' GHI, DHI, **and** DNI signal all equal $0\,\mathrm{W/m^2}$ at the same time, even though the reference GHI is greater than $100\,\mathrm{W/m^2}$.
2. Check, whether $\mathrm{GHI_{RSP}} = \mathrm{DHI_{RSP}}$ applies, while $\mathrm{DNI_{Ref}} \geq 100\,\mathrm{W/m^2}$.
3. Make sure that no sensor fails to measure the GHI, DHI, **or** DNI (respective output equals $0\,\mathrm{W/m^2}$), although the respective reference signal reaches a value above $100\,\mathrm{W/m^2}$.

For filter (1) no entries are dropped. For filter (2) the number of rejected data points is 13, and for the third test, 73 entries are dropped for RSP's DNI estimation.

3.2.2 Measured and Calculated Parameters

As given in Table 3.4, the meteorological parameters are either measured or calculated based on other parameters. The following sections are intended to provide a brief overview of how the parameters are obtained.

3.2.2.1 Measuring the Effective Wavelength

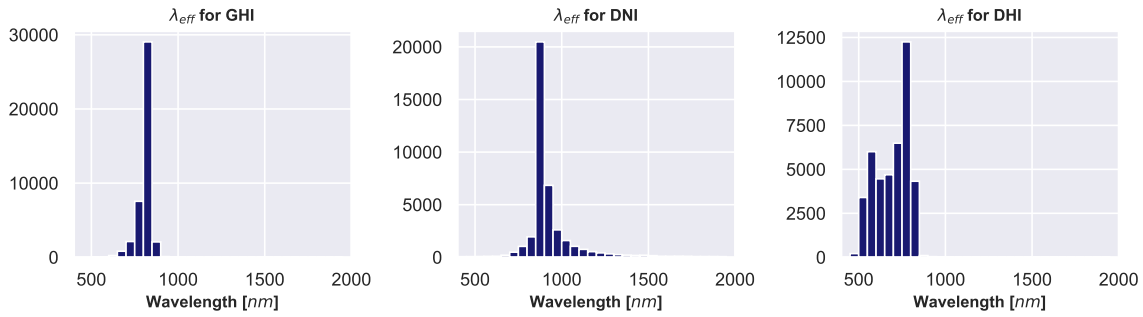

Figure 3.5: Distribution of the effective wavelength for the GHI, DNI, and DHI spectrum. The GHI spectrum is considered in this thesis.

The effective wavelength is calculated using Equation 2.4:

$$\lambda_{eff,t_i} = \frac{\int_a^b \lambda * E(\lambda) d\lambda}{\int_a^b E(\lambda) d\lambda}$$

Due to the large distance between the WISER spectroradiometers and the actual test stand (cf. Section 3.1), moving clouds and thus unstable conditions can produce a problem for the

evaluation. The spectroradiometers might measure a light spectrum influenced by a cloud, while the sensors on the test stand are still (or already again) exposed to clear sky conditions. For this reason, only overcast and clear sky conditions, or in other words stable conditions, will be investigated in the correlation analyses. In line with [6], the conditions at a timestamp are defined as stable if DNI does not change by more than $10\,\mathrm{W/m^2}$ in a 15-minute time window centered around that timestamp. That moving average is also used in the work of Schroedter-Homscheidt et al. [5]. Consequently, the intersection of the valid time stamps for the measurement location of the WISER and the test stand is determined[4]. A total of 45% of the data is thus available for the later correlation analysis. The distribution of the effective wavelength for the GHI, DNI, and DHI spectrum is shown in Fig 3.5. Since both the DNI and DHI signals from the radiometers are examined, the effective wavelength based on the GHI is used. The consideration of the effective wavelength is thus an incontrovertible weak point of this work, as it reduces the data set very strongly, and consequently reduces the significance of the data.

3.2.2.2 Calculating Sun Angles

The elevation, zenith, and azimuth angle are calculated using the `solarposition.getsolarposition` function from the `pvlib` library in Python. Their documentation can be found in [51] and [52].

3.2.2.3 Calculating Variability Classes and Linke Turbidity

In contrast to the Linke turbidity, the so-called variability classes are not explained in Section 2.2, as they are not of interest in the correlation analysis. Nevertheless, they are intended to represent the classification of the data into different weather conditions at the end of this Section 3.2 to ensure the transparency and reproducibility of this work and at the same time to expose potential sources of error. The variability classes are first introduced by [5] and divided into 60-minute windows. They are taken up by [53], where a 15-minute window is applied. In this study, the 60-minute classes are used, because of their better robustness against interferences. However, the calculation for both, the variability classes and the Linke turbidity can be taken from the latter paper. Variability classes result from a 60-minute moving average, similar to the procedure described in Section 3.2.2.1. They are calculated using a 60-minute window centered around the evaluated timestamp. In contrast in [53], the classification of the sky condition into a variability class is based on the past 60 minutes. Table 3.5 contains the respective description for each class.

[4] Another Sun-tracker, similar to the one used in this benchmark, is located at the WISER's site. Its DNI measurements are used for the intersection.

Table 3.5: DNI variability classes according to [53]

Class	Description
1	Clear sky conditions
2	Nearly clear sky conditions
3	Nearly clear sky conditions with a stronger variability and comparatively lower average DNI as in the case of class 2
4	Strong temporal variability but with an overall high average DNI
5	Less variable conditions with a lower average DNI compared to class 4
6	Resembles class 4 with a strong temporal variability, but with a significantly lower average DNI
7	Nearly complete overcast conditions with some ramps
8	Overcast conditions

3.2.2.4 Calculating the Clear Sky Index

The DNI clear sky index $k_{c,\,DNI}$ is calculated according to Equation 2.5:

$$k_{c,DNI} = \frac{DNI_{meas}}{DNI_{theo}}$$

To be congruent to the calculated index in [5], a 60-minute moving average is applied to $k_{c,\,DNI}$, so as to better represent the sky conditions over hourly averages.

3.2.2.5 Calculating Missing Irradiance Signals

The following irradiance signals are not provided by the sensors directly and, thus, have to be calculated, using Equation 2.3:

- DNI for SPN1
- DHI for MS-90
- DNI for PyranoCam

While for the SPN1 both, the GHI and DHI signal is provided from the sensor itself, MS-90 and PyranoCam do not measure GHI and therefore access the reference GHI to calculate the DHI or the DNI, respectively, as it is intended by the developers [7] and [34].

3.2.3 Creation of Data Sets

Since the data for CSI are first available in October 2022, two different time periods have to be evaluated for the performance and the correlation analysis. Furthermore, another problem occurs when calculating relative deviations for small reference readings, since that leads to extreme or even infinite deviation values. To prevent a corresponding distortion of the data, two independent data sets are generated from the original data set for the correlation analysis. One excludes DNI values smaller than 100 W/m^2, when examining the DNI, and another one rejects DHI values smaller than 20 W/m^2, when investigating DHI.

Within the performance analysis, the metric results of the radiometers are evaluated for 1 - minute data. However, 10 - minute and 60 - minute data will also be considered in order to compare them with the results of [4]. To do this in a statistically correct way, it is obligatory just not to average the 1-minute data set to 10 and 60 minutes but to ensure that the same samples are contained in the data sets of all resolutions. Thus, 60-minute windows with less than 60 recordings are rejected from the data set which is used to compare 1, 10, and 60-minute averages. Due to this filter, periods with many short outages are underrepresented. All data points that are not considered in the averaged data set have to be eliminated in the original data set, to avoid any shortcomings. An overview of the time periods and the number of data points used in each data set are given in Table 3.6. Aside from that, the data of the performance analysis show a homogeneous distribution over the hours per day, while the data for the correlation analysis do not. Their distribution is negatively skewed. Also, both data sets exhibit some data gaps due to invalid timestamps. Further details on the statistics of sorted-out values are described in Appendix B.1.

The classification of the data into variability classes is shown in Fig 3.6 for the data set of the performance analysis and in Fig 3.7 for the data set of the correlation analysis. [5] specifies the rules according to which the division is made. Variability classes provide information about the weather conditions represented and allow a better comparison with previous works. Looking at all data sets together first, it can be stated, that they represent variability class 1 (clear sky conditions) with the highest frequency. Classes 2, 5, and 6 are also found in comparatively high numbers. On the other hand, classes 3 and 4 only contain a few data points.

Table 3.6: Time periods and number of data points in each data set

Data Set	Time Period	Number of Data Points
Performance Analysis (1-Minute-Resolution)	01.08.2022 - 11.12.2022	63541
Performance Analysis (1-Minute-Resolution, adjusted)	01.08.2022 - 11.12.2022	27420
Performance Analysis (10-Minute-Resolution, adjusted)	01.08.2022 - 11.12.2022	2742
Performance Analysis (60-Minute-Resolution, adjusted)	01.08.2022 - 11.12.2022	457
Correlation Analysis (no further filtering)	01.10.2022 - 11.12.2022	15409
Correlation Analysis (filtered for DNI $< 100\,W/m^2$)	01.10.2022 - 11.12.2022	11944
Correlation Analysis (filtered for DHI $< 20\,W/m^2$)	01.10.2022 - 11.12.2022	15401

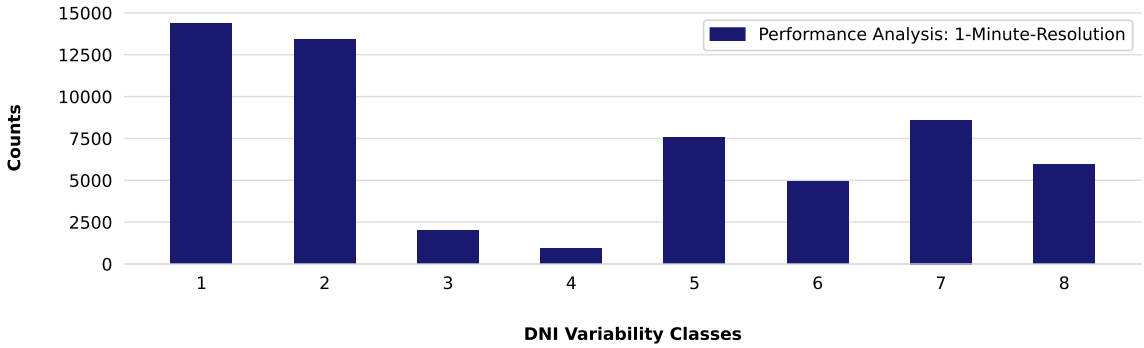

Figure 3.6: Classification of the data for the performance analysis into the variability classes

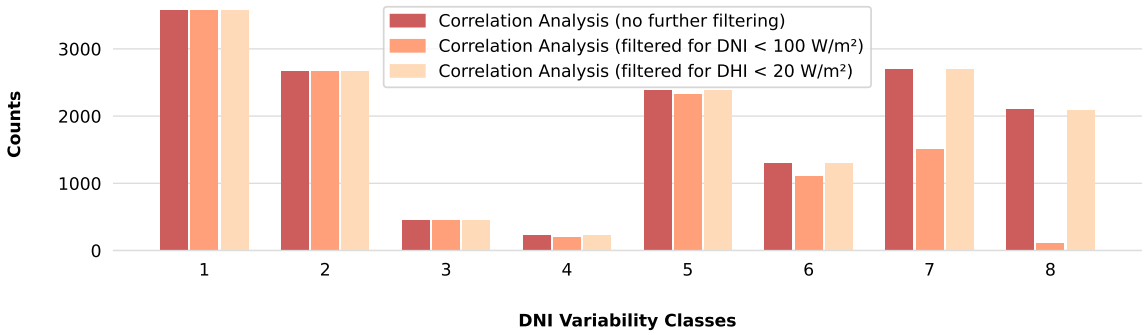

Figure 3.7: Classification of the data for the correlation analysis into the variability classes. Note: Since the variability classes do not play a role in the performance analysis and contain some NaN-values, this Figure only represents 90% of the actual data set. No variability class could be given for the remaining 10%. However, a sufficiently accurate representation of the distribution is assumed.

While for the data set in Fig 3.6, classes 7 and 8 show a moderate frequency comparable to classes 5 and 6, the comparison of the overcast classes' frequencies for DNI and DHI filtered data sets are of particular interest. In contrast to the DNI-filtered data set, the DHI-filtered data set has nearly the same amount of data points in variability classes 7 and 8 as the unfiltered data set for the correlation analysis in Fig 3.7. The DNI-filtered data set does not, as variability classes 7 and 8 mainly represent overcast conditions (see Table 3.5). Finally, the mean radiation values shown in Table 3.7 allow converting percentage data into absolute values if necessary.

Table 3.7: Measured, averaged reference irradiation values in $\mathrm{W/m^2}$ for the respective data sets. The numbering of the data sets corresponds to the chronological order from Table 3.6 from top to bottom.

Data Set	1	2, 3, 4	5	6	7
$\overline{DNI}$	501.0	666.6	503.2	643.4	503.4
$\overline{DHI}$	155.3	153.7	168.4	163.5	168.5

At the end of this chapter, the following should be mentioned: The analysis results shown in this thesis are based on time periods of 4.5 and 2.5 months, respectively. The radiometers are, therefore, not exposed to all weather and climate conditions occurring throughout the year. A more even distribution of the data in Fig 3.6/3.7 across the variability classes can only be expected to a small extent, even over a longer period of time due to the semi-desert climate in Tabernas [54]. Additionally, the variability classes only provide limited conclusions about dusty and cloudy conditions, rainfall, strong winds, and changing temperatures over the year. The angle of elevation and the path of the Sun also changes over the year, as explained in Chapter 2.2.1. Nevertheless, it should be possible to determine a trend in the behavior of the individual sensors, which can then be verified or, if necessary, falsified on an annual data set or at a different location in subsequent works.

4 Performance Analysis and Evaluation

In Chapter 4, the processed data of the individual sensors are analyzed with regard to the research question:

> How do the individual sensors perform against a reference system when applying various deviation metrics?

For evaluation four error metrics are examined.

- RMSD
- MAD
- BIAS
- R^2-score in combination with scatter density plots

In addition, the measurement uncertainty of each sensor is determined empirically using a 95% prediction interval (PI_{95}). The first metric represents the Root-Mean-Squared-Deviation and is calculated as:

$$RMSD = \sqrt{\frac{1}{n} * \sum_{i=1}^{n} (y_i - y_{ref})^2} \tag{4.1}$$

where n corresponds to the sample size, y_i represents the measured sensor value and y_{ref} the measured reference value. The RMSD is a very common and widespread deviation metric in science and is also used in comparable works such as [4], [6], [7], [45], and [14]. Its use, therefore, corresponds to the scientific standard and enables a comparison of the results of the present work with those from Section 2.4. Nevertheless, there is frequent debate in the scientific community about the validity of RMSD and MAD. Latter one's definition is given as:

$$MAD = \frac{1}{n} * \sum_{i=1}^{n} |(y_i - y_{ref})| \tag{4.2}$$

According to [55], when the deviation distribution is anticipated to be Gaussian, the RMSD represents the sensor's performance better than the MAD. At the same time, it can be stated that the RMSD penalizes deviation by giving large outliers more weight than smaller ones, whereas the MAD provides equal weight to all deviations. When computing the RMSD in practice, it may be appropriate to exclude outliers that are many orders bigger than the other samples, especially if the total number of samples is small [55]. In this study, the sample size

is very large. Outliers are rejected as described in Section 3.2. However, some strong outliers might still be present, due to temporal response differences between the devices, performance alterations during regular cleaning activities, and/or incorrect observations for a variety of unidentified causes. Before computing the RMSD, it makes sense to reduce the systematic deviations if the model biases are significant [55]. Systematic deviations are excluded in the initial phase before starting the analysis of the sensor's performance. Still, because the aim of the work is to observe data distribution over the whole data set without manipulating the data, further systematic deviations, resulting from any kind of influence, are not excluded. Any metric only gives one projection of the sensor's variation and, as a result, only draws attention to a certain feature of the deviation characteristics. To evaluate the performance of a radiometer, a variety of metrics is obligatory [55]. However, since the MAD only considers the absolute value of the difference between the test and reference signal, it does not provide information on whether the DNI/DHI tends to be overestimated or underestimated. When evaluating the MAD, it is especially interesting to compare it to the RMSD, since the latter one, as described above, weights larger outliers more heavily than small ones. In the case that $RMSD_i > MAD_i$ it can be assumed that there is an increased number of large outliers for this sensor in the measurement. A metric also considered in many works is the BIAS:

$$BIAS = \frac{1}{n} * \sum_{i=1}^{n}(y_i - y_{ref}) \tag{4.3}$$

In contrast to the MAD, the BIAS tells a lot about whether a sensor tends to underestimate or overestimate the reference measurand on average. The last metric to be examined is the so-called R^2-score. It is calculated according to Equation 4.4 and is a measure of the quality of linear regression when applying a scatter density plot, for instance. It, therefore, represents how exactly the output of a test sensor (y_i) matches that of the reference signal (y_{ref}). The R^2-score is always between 0 (regression is not able to describe any of the variations of y_i) and 1 (perfect regression fit).

$$R^2 = 1 - \frac{\sum(y_{ref} - y_i)^2}{\sum(y_{ref} - \overline{y_{ref}})^2} \tag{4.4}$$

Relative RMSD, MAD, and BIAS are also examined in the scope of this analysis. They are defined by dividing the absolute metric by the mean value of the reference measurement. Exemplary for the rRMSD then applies:

$$rRMSD = \frac{RMSD}{y_{ref}} = \frac{\sqrt{\frac{1}{n} * \sum_{i=1}^{n}(y_i - y_{ref})^2}}{y_{ref}} \tag{4.5}$$

The two subsequent Sections are structured in such a way, that the results of the individual radiometers are described, evaluated, and discussed categorically according to the metrics.

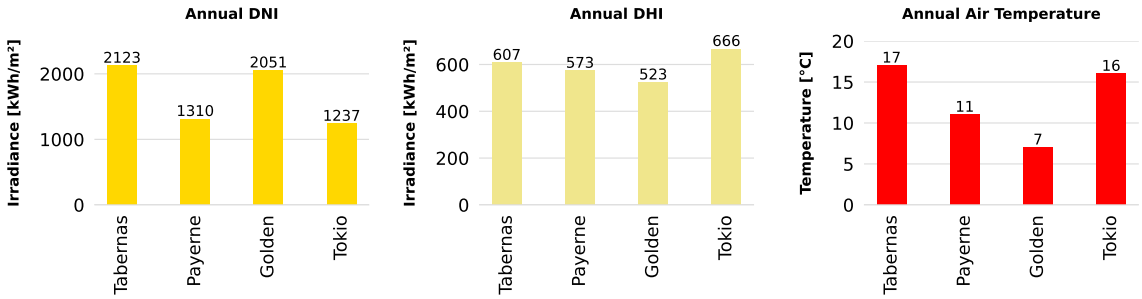

Figure 4.1: Comparison of the annual averages for DNI, DHI, and the ambient temperature for the own test location and those of previous works. Data are taken from [56].

These are then successively related to each other and compared quantitatively with the works from [4], [6], and [45] from previous works. To be taken into account are the different climatic conditions and annual average irradiation values at the various locations of these studies, in comparison to this thesis. The classification according to Köppen & Geiger can be found in Table 4.1. The annual average irradiation values at Tabernas in Spain, Golden in USA [4], Payerne in Switzerland [6], and Tokyo in Japan [34] are plotted in Fig 4.1. It is important to mention, that the values are only intended to provide an idea of the climatic conditions on a qualitative basis, and are in no way suitable for quantitative evaluations. It is assumed that the location in Payerne is characterized atmospherically mainly by a stronger purity and clarity. The number of hours of sunshine per year is also only about half as great in Payerne as in Tabernas, resulting in the corresponding annual DNI (Fig. 4.1). Hence, the hypothesis is made, that the performance of the RSP and the SPN1 in Tabernas are more similar to the favorable conditions from [6] than to the all-sky conditions. The same applies to the location in Golden, where less haze can be expected on average due to the immensely differing climate conditions. Simultaneously, however, the irradiation sums over the year for DNI are relatively similar to the ones in Tabernas. Thus, a stronger similarity from this thesis' results to the ones from [4] for all-sky conditions is expected here. Comparisons are repeatedly made with both data sets from [6] and [4] in the respective Sections. Besides the fact that differences in the performance results indicate artifacts or external influences in the measurements, a quantitative comparison also serves to verify the measurement's plausibility.

Based on the explanations given above, two principles of interpretation apply to the following evaluations of the metrics:

Table 4.1: Climatic classification of the previous works' locations, according to Köppen & Geiger [54]

Site	Climatic Classification	Meaning
Tabernas	Csa	Warm temperature, summer dry, hot summer
Payerne	Cfb	Warm temperature, fully humid, warm summer
Golden	Dfc	Snow, fully humid, cool summer
Tokyo	Cfa	Warm temperature, fully humid, hot summer

1. The ratio of MAD and RMSD provides information about the number of large outliers within a distribution of measured values. Hence, a large proportion of the MAD to the RMSD does not mean that there is little dispersion, but rather that the number of large outliers is small in relation to the actual dispersion width.

2. The BIAS provides information on whether the DNI and DHI signal tends to be underestimated or overestimated over the entire data set. Moreover, the absolute value of the BIAS in relation to the MAD serves to estimate the strength of the dispersion, since the BIAS itself always has a certain share in the MAD. For example, a sensor that consistently underestimates the measurement signal, but otherwise does not show a strong dispersion, is characterized by an almost identically large BIAS and MAD.

4.1 Evaluation and Interpretation of the DNI Performance for 1-Minute-Resolution

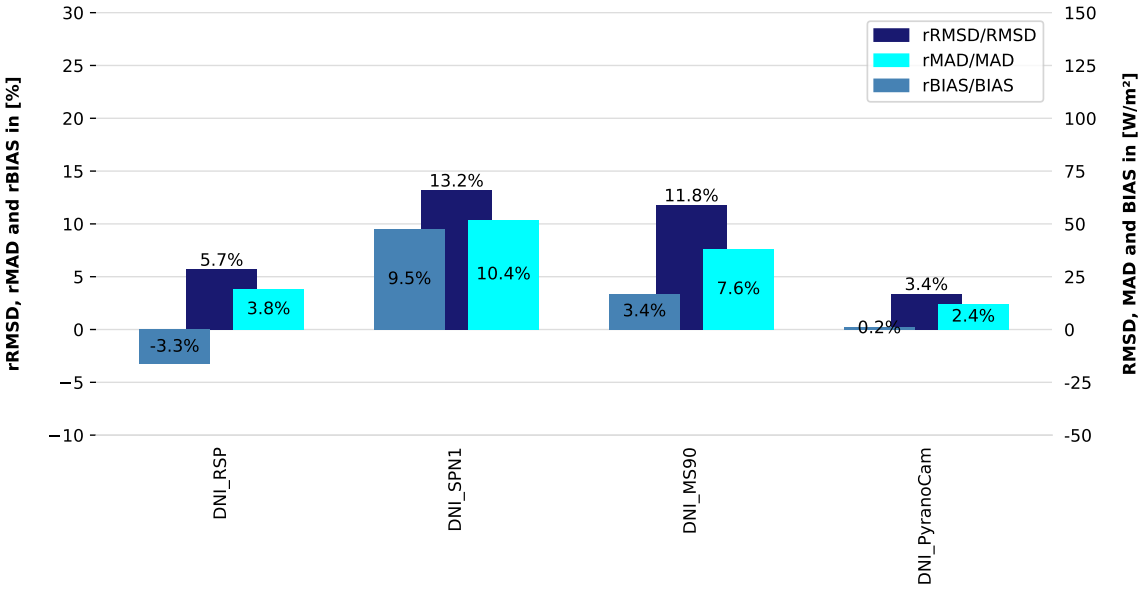

Figure 4.2: Comparison of RMSD, MAD, and BIAS for DNI in 1-minute resolution. The relative scale is attached on the left side, and the absolute scale is on the right side.

Fig 4.2 compares the RMSD, MAD, and BIAS of the tested radiometers for DNI, based on the data set "Performance Analysis (1-Minute-Resolution)" from Table 3.6. Table 4.2 represents the findings quantitatively from [6] and [45]. The value ranges given are caused by the fact that, unlike in the present study, [6] did not examine only one RSP or SPN1, but several radiometers of the same type. The specified range of values thus extends from the lowest to the highest value determined in [6]. Moreover, in Table 4.2 favorable conditions are understood as periods in which the DNI varies by less than 10 W/m² within a 15-minute window [6].

Both the RMSD and MAD initially show the following ranking in terms of sensor accuracy, starting with the sensor of the smallest deviation:

1. PyranoCam
2. RSP
3. MS-90
4. SPN1

The PyranoCam method delivers a relatively low RMSD value of 17.1 W/m² (3.4%). Broda finds a value of 13.2 W/m² (2.4%) in his analysis [45] (cf. Table 4.2). Both values are in the same range. Furthermore, the RMSD and MAD differ moderately (70%), so even though a greatly high number of large outliers is not present in the corresponding scatter density plot in Fig 4.5, a few data points are far outside the actual scatter range. For the PyranoCam method, the BIAS is almost 0 W/m² (0.9 W/m², 0.2%). That indicates, that PyranoCam shows neither under- nor overestimating of the true value and the low MAD (2.4%), hence, results only from the dispersion of the measured values around the reference. Fig 4.5 confirms this interpretation, as there is no deviation of the data points from the angle bisector visible. In [45] a BIAS of 7.7 W/m² (1.4%) is given (cf. Table 4.2). Without applying the machine learning model it is 0.2%, according to the initial paper from [7]. Looking at the scatter density plot, there are two trends visible between 400 and 600 W/m², where the PyranoCam method underestimates DNI strongly, and between 200 and 350 W/m², where the opposite is the case. This is visualized in Fig. 4.3 and 4.7. It is possible to identify which days are responsible for the over- and underestimation. The respective ASI images from these days are given in Fig 4.4a and 4.4b. On both days there are special occurrences: Red clouds on the afternoon of 08/09/2022 (leads to an underestimation of PyranoCam's DNI) and strong turbidity on 03/10/2022 (leads to an overestimation of PyranoCam's DNI). Thus, it can be assumed that the PyranoCam method, which has not yet been fully analyzed, probably has a not insignificant sensitivity to the spectral composition of the light and the opacity of the atmosphere. Whether such a correlation exists is evaluated in the correlation analysis in Chapter 5.

Table 4.2: Results from [6] and [45] for DNI in 1-Minute Resolution. For [6], the values for the expanded uncertainty are calculated within a 99.3% interval. Favorable conditions are understood as periods in which the DNI varies by less than 10 W/m² within a 15-minute window.

	All-Sky Conditions [6]		Favorable Conditions [6]		All-Sky Conditions [45]
	RSP	SPN1	RSP	SPN1	PyranoCam
RMSD	22 - 30	45	12 - 28	31 - 37	13.2
MAD	12 - 20	58	10 - 25	30	n.a.
BIAS	-15	40	-20	20 - 25	7.7
Expanded Uncertainty	±40	-45 - 125	-55 - 40	30 - 120	n.a.

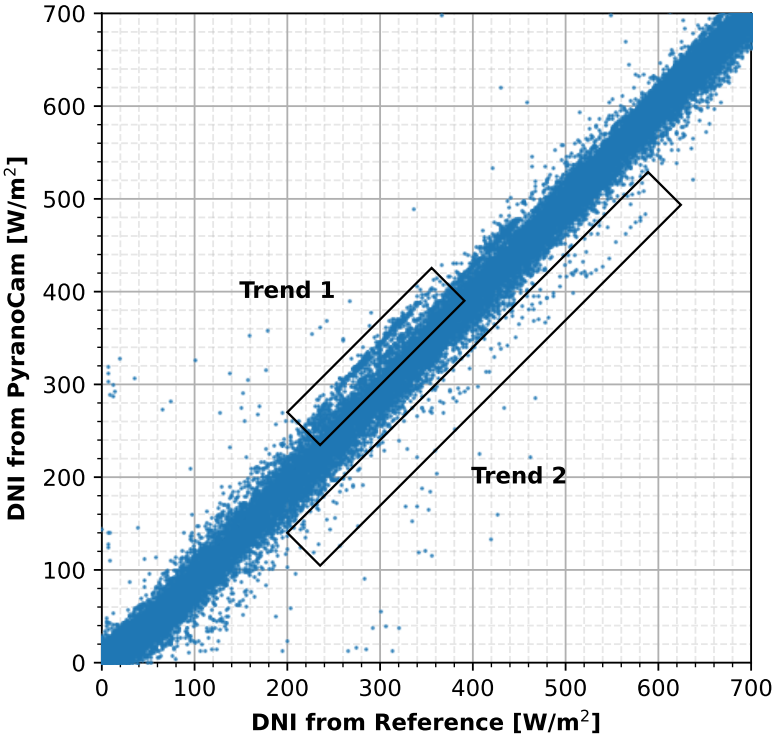

Figure 4.3: Visualization of the trends in PyranoCam's DNI measurement

For the RSP, the RMSD is 28.8 W/m², which corresponds to a relative value of 5.7%. In Payerne [6], the rotating shadowband pyranometer showed an RMSD of around 22 - 30 W/m² for all-sky conditions and 12 - 28 W/m² for favorable conditions. The value determined here, therefore, fits in both ranges. This indicates, that the measurement of DNI with the RSP, thus, appears to be largely independent of climatic differences between the two sites, at least for the RMSD. The MAD with a value of 5.7 W/m² (3.8%) differs strongly from the RMSD (MAD/RMSD = 66%), resulting in a not inconsiderable amount of large outliers in Fig 4.5. Its MAD lies between the two given respective ranges from [6], recorded in Table 4.2. Considering the RSP's BIAS, with an absolute value of -16.7 W/m² (-3.3%), it almost equals the MAD, which on the one hand indicates, that the RSP underestimates the DNI signal on average and on the other hand, that its MAD for the largest part results from that. A rather small dispersion can, hence, be observed in Fig 4.5, while the majority of data points are located below the dashed angle bisector. In [6] the RSP shows a BIAS around -15 W/m² for all-sky conditions and a BIAS around -20 W/m² for favorable conditions.

When looking at the result for the MS-90, a relatively high RMSD value of 59 W/m² (11.8%) is found. Since the MAD only accounts for about 64% of the RMSD (cf. Fig 4.2), a high number of large outliers take place in the respective scatter density plot in Fig 4.5. This plot also indicates that the distribution of the data points has a rightward sloping curve that is above the bisector for low to medium irradiance values and below the bisector for high irradiance values. Another interesting point to compare with Pó's work is the R^2-score. The MS-90,

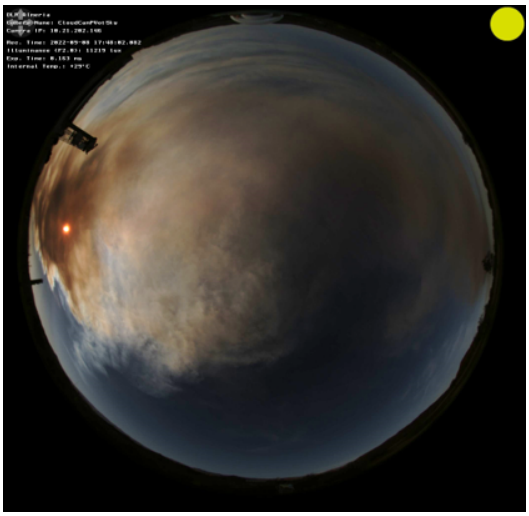

(a) Underestimation on 08/09/2022 due to red clouds on the afternoon for DNI

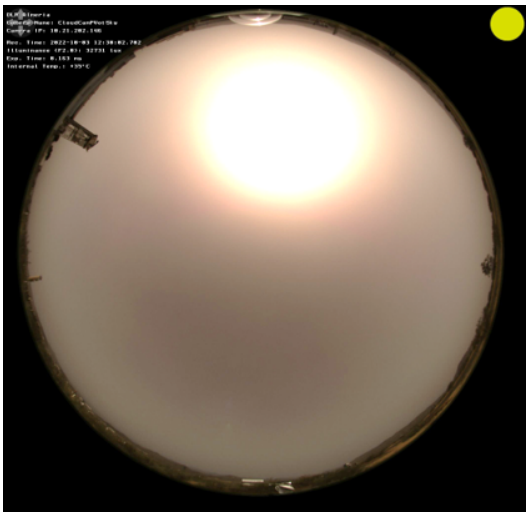

(b) Overestimation on 03/10/2022 due to high turbidity for DNI

Figure 4.4: The photographs of the all-sky-imager provide the explanation for the trends in Fig 4.3, where PyranoCam's DNI is overestimated and underestimated, respectively

located in Tokyo, achieves a value of 0.9766, whereas in Tabernas only an accuracy of 0.969 is achieved. The correlation analysis should provide more insight into which meteorological factor influences the DNI measurement of the MS-90 most strongly, and whether this is more pronounced in Tabernas than in Tokyo. This could explain the poorer performance of the DNI sensor studied here. Finally, MS-90's BIAS (3.4%) is about half of its MAD (7.5%). The sensor, hence, overestimates DNI on average, which, however, does not fully explain the MAD.

The evaluation of the SPN1 remains. Its RMSD (66.1 W/m^2, 13.2 %) and MAD (52.2 W/m^2, 10.4%) underlie the MS-90's one. Thus, this sensor performed the worst in the measurement of DNI of all those examined here. Compared to [6], where the SPN1s exhibit RMSDs around 45 W/m^2 for all-sky conditions and around 31 - 37 W/m^2 for favorable conditions, it is noticeable that the value obtained in this study is clearly above the two value ranges but closer to the all-sky conditions data set. Although such high values for the RMSD and MAD are determined for the SPN1, the scatter density plot (Fig 4.2) shows only a small number of large outliers, as the ratio of MAD and RMSD is 78%. However, judging by the magnitude of MAD and BIAS (47.5 W/m^2, 9.5%), SPN1 overestimates DNI in a very strong way. At this point, too, the SPN1 exhibits similar behavior for MAD and BIAS to this one from [6] under all-sky conditions (cf. Table 4.2), different from what was assumed in the hypothesis at the beginning. Similar to the MS-90, there seems to be an atmospheric condition present in Tabernas, which does not appear in Payerne, or at least not to this extent.

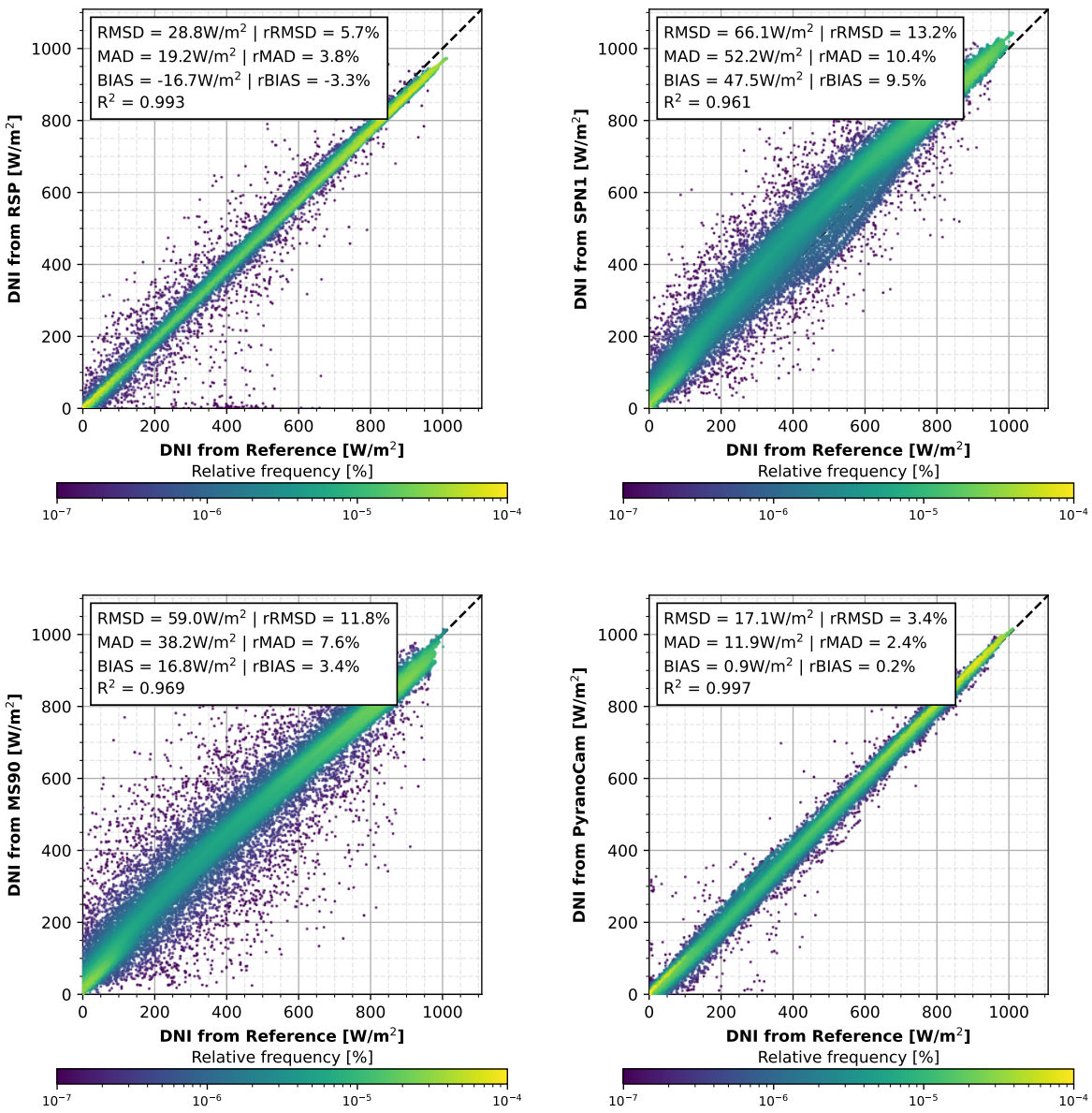

Figure 4.5: Scatter density plots of radiometers' DNI over the reference DNI, with information on the respective RMSD, MAD, BIAS, and R^2-score. Evaluated on 1-minute resolution.

4.2 Evaluation and Interpretation of the DHI Performance for 1-Minute-Resolution

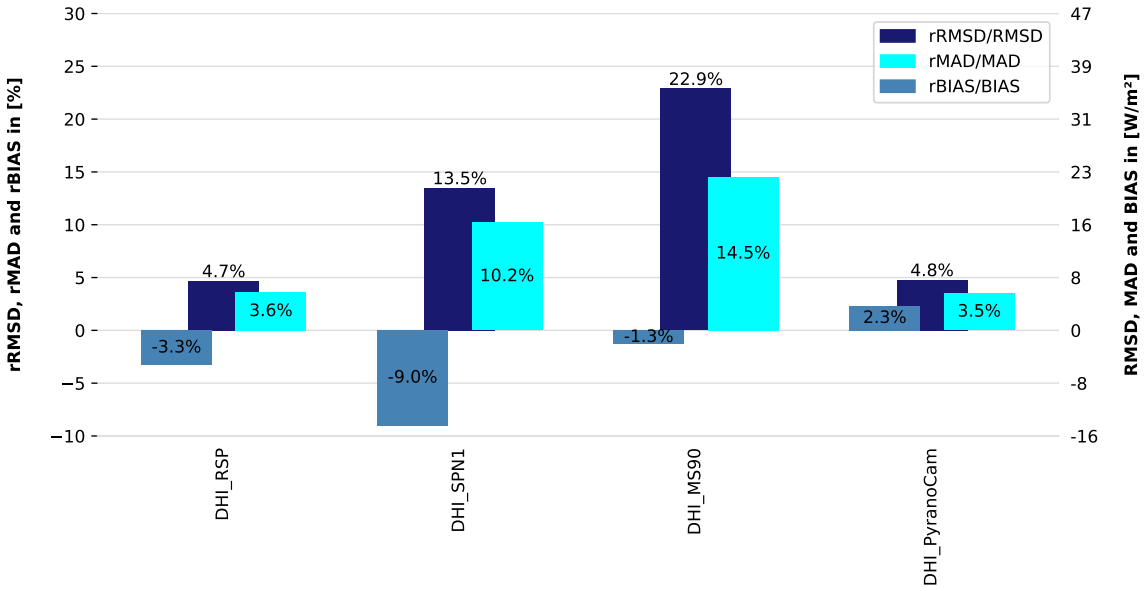

Figure 4.6: Comparison of RMSD, MAD, and BIAS for DHI in 1-minute resolution. The relative scale is attached on the left side, and the absolute scale is on the right side.

Fig 4.6 compares the RMSD, MAD, and BIAS of the tested radiometers for DHI, based on the data set "Performance Analysis (1-Minute-Resolution)" from Table 3.6. The respective findings from [6] and [45] are given in Table 4.3.

In contrast to the DNI measurement, the performance ranking changes for both, the RMSD as well as the MAD:

1. RSP
2. PyranoCam
3. SPN1
4. MS-90

Table 4.3: Results from [6] and [45] for DHI in 1-Minute Resolution. For [6], the values for the expanded uncertainty are calculated within a 99.3% interval. Favorable conditions are understood as periods in which the DNI varies by less than 10 W/m² within a 15-minute window.

	All-Sky Conditions [6]		Favorable Conditions [6]		All-Sky Conditions [45]
	RSP	SPN1	RSP	SPN1	PyranoCam
RMSD	7 - 12	21	4 - 16	17	6
MAD	5 - 8	16	3 - 11	15	n.a.
BIAS	-5	-10	-22 - -13	-15	2
Expanded Uncertainty	±20	-45 - 20	25 - 40	-45 -15	n.a.

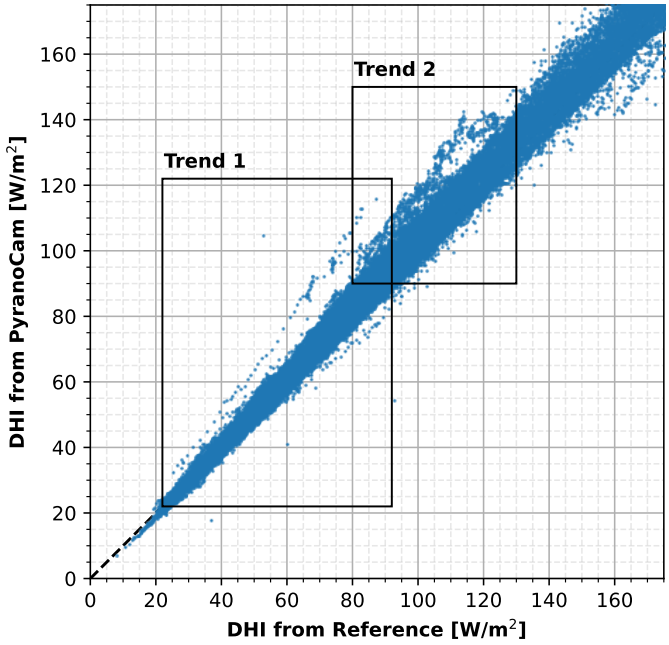

Figure 4.7: Visualization of the trends in PyranoCam's DHI measurement

As was the case with the DNI measurement, the calculated values for the RMSD of the RSP (7.3 W/m², 4.7%) also agree with those from [6] for both, all-sky and favorable conditions (cf. Table 4.3). Considering the RSP's MAD (5.5 W/m², 3.6%), it can be stated, that it differs moderately from the RMSD and, thus, a high number of large outliers cannot be detected in Fig 4.9, even though some are present. Comparing the MAD's absolute value with the corresponding value ranges from [6] in Table 4.3, its correctness can be verified since the here calculated MAD lies within both ranges. Furthermore, the RSP BIAS' absolute value almost equals its MAD, which on the one hand indicates, that the RSP underestimates the DHI signal and on the other hand, that its MAD for the largest part results from that. A rather small scatter of the measured values is hence visible in Fig 4.9. The BIAS determined in this study (-5.1 W/m², -3.3%) suits well the BIAS for all-sky conditions in Payerne [6] (-5 W/m²) and does not lay inside the range of BIAS observed for favorable conditions (Table 4.3).

Also for DHI, the PyranoCam method shows a relatively low RMSD value of 7.9 W/m² (4.8%), which is nearly the same value as for the RSP (7.26 W/m²) and which matches the findings from [45] (6 W/m², 3.7%). The ratio between MAD (5.5 W/m², 3.5%) and RMSD is about 73%, and thus the number of large outliers is quite low (cf. Fig 4.9). Looking at the BIAS' absolute value of 3.5 W/m² (2.3%) explains why PyranoCam overestimates the DHI signal on average. Since the MAD results only partially from BIAS, the ASI-based radiometer shows moreover a moderate scattering. In addition, two more trends are also visible in the scatter density plot for DHI in the range between 20 W/m² to 90 W/m² as well as between 80 W/m² to 125 W/m², visualized in Fig 4.7. While the first trend results from the red clouds on the afternoon of 08/09/2022 (Fig 4.8a), trend 2 is the soiling's outcome of the ASI's lens, as can

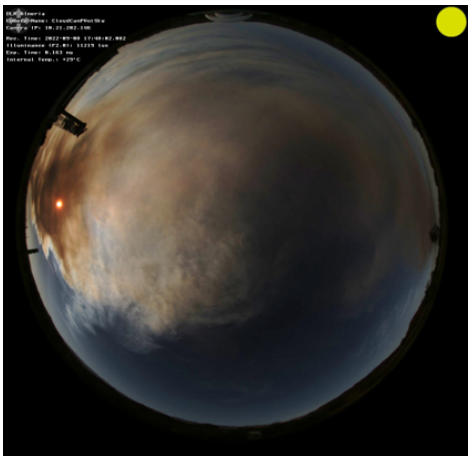

(a) Overestimation on 08/09/2022 due to red clouds on the afternoon for DHI

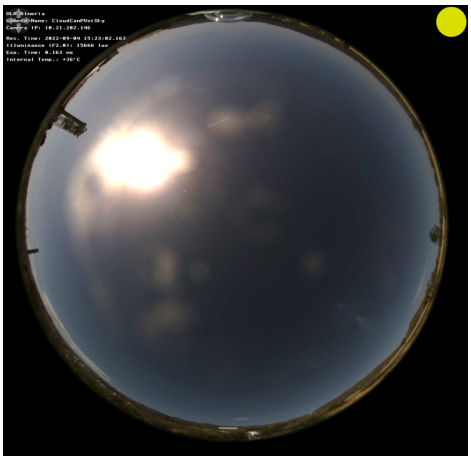

(b) Overestimation on 04/09/2022 due to soiling of the ASI's lens

Figure 4.8: The photographs of the all-sky-imager provide the explanation for the trends in Fig 4.7, where PyranoCam's DHI is overestimated

be seen at the photograph in Fig 4.8b.

The SPN1 shows a relatively high RMSD value of 21 W/m² (13.5%). In Payerne [6], RMSD ranges between 21 W/m² for all-sky conditions and 17 W/m² for favorable conditions. As already seen in the DNI measurement, the SPN1 readings in Tabernas match the all-sky conditions in Payerne better than the favorable data set. Due to a ratio of 76% between RMSD and MAD (15.8 W/m², 10.2%), large outliers are rarely visible in the corresponding scatter density plot in Fig 4.5. SPN1's BIAS (-14 W/m², -9%) is about 88% of the MAD. The sensor hence underestimates DHI on average very strongly, which explains almost fully the MAD. Its absolute value suits well the results from [6] (cf. Table 4.3).

MS-90 shows again a high value for the RMSD of 35.5 W/m² or 22.9%. Unfortunately, no comparative value for the DHI measurement is given by the manufacturer or by Pó in [34]. The MS-90 exhibits the lowest BIAS (-2.1 W/m², -1.4%) of all radiometers when measuring the DHI and, hence, almost neither underestimates nor overestimates the reference values on average. Nevertheless, in contrast to the other sensors, the ratio of MAD and RMSD for the MS-90 is significantly lower with a value of only 63%. Hence, the scatter plot in Fig 4.5 indicates not only a strong dispersion but also one, which is marked by a high number of large outliers. Here, too, there is a conspicuous feature in the associated scatter density plot, as there is a clear trend in the form of an upward bulge between 50 W/m² and 130 W/m². It can be shown that the MS-90 clearly overestimates the DHI when DNI is greater than 850 W/m² at the same time. This effect explains this upward bulge.

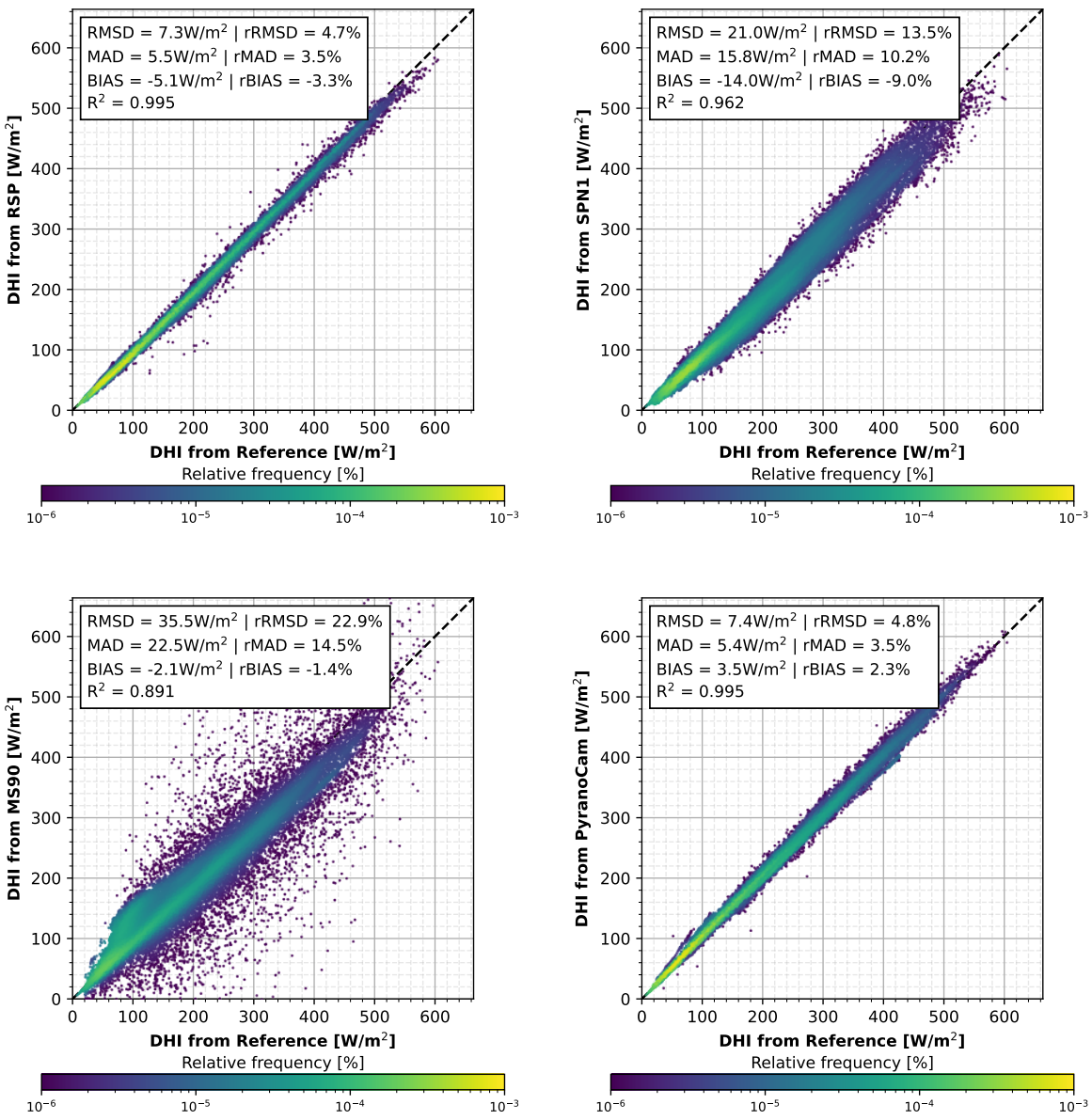

Figure 4.9: Scatter density plots of radiometers' DHI over the reference DHI with information on the respective RMSD, MAD, BIAS, and R^2-score. Evaluated on 1-minute resolution.

4.3 Evaluation of the Sensor's Performance for Different Time Resolutions

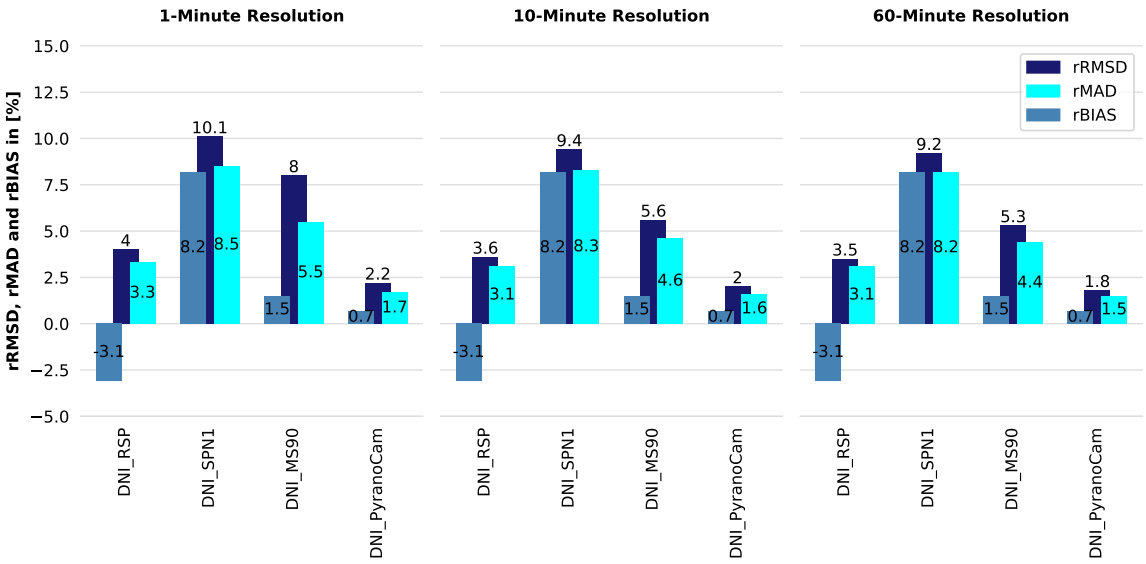

Figure 4.10: Evolution of RMSD, MAD, and BIAS over time resolution of 1, 10, and 60-minutes for DNI. All Values are given in %.

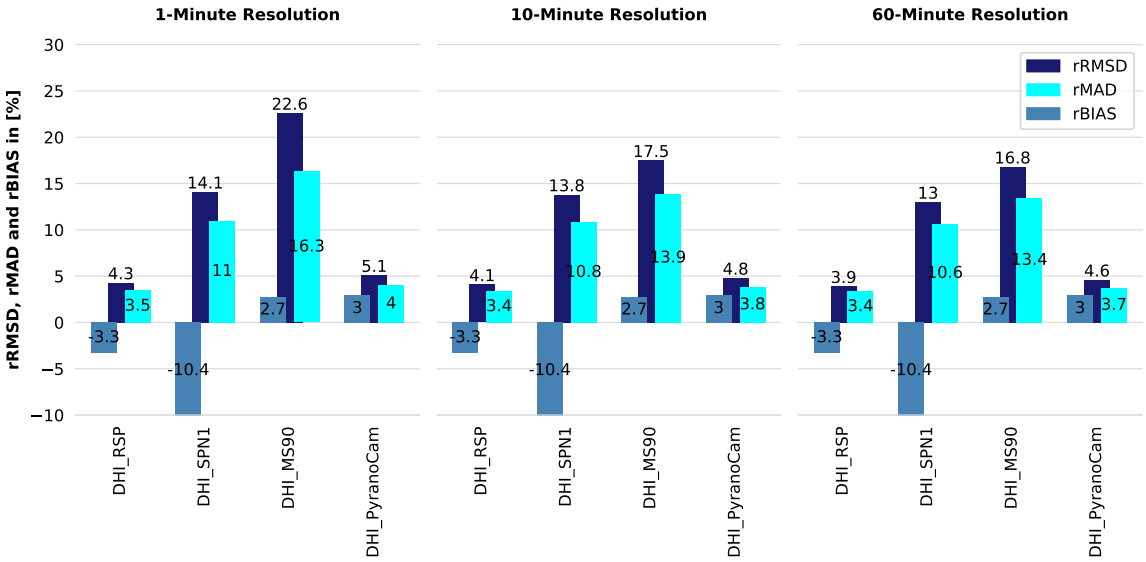

Figure 4.11: Evolution of RMSD, MAD, and BIAS over time resolution of 1, 10, and 60-minutes for DHI. All Values are given in %.

Figures 4.10 and 4.11 show the evolution of the three deviation metrics RMSD, MAD, and BIAS over the time resolutions of 1, 10, and 60 minutes, respectively for DNI and DHI. The values are based on the adjusted data sets from Table 3.6.

Looking at the DNI in Fig 4.10, it can be seen that as expected, the RMSD decreases with coarser temporal resolution. The RMSD for PyranoCam and SPN1 decreases moderately

from 1 to 10 to 60-minute resolution. In contrast, the MS-90 and also the RSP show a significant drop from 1-minute to 10-minute resolution. Since MS-90 is affected by noise in the form of an oscillation with a period time of 6 minutes, this noise is canceled out for the largest part when 10 and 60-minute averages are evaluated. Due to the noise's existence, an adjustment was made to the MS-90's logger program during the ongoing measurements on 08/09/2022. Fig. 4.12a and 4.12b compare an exemplary DNI time series from the MS-90 before and after the adjustment. However, the calculation of the effect of the oscillation on the RMSD shows that it is negligible (for further explanations see Appendix A.3). Rather, it is assumed that changing atmospheric conditions (and especially less clear conditions) are the reasons for the increased RMSD at a fine temporal resolution of the measurement data, as is discussed in Chapter 5 in more detail. If the MS-90 does indeed has greater deviation under less clear conditions, then it confirms the findings from [34]. It states that the MS-90 measurement deviation doubles from ±5% to ±10% for DNI $< 700\,\mathrm{W/m^2}$. These unstable conditions are largely eliminated by the 10-minute and 60-minute averaging.

In a further step, as before the 1-minute values, now the 10- and 60-minute values are compared with those of Habte et al.'s study in [4]. The respective values are given in Table 4.4. Here, clear-sky conditions are defined as being below a cloud cover threshold of 1.2%, measured with a TSI-880 [57]. The results from [4] are, however, only comparable to a limited extent. First, for calculating BIAS, only values within an interval of ±50% around the nominal value are considered. Secondly, both BIAS and RMSD are only given as the arithmetic mean of a 95% confidence interval. Finally, the calculation of the relative metrics differs from the common way (cf. Equation 4.5). In [4], relative RMSD, for instance, is calculated as:

$$rRMSD_{\text{Habte et al.}} = \sqrt{\frac{1}{n} * \sum_{i=1}^{n} \frac{(y_i - y_{ref})^2}{y_{ref}}} \tag{4.6}$$

For the RSP and 60-minute resolution, the RMSD is $23\,\mathrm{W/m^2}$ (3.5%). Habte et al. find an RMSD of 7% for all-sky conditions and 2.5% for clear-sky conditions. The RMSD value for the DNI measurement deviation determined within the scope of this study in Tabernas is between the values found by Habte et al. for all-sky conditions as well as clear-sky conditions. In comparison, the SPN1 exhibits an RMSD of $61.3\,\mathrm{W/m^2}$ (9.2%) for DNI at 60-minute resolution and, hence, is similar to the value found by [4] for all-sky conditions (cf. Table 4.4).

Table 4.4: Results from [4] for DNI and DHI in 10 and 60-minute resolution. All values are given in %. All Metrics are calculated within an interval of ±50% around the nominal value and given as the arithmetic mean of a 95% confidence interval. Clear-sky conditions are defined as being below a cloud cover threshold of 1.2%, measured with a TSI-880 [57].

	All-Sky-Conditions				Clear-Sky-Conditions			
	10-Minute-Resolution		60-Minute-Resolution		10-Minute-Resolution		60-Minute-Resolution	
	RSP	SPN1	RSP	SPN1	RSP	SPN1	RSP	SPN1
RMSD	-	-	7	9.5	-	-	2.5	6
BIAS	0	7	-3	7.5	2.5	4	2	1

The MAD also shows a sharp decrease from a 1-minute to a 10-minute resolution for the MS-90. However, this is not as noticeable as with the RMSD. Furthermore, the fact that the BIAS stays constant over the different time resolutions indicates that there are no artifacts in the evaluation. As the given values in Table 4.4 are the means of a 95% CI, it is plausible that it varies over time resolution. However, comparing the respective BIAS values, it gets obvious that both, the RSP's and the SPN1's BIAS at 60-minute resolution are similar to the ones for all-sky conditions in Golden. Since in [4], only GHI and DNI signals are considered, a further comparison to Habte et al.'s study is not possible. In contrast to Payerne, the locations of Golden and Tabernas are similar in terms of their DNI irradiation over the year but differ to some extent in their diffuse irradiation. Therefore, it seems plausible that the values determined by Habte et al. for the RMSD and BIAS under all-sky conditions also fit the values determined in Tabernas under all-sky conditions.

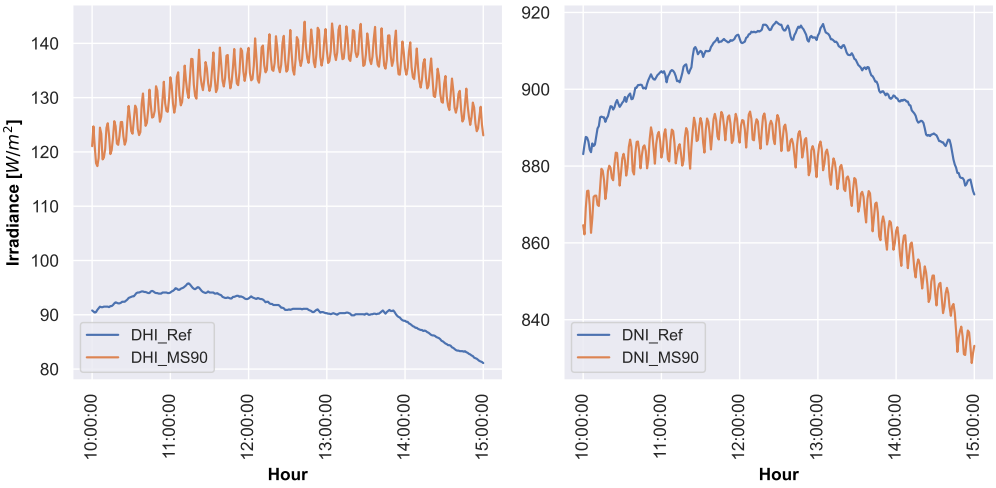

(a) MS-90's DNI and DHI signal in comparison to the reference signal before adjusting the logger program. Evaluated day: 23/08/2022

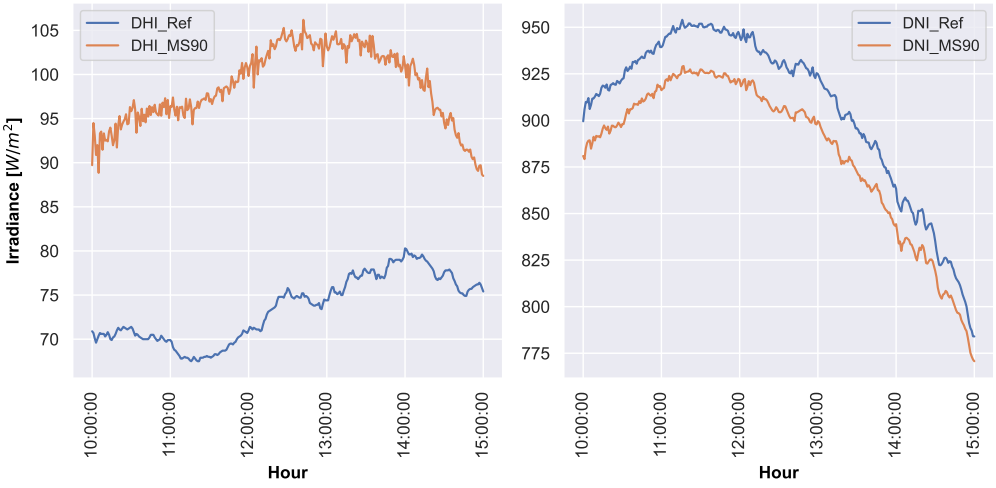

(b) MS-90's DNI and DHI signal in comparison to the reference signal after adjusting the logger program. Evaluated day: 13/10/2022

Figure 4.12: MS-90's DNI and DHI signal before and after adjusting the logger program

4.4 Determination of the Uncertainty

A measured value without a statement about its accuracy is not complete and not reliable. The uncertainty of a measurement, therefore, indicates the absence of precise knowledge of the true value of the measurand [58]. According to scientific standards, the so-called expanded uncertainty is normally given. It follows the JCGM 100:2008 [58]. Within this standard, a distinction is made between so-called Type A and Type B evaluation of measurement uncertainty. Type A is the more reliable method, as it requires that data are collect by oneself, as is the case here, and do not come from third parties [59]. The standard uncertainty $u(x_i)$ is calculated as the standard deviation $s(\overline{X_i})$ of all mean values of various measurements around the mean value of the mean values [58]:

$$u(x_i) = s(\overline{X_i})$$

Expanded uncertainty U is then defined as an interval that includes at least 90% (or more) of the measured values, depending on the selected multiplication factor k [58]:

$$U = k * u(x_i)$$

k usually takes values of 1.64, 1.96, and 2.58 and, hence, corresponds to the empirical 90–95–99 rule, also called sigma rule[1] [58]. If Type A applies and the available data are not normally distributed, it is not required to indicate the expanded uncertainty as the standard deviation multiplied by a factor. Instead, it may also be given as an interval with a level of prediction of 90%, 95%, or 99% [58]. For this reason, the measurement deviations are first tested for being normally distributed. Various mathematical methods could be used for this purpose, such as Kolmogorov Smirnov or the D'Agostino & Pearson Test [61]. Demir showes in his work from [61], that when the skewness and kurtosis coefficients are equal to or near zero, the sample size has no impact on the results of normality tests. However, he also shows that normality tests are indeed influenced by the sample size and tend to provide falsified findings, especially for sample sizes with more than 200 samples, in situations where the skewness and kurtosis coefficients deviate from zero. For such cases, instead of normality tests, histograms should be used. In this thesis, hence, the data set is tested for normality by plotting a histogram as well as a probability plot and by calculating the respective statistical factors for the skewness and kurtosis, with help of [62] and [63]. The results of the tests are exemplarily visualized for the SPN1 (Fig 4.13). Both the histograms and the probability plots clearly and without doubt prove that the measurement deviations of the sensors are not normally distributed. This is also shown by the corresponding values for skewness and kurtosis. Moreover, the histograms match with the results from Sections 4.1 and 4.2. It was shown that the SPN1 tends to overestimate the DNI but underestimates the DHI. Underestimation

[1] This context can be seen when looking at the corresponding Equations for determining the standard and expanded uncertainty in [58]. The 90–95–99 rule states that for a normal distribution approximately 90%, 95%, and 99% of all values are in the intervals $I_{90} = [\mu \pm 1.64\sigma]$, $I_{95} = [\mu \pm 1.96\sigma]$ and $I_{99} = [\mu \pm 1.64\sigma]$ [60]. The multiplier for sigma corresponds to the k-value in this case.

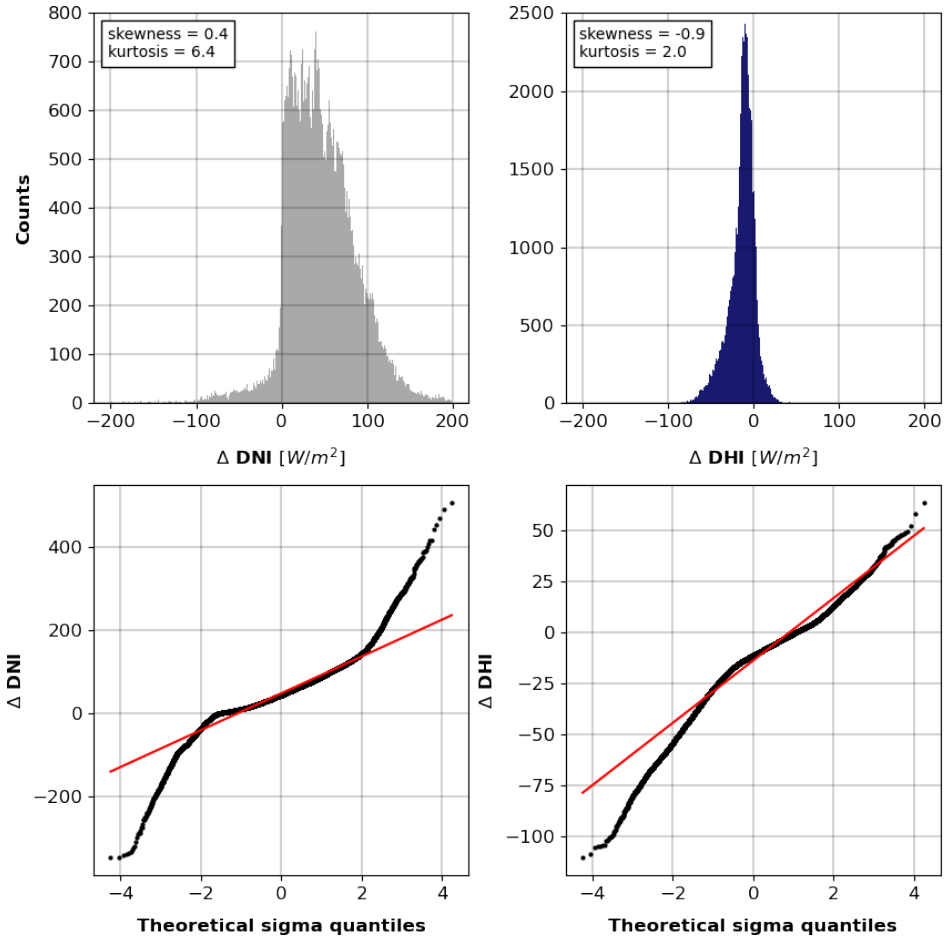

Figure 4.13: Graphical check for normal distribution for the DNI and DHI measurement deviation of the SPN1 using histograms, probability plots and specifying the skewness and kurtosis

results in a mean value shifted to the left, and thus to a positive skew of the distribution. Overestimation, on the other hand, leads to a negative skew, because of a mean value shifted to the right. All the findings described here can also be determined for the other radiometers (cf. Appendix B.2).

To draw conclusions, the sensor's uncertainties cannot be calculated according to [58]. Instead, a 95% prediction interval PI_{95} is used, as it provides the range in which 95% of the deviations are found[2]. The application of such an interval is compliant with the requirements of [58] as described above. PI_{95} represents the difference between the 97.5^{th} and the 2.5^{th} percentile:

$$PI_{95} = p_{97.5} - p_{2.5} \tag{4.7}$$

[2]The prediction interval (PI) must not be confused with the confidence interval (CI). CI indicates the probability of a statistical parameter, such as the arithmetic mean, lying within a range of values. If, for example, the confidence interval is calculated for 100 samples of a population and 95 of the 100 confidence intervals contain the statistical parameter of interest, this corresponds to the 95% confidence interval. CI, however, does not, in any case, say anything about the dispersion of the measured values around the mean value and thus also nothing about the location of individual or future measured values. At this point, the prediction interval is used. Logically, the range of PI is therefore significantly larger than that of CI.

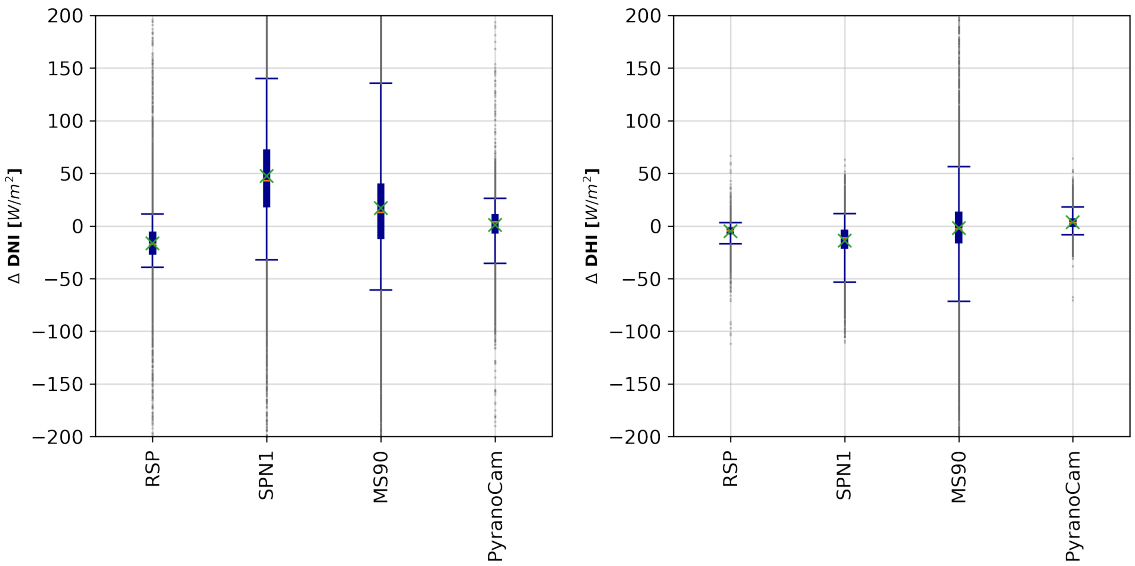

Figure 4.14: Representation of the measurement uncertainty as boxplots for all sensors for DNI (left) and DHI (right). The whiskers represent the 95% prediction interval PI_{95}. The mean and median are marked by the green cross and the orange horizontal line. The blue box includes the interval between the 25^{th} and 75^{th} percentile.

The prediction intervals of the sensors can be taken from the boxplots in Fig 4.14, represented by the whiskers. Table 4.5, furthermore, provides all relevant dispersion parameters.

The MS-90 sensor for the DNI shows the greatest measurement uncertainty, closely followed by the SPN1. The PI_{95} of the PyranoCam method is comparable to that of the RSP sensor for DNI measurement. The same ranking is also shown by the results for the measurement of diffuse radiation. The position of the dispersion parameters around the zero axis matches the results for the BIAS from the previous Sections. Since RSP's MAD results nearly completely from its BIAS, it is plausible, that it's PI_{95} is narrower than the one from PyranoCam, even

Table 4.5: Dispersion parameters for the DHI and DNI absolute measurement deviations of each sensor, based on data set 1 from Table 3.7. The parameters $p_{0.025}$ and $p_{0.975}$ correspond to the 2.5^{th} and 97.5^{th} percentile and represent the 95 prediction interval PI_{95}. $IPR_{PI_{95}}$ provides the interpercentile range for PI_{95}. All Values are given in W/m^2.

	DHI				DNI			
	RSP	SPN1	MS90	PyranoCam	RSP	SPN1	MS90	PyranoCam
Mean	-5.1	-14.0	-2.1	3.5	-16.7	47.5	16.8	0.9
Mode	0.0	41.0	14.0	5.0	-4.0	-8.0	-2.0	3.0
Median	-4.5	-11.4	-2.6	3.2	-17.2	42.9	12.8	3.9
$p_{2.5}$	-16.7	-53.2	-71.4	-8.3	-39.2	-32.0	-60.9	-35.5
$p_{97.5}$	3.2	11.8	56.2	18.0	11.4	140.2	135.6	26.2
$IPR_{PI_{95}}$	19.9	65.0	127.6	26.4	50.6	172.2	196.5	61.7

though PyranoCam shows the smaller MAD value for DNI. The same applies to the MS-90 and the SPN1. Since [6] predicts the error distribution in an interval, which contains 99.3% of all values, the results are, again, only possible and meaningful to compare to a limited extent. Nevertheless, it seems to be obvious, that the limits of prediction interval from this thesis should be within the limits from [6] (cf. Table 4.2 and 4.3). For the RSP this applies for both, all-sky and clear-sky conditions, while the SPN1 tends to be closer to the all-sky conditions. Again, as already mentioned earlier, the differing meteorological circumstances seem to negatively affect the SPN1's performance in Tabernas, in contrast to Payerne.

4.5 Discussion of the Performance Analysis

Summarizing the findings from the previous sections, the following can be stated:

With respect to the RMSD and MAD, the PyranoCam method shows the best performance for the DNI measurement, followed by the RSP, the MS-90, and finally the SPN1. While PyranoCam seems to be free of BIAS, the here examined RSP underestimates the DNI as well as the MS-90. In contrast, as already known from other studies and proven here, SPN1 overestimates the DNI, which basically results from its design and spectral response-related DHI underestimation, as it. Especially the MS-90 and the SPN1 show both a generally large spread and an increased number of large outliers. In contrast, the measured values of the RSP scatter only to a small extent but show some large outliers. In the DHI measurement, the RSP performed best of all sensors. PyranoCam is in second place, followed by SPN1 and MS-90. The latter one shows a particularly high number of large outliers here, while the SPN1, on the other hand, generally scatters to a moderate to a strong degree. Moreover, except for the PyranoCam method, all sensors underestimate the DHI, albeit to different degrees. Examining the change of the three metrics over time resolution yields, that averaging the sensor data to 10 minutes provides a good compromise between temporal resolution and accuracy of the data.

The SPN1, the MS-90, and also the PyranoCam methods show some conspicuities. Against the expectations and the hypothesis formulated at the beginning of this chapter, the SPN1 tends to fit the all-sky conditions from [6] better than the favorable conditions when measuring DNI, even though in the data set available for this study, there are a high number of days with a $k_{c,\,DNI}$ close to 1. Apparently, there has to be some meteorological influence existing or appearing stronger in Tabernas than in Payerne, which negatively influences the SPN1's DNI measurement. The higher ambient temperature and turbidity-related influences in Tabernas could lead to increased deviations of the SPN1. Theoretically, the angle of elevation could also be an influence, as the sun is higher in the sky in southern Spain than in Switzerland. However, the data set used here represents rather moderate Sun elevations. A similar effect may be present for the DNI measurement of the MS-90 since the R^2-score from [34] could not be confirmed here. This can either be due to a small data set or a location-specific meteorological influence that affects EKO's MS-90 sensor. Nonetheless, the reliability of [34]

is limited due to the small data set. For the camera-based measurement method, it can be stated, that a stronger weighting of the red parts in the spectrum probably leads to an overestimation of the DHI. Furthermore, the influence of turbidity and soiling shows a clear trend toward overestimation of the DNI. However, these assumptions are investigated in depth in the subsequent Chapter 5.

5 Correlation Analysis and Evaluation

In Chapter 5, the processed data of the individual sensors are analyzed with regard to the research question:

> Do the measurement deviations of the individual sensors correlate with various meteorological parameters? If so, which influencing factors affect the sensors most strongly, and to what is this dependence related?

Measurement deviations δ are considered in relative values and calculated as:

$$\delta = \frac{y_i - y_{ref}}{y_{ref}} \tag{5.1}$$

The dependence of the sensors' measurement deviation on atmospheric and meteorological conditions, is analyzed quantitatively with the help of Spearman's Rank correlation coefficient ρ and qualitatively with the help of scatter density plots. In the latter method, the measurement deviation is always plotted over a meteorological influence factor. As described in Chapter 3, due to the unequal locations of the radiometers and the WISERs, only stable sky conditions are available for the correlation analysis. According to [6], stable conditions are defined as the DNI varies by less than $10\,\mathrm{W/m^2}$ in a 15-minute period.

In general, there are two common possibilities to examine two variables for correlation:

- Pearson product-moment correlation coefficient
- Spearman's rank correlation coefficient

The correlation coefficient according to Pearson[1], which is widely used in science, represents the degree of strength of a linear relationship between two variables [64]. It assumes a normal distribution of the data and is thus limited to the linear dependence of the variables. Spearman's rank correlation coefficient[2] on the other hand, provides evidence of the degree of correlation between two monotonically related variables. It is, consequently, not limited to linear relationships [64], but to monotonically ones. As proven in Section 4.4, the distribution of the deviations is not Gaussian. Hence, the correlation coefficient according to Spearman

[1] Karl Pearson (1857-1936), British mathematician
[2] Charles Edward Spearman (1863-1945), British psychologist and mathematician

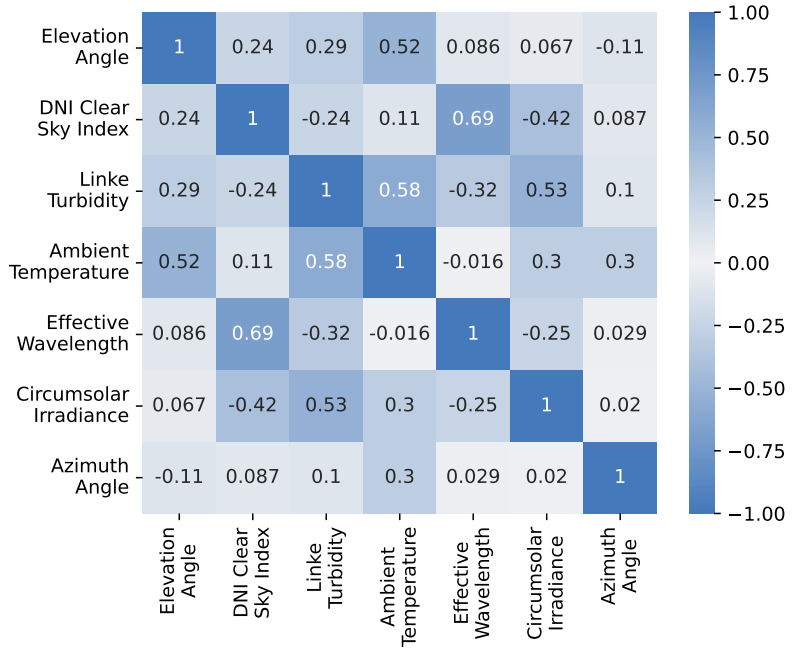

Figure 5.1: Heatmap of the meteorological parameters' correlation matrix

is used to examine and quantify the meteorological influences on the measurements. It is calculated as:

$$\rho = 1 - \frac{6 * \sum_{i=1}^{n} (r_{xi} - r_{yi})^2}{n * (n^2 - 1)} \tag{5.2}$$

Where ρ is Spearman's rank correlation coefficient, n is the sample size, and $r_{x,i}$, as well as $r_{y,i}$, are the individual paired values, respectively the ranks. The exact definition is given in [64] and [65]. To interpret and evaluate the correlation values, the rules according to Cohen's work from [66], are used as a convention for this thesis, since the interpretation of Pearson's and Spearman's coefficient is similar [64]. Based on these rules, only correlations greater than 0.3 are considered true correlations in the context of this work. As stated above, Spearman's rank correlation coefficient only detects correlations between monotonically related variables. For this reason, the results are controlled visually with the help of scatter density plots. Meteorological factors of influence from Section 2.2 partly correlate with each other or even stand in a cause-and-effect logic to each other. For instance, the Linke turbidity T_L deter-

Table 5.1: Interpreation rules for Spearman's rank correlation coefficient according to [66]. It states: $0 \leq \rho \leq 1$

Absolute value of ρ	Interpretation
0 - 0.1	no to weak correlation
0.1 - 0.3	weak to moderate correlation
0.3 - 0.5	moderate to high correlation
> 0.5	strong correlation

mines the circumsolar irradiance CSI to some extent (see also Section 2.2.2) and similarly, it can be expected that the DNI clear sky index $k_{c,\ DNI}$ correlates with the effective wavelength λ_{eff}, as described in Section 2.2.4. Thus, an appropriate correlation matrix is calculated for the meteorological parameters. it is visualized as a heatmap in Fig 5.1. The comparison of the individual parameters in scatter plots is secondary at this point but can be found in Appendix B.3.

The subsequent Sections 5.1 and 5.2 are structured as follows. In the first step, all correlation coefficients for the RSP, the MS-90, the SPN1, and the PyranoCam method are calculated. Then, for each case, the corresponding main and secondary influences are identified and compared with the findings from previous Sections.

5.1 Determination of the Correlation between Deviation of Measurement and Meteorological Influence

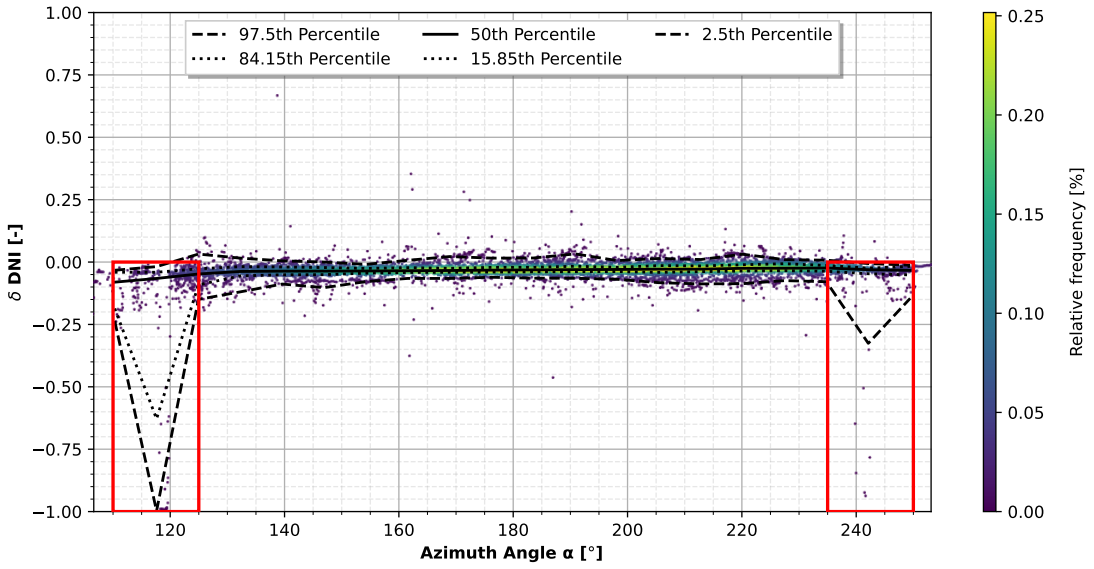

Figure 5.2: Anomalies in RSP's DNI measurement under the influence of the azimuth angle

Before examining the sensors in Section 5.2 for their main and secondary influences, anomalies in the scatter density plots should first be discussed. In doing so, only those plots will be considered, which show a measured and not a calculated irradiance signal (see Section 3.2.2).

Beginning with the RSP, an increasing number of large outliers for the DNI measurement can be identified, when looking at azimuth angles around $\alpha = 120°$ and $\alpha = 240°$ (see Fig. 5.2). Outliers at $\alpha = 120°$ probably result from the shading of the sensor by the sun tracker and, hence, indicate a shortcoming in the data preprocessing. With regard to the filters applied in Section 3.2.1.4, it is therefore recommended to reject timestamps already, when the test signal is $< 10\,\mathrm{W/m^2}$ (compared to a reference value of $100\,\mathrm{W/m^2}$). Within the data preprocessing a threshold of $0\,\mathrm{W/m^2}$ was used. Moreover, the manual identification of shading has to be improved.

All other anomalies appearing in the initial check before the analysis are characterized by data point clouds as exemplified in Fig 5.3 for MS-90's DNI. Fig 5.3 is representative of all other plots in Appendix B.3. These data point clouds result indeed from the strong haze of the sky on 03/10/2022 (Fig 4.4b). Looking at Linke turbidity's histogram in Fig 5.4, it is noticeable that the occurrence of extremely high values ($T_L > 8$) is a rarity. If more days with high turbidity values were available, then a larger dispersion of δDNI and δDHI can be assumed. Therefore, two findings can be derived from screening the anomalies:

1. The meteorological influencing factor "turbidity" affects the measurement accuracy of all sensors except the RSP, since it leads to high outliers (partially outside PI_{95}) or anomalies in the scatter plots, respectively.

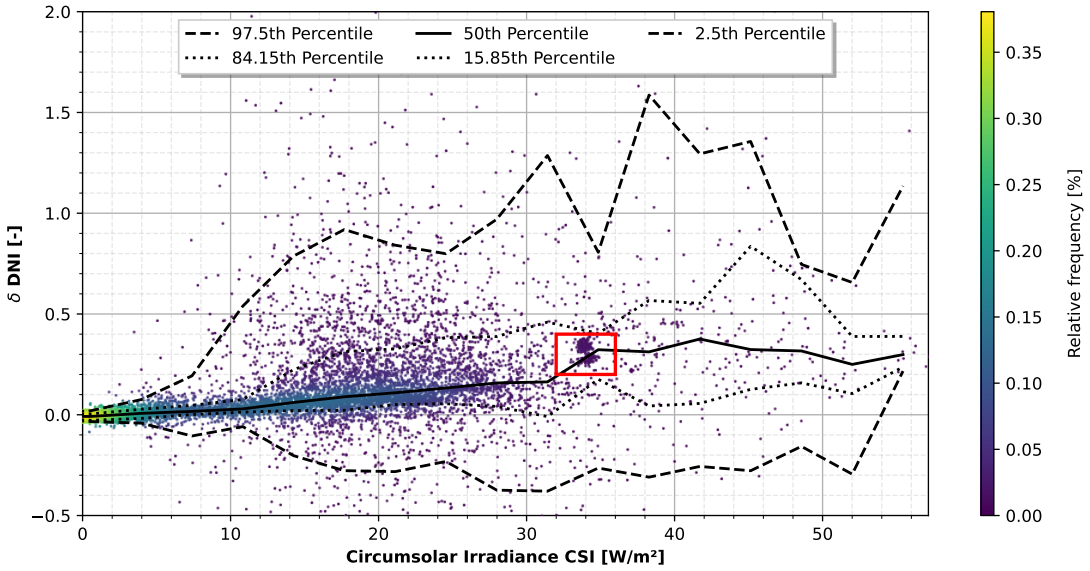

Figure 5.3: Anomalies in MS-90's DNI measurement under the influence of the circumsolar irradiance

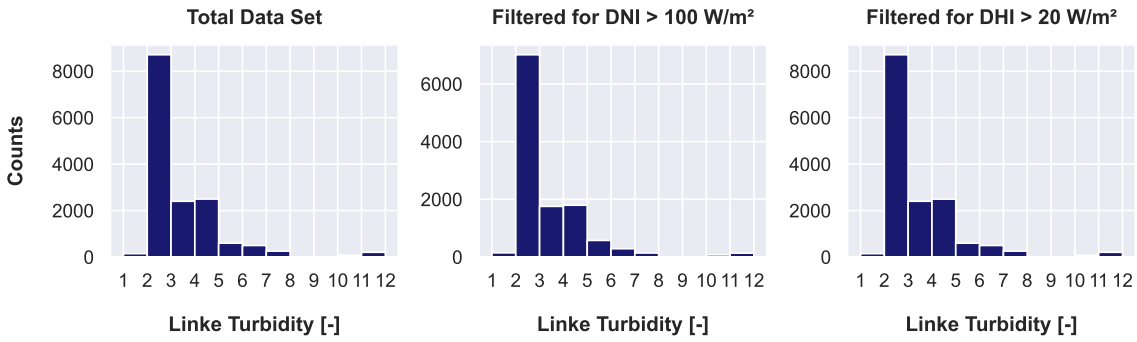

Figure 5.4: Histograms of the available Linke turbidity data for the correlation analysis

2. The dispersion of the data points, thus, significantly increases for days with high turbidity. Therefore, the measurement reliability for the SPN1, MS-90, and PyranoCam sensors probably decreases in areas with annually high turbidity values. Nevertheless, this assumption has to be verified by considering more days with such extreme values for the Linke turbidity, as they appear on 03/10/2022.

However, regarding these two findings, the cause-effect chain must also be taken into account. Depending on the atmospheric factors' correlations, the haze itself can also only be the root cause of another meteorological parameter. That means, that a sensor might not directly be influenced by the Linke turbidity T_L, but by an atmospheric condition like the effective wavelength λ_{eff} or the circumsolar radiation CSI, that depend on the turbidity level, among others.

5.2 Identification and Classification of Main and Secondary Influences

Now that the appearance and origin of anomalies have been discussed in the corresponding scatter plots, the task is to identify and classify the atmospheric parameters, that influence the particular measurements the most. In Section 5.2.1, only the procedure for determining the main and secondary influences is explained, for the sake of clarity. It is then followed by Sections 5.2.2 and 5.2.3, which contain the evaluation and discussion of the results.

5.2.1 Description of the Procedure

The classification of the meteorological parameters into main and secondary influences can partly be done with the help of Table 5.2. Since the main impact can also correlate with other parameters, as given in Fig 5.1, not all coefficients greater than 0.3 (marked in light blue)can be classified as secondary influences. It is rather necessary to eliminate the main influence from the original data set and to calculate a new matrix based on the adjusted data set then. For this purpose, a regression model of the third degree is calculated, by minimizing the squared error E:

$$E = \sum_{i=1}^{n} |(p(m_i) - y(m_i))|^2 \tag{5.3}$$

where p_i is the respective value for the polynomial and y_i the deviation of the measurement, depending on the value of the main influence m_i in the data pair i. This computation is implemented in NumPy's `numpy.polyfit` function [67]. The so-calculated regression model is then applied to the data set by subtraction, according to Equation 5.4:

$$\begin{aligned} \delta DNI(m_i)^* &= \delta DNI(m_i) - p(m_i) \\ \delta DHI(m_i)^* &= \delta DHI(m_i) - p(m_i) \end{aligned} \tag{5.4}$$

Table 5.2: Spearman's correlation matrix for DNI and DHI, based on the relative measurement deviations and the meteorological influence factors. All values greater than 0.3 are colored in with main influences colored in .

	DNI				DHI			
	RSP	SPN1	MS-90	PyranoCam	RSP	SPN1	MS-90	PyranoCam
Elevation Angle	-0.33	0.08	-0.03	0.18	0.24	-0.03	0.08	0.17
Azimuth Angle	0.32	0.02	0.04	0.22	-0.10	0.08	-0.04	-0.05
DNI Clear Sky Index	-0.04	-0.63	-0.59	0.40	0.01	-0.50	0.54	0.51
Linke Turbidity	-0.29	0.55	0.44	-0.09	0.04	0.02	-0.42	-0.17
Ambient Temperature	-0.23	0.31	0.17	0.04	0.1	0.004	-0.10	0.15
Effective Wavelength	0.15	-0.46	-0.36	0.20	0.2	-0.35	0.40	0.41
Circumsolar Irradiance	-0.04	0.76	0.68	-0.13	0.03	0.002	-0.68	-0.27

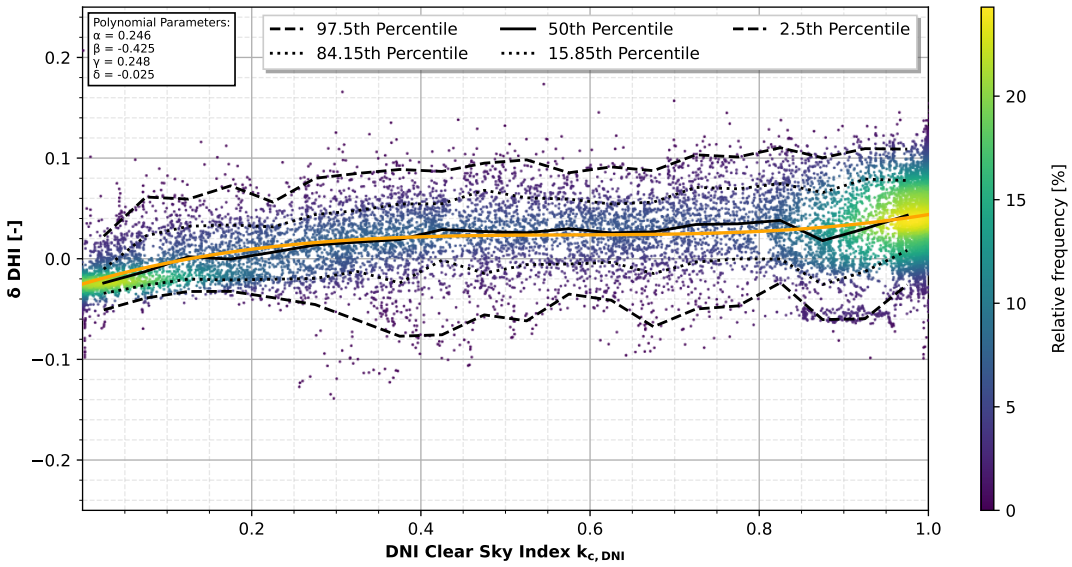

Figure 5.5: Plot of the DHI measurement of the PyranoCam method over the main influence of the circumsolar irradiance on the original, unadjusted data set. The regression corresponds to a polynomial of degree 3.

Where the adjusted data are marked by *. Only secondary influences, which have a correlation coefficient $\rho > 0.2$ with the measurement deviation (on the adjusted data set), are considered in more depth in the scope of this analysis and are consequently treated as true secondary influence parameters. The exact approach is exemplified by the PyranoCam method for the DHI measurement below.

First, the main influence from Table 5.2 is identified and visualized in a scatter plot as given by Fig 5.5. The additional consideration of the data points' density distribution provides information about the correlation coefficients' significance and reliability. If the density is too low, for instance, the reliability decreases. Looking at Table 5.2, the DNI clear sky index $k_{c,\,DNI}$ influences PyranoCam's DHI measurement in the strongest way with a correlation coefficient of $\rho = 0.51$. According to Cohen's rules for interpretation, this value corresponds to a strong correlation. A further influence on the original data set is given by the effective wavelength λ_{eff} ($\rho = 0.41$). Both meteorological parameters are correlated with a coefficient of 0.69 (Fig 5.1), which indicates that both influences should show a lower correlation with δDHI, after adjusting the data set for the main influence factor. This is done with the help of the calculated regression polynomial $p(m_{k_{c,DNI}})$:

$$p(m_{k_{c,DNI}}) = 0.235 * {m_{k_{c,DNI}}}^3 - 0.406 * m^2_{k_{c,DNI}} + 0.24 * m_{k_{c,DNI}} - 0.025$$

Subtracting each function value of the polynomial from the corresponding value for δDHI yields an updated data set and leads to an elimination of the main influence. This is demonstrated in Fig 5.6. The regression model from Fig 5.5 is applied to the whole value range which is why the parameters of the newly calculated fit on the adjusted data set (upper left corner in Fig 5.6) all converge to 0.

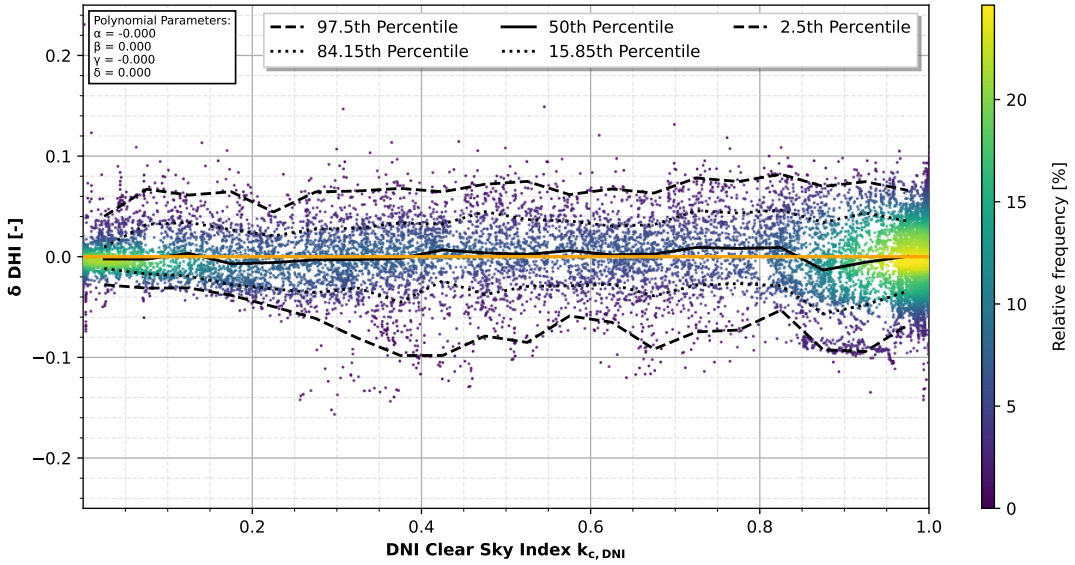

Figure 5.6: Plot of the DHI measurement of the PyranoCam method over the main influence of the DNI clear sky index on the data set corrected for the main influence. Since the regression was applied in the whole value range, the polynomial parameters completely converge to 0.

During the evaluation, however, it is noticeable that the regression model is strongly influenced by the presence of huge outliers or data point clouds (e.g. anomalies as described in Section 5.1). For this case, there are two possible procedures for eliminating the main influence from the data set. Both methods can and are also used in combination.

1. A value range is visually determined so that only data points within this interval are considered to build the model. Apart from that, when the data set is adjusted, the model is applied to all data points. Satisfactory results can be achieved with this method. If it is applied, then it is mentioned in the caption of the corresponding plots.

2. Polynomials are evaluated up to degree three. Should the cubic function not be able to correctly capture all data points, this is expressed in the verification polynomial whose parameters do not converge to zero or whose course in the scatter diagram still shows a dependence of the measurement deviation on the influencing factor. In such a case, a second iteration is performed. Satisfactory results can also be achieved with this procedure. As with method 1, this procedure is noted in the caption of the respective plots.

In the subsequent evaluations for DNI and DHI, among others, results are discussed which are obtained by analyzing scatter density plots of δ over the main and secondary influence. Only the most insightful plots are shown in the following sections. For completeness, the remaining scatter density plots are provided in Appendix B.3. However, they are secondary to the understanding at this point.

5.2.2 Evaluation of the Correlation Coefficients for DNI

The following evaluation is based on the data set "Correlation Analysis (filtered for DNI < 100 W/m²)" from Table 3.6. Starting with the evaluation of the RSP, it can be stated, that due to the physical measuring principle of the LI-COR 200R (photoelectric effect) in particular, the following dependencies of the DNI (and also DHI) can theoretically be expected:

- Ambient Temperature
- Effective Wavelength
- Elevation Angle (corresponds to the error due to shortcomings in the directional response)

As described in Section 2.3.3, silicon sensors show sensitivity to temperature fluctuations, regarding their short-circuit current. Also, [19] states that spectral response is one of RSP's biggest shortcomings (cf. Fig 2.12). The elevation angle ϵ could technically increase both, the cosine error as well as the spectral error. However, when looking at Fig 5.1, only a correlation factor of $\rho = 0.086$ can be observed between ϵ and λ_{eff}, meaning that the elevation angle does not have an influence on the spectral composition of radiation, in this evaluation. As given in Table 3.3, three correction functions are applied for GHI and DHI, respectively, in the logger program. Since the DNI is determined from these both measurands using Equation 2.3,

$$DNI = \frac{GHI - DHI}{\cos\zeta}$$

it can be assumed, that also RSP's DNI signal should show resistance against temperature, spectral and directional errors.

Moving on to the evaluation itself, it can be stated that Table 5.2 indicates that the RSP does not have a particularly large correlation with any meteorological parameter. A correlation coefficient of $\rho = $ -0.33 with the elevation angle ϵ and $\rho = 0.32$ with the azimuth angle α is considered moderate. Still, the elevation angle ϵ is defined as the main influence. After adjusting the data set for the elevation angle ϵ, the RSP shows only an unaltered dependence on the azimuth angle α, which is, hence, defined as a true secondary influence, according to Table 5.1. Since the Linke turbidity T_L and the elevation angle ϵ correlate with only a factor of $\rho = 0.29$ (Fig 5.1), the correlation coefficient for T_L decreases from $\rho = $ -0.29 to a weak correlation of $\rho = $ -0.19 but does not fully disappear.

Relating the main influence to previous studies, the physical measurement principle, and the technical design of the RSP, it can be said, that the increased correlation with the elevation angle ϵ can be attributed to the poor cosine response and, thus, suggests a shortcoming in the respective correction functions. This behavior is also present in the previous work of [6]. Visualizing δDNI over ϵ yields that the data points disperse very strongly downwards, especially in the lower angle range. From 25° the values scatter approximately between -10% and 1% when including 95% of all values. Since the DNI signal is the result of the actually

measured GHI and DHI signal, RSP's δDNI curve over ϵ must yield from the δDHI one, treated in the subsequent Section.

The azimuth angle can be identified as a secondary influence ($\rho = 0.25$), even though this dependency is not known from previous studies. An error in the physical alignment of the sensor over north can be ruled out since this was double-checked and small azimuth misalignment inaccuracies within ± 5° have no impact on RSPs, that rotate continuously [13, p.57]. The alignment of the resting shadowband to the north and not to the south also meets the requirements from [68, p.20]. The dependence of the measurement on the azimuth angle could theoretically also result from an incorrect leveling of the LI-COR 200R. However, the silicon sensor is still in the correct initial state, even after the measurement has been completed, as a check indicates (details on the check see Appendix B.3). Since all possible sources of error are eliminated, the correlation between the measurement deviation and the azimuth angle is assumed to be the result of the Sun tracker next to it partially shading the Sun. In this way, only a certain percentage of the DNI reaches the RSP and a disturbed (too low) measurement of the DNI occurs. These events are apparently not reliably sorted out during data preprocessing.

The SPN1's DNI estimation is mainly influenced by the circumsolar irradiance with a very strong correlation coefficient of $\rho = 0.76$ (Table 5.2). This dependence can be expected and moreover confirmed by [14]. As it has already been stated in Section 2.4, the SPN1's effective aperture (i.e. the angle from which radiation is directly received) is always greater than ±5° with a maximum angle of ±25°. As a result, the SPN1 includes a significant portion of the circumsolar irradiance in its DNI measurement. The percentage included will vary depending on the solar position [14] and the orientation of the SPN1 (the manufacturer does not give a specification). Further, secondary influences on the SPN1's DNI estimation cannot be detected, according to Table 5.3. Besides the strong correlation, a very distinctive dispersion can also be found for the influence of the circumsolar irradiance, since dispersion rises with increasing values of CSI.

When looking at the column for the MS-90 in Table 5.2, several high correlation coefficients can be identified, with the circumsolar irradiance being the greatest one. After the iterative adjusting of the data set, the MS-90 does not show any further, secondary dependencies (cf. Table 5.3). No detailed information exists on the technical design or physical properties of this DNI sensor, other than those given in [34], [33], and [37]. Nevertheless, the following considerations can be made. The MS-90 measures the DNI by scattering the direct radiation, that is incident on the rotating mirror and then reflecting it onto the pyroelectric sensor. As Fig 2.15 illustrates, this also happens with incident diffuse radiation, for instance, scattered by clouds, as long as these are within the mirror's symmetry plane. Anyway, in the latter case, the corresponding threshold value of 120 W/m^2 is not exceeded and the radiation is therefore not considered as DNI (see Fig 2.16 and cf. [36]). In the case of circumsolar irradiance's existence, a not inconsiderable amount of diffuse radiation comes from the immediate area around Sun and, thus, lies in the same spatial plane as direct radiation. This increases

(a) Visualization of the cloud enhancement effect, caused by thin clouds at the region around the sun disk.

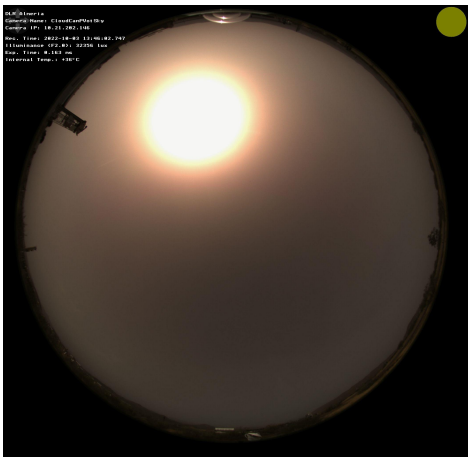

(b) Visualization of CSI, caused by high aerosol values.

Figure 5.7: Visualization of CSI and the cloud enhancement effect on ASI photographs. Both atmospheric conditions have different causes of origin but lead to a not inconsiderable amount of diffuse radiation, coming from the immediate area around the Sun.

the amount of incident energy on the sensor and leads to DNI's overestimation. At this point, another effect should be mentioned that is not directly investigated in this thesis, but which may erroneously show up as a high CSI value in the measurement: the cloud enhancement effect. As is shown in the two ASI photographs in Fig 5.7, both atmospheric conditions have different causes of origin but lead to a not inconsiderable amount of diffuse radiation, coming from the immediate area around the Sun. Thus, the setup for measuring CSI may often detect cloud enhancement effects as circumsolar radiation. Based on the speed of the clouds, the bursts might range from seconds to minutes [39]. The MS-90 in particular is sensitive to such effects resulting from such cloud constellations due to its measurement principle. It can either measure a too-high DNI value if the thin cloud lies within the symmetry plane of the mirror or, it interprets a cloud enhancement effect before the actual direct radiation as the maximum DNI value. For both cases, DNI is overestimated. Furthermore, CSI leads to a strong scattering of the measured values, which grows with higher values for CSI (between -12% and 20%).

Calculating all correlation coefficients for the measured DNI by the PyranoCam method, comes to the finding, that it is the DNI clear sky index $k_{c,\,DNI}$, which affects the accuracy in the most intense way. From visualizing δDNI over the main influence, it can be obtained that the PyranoCam method seems to have issues in estimating the DNI correctly when the sky differs from ideal clear sky conditions, respectively, when DNI is small. In these situations, it underestimates the DNI. Also, the dispersion of the measured values gets narrower, when $k_{c,\,DNI}$ converges towards 1. Since PyranoCam's DNI is calculated from its measured DHI and the reference GHI, the actual reason for the phenomenon described here is likely to be found in the DHI measurement in the subsequent Section.

Table 5.3: Comparison of the original and the newly calculated Spearman correlation coefficients for DNI, based on the relative measurement deviations and the meteorological influence factors. The main influences are colored in and the secondary influences are marked in . Secondary influences are characterized by a correlation coefficient $\rho > 0.2$ with the measurement deviation (on the adjusted data set).

	RSP		SPN1		MS-90		PyranoCam	
	Original	New	Original	New	Original	New	Original	New
Elevation Angle	-0.33	-0.02	0.07	-0.03	-0.03	-0.16	0.15	0.19
Azimuth Angle	0.32	0.25	0.02	-0.004	0.04	0.04	0.23	0.19
DNI Clear Sky Index	-0.04	-0.04	-0.63	-0.08	-0.59	-0.1	0.39	-0.05
Linke Turbidity	-0.29	-0.19	0.54	-0.05	0.44	-0.19	-0.10	-0.01
Ambient Temperature	-0.23	-0.08	0.31	0.005	0.17	-0.16	0.03	0.08
Effective Wavelength	0.15	0.05	-0.45	-0.06	-0.36	0.05	0.21	0.04
Circumsolar Irradiance	-0.04	-0.02	0.76	-0.07	0.68	-0.13	-0.13	0.18

5.2.3 Evaluation of the Correlation Coefficients for DHI

The following evaluation is based on the data set "Correlation Analysis (filtered for DHI < 20 W/m²)" from Table 3.6. In contrast to the DNI measurement, the RSP does not show a main influence factor for DHI, when relating to the interpretation rules from [66]. Nonetheless, the biggest influence is given by the elevation angle ϵ, too, with a small to moderate correlation coefficient of $\rho = 0.23$ (Table 5.4). That means the magnitude of RSP's deviation drops with increasing Sun elevation. Here, again, the reason is the already mentioned insufficient cosine correction. It has been stated in the previous Section, that the curve from RSP's δDNI over ϵ is related to the curve from RSP's δDHI over ϵ. This can be verified at this point; RSP underestimates DHI for low Sun elevation and therefore overestimates DNI.

Table 5.2 indicates, that SPN1 shows the strongest correlation with $k_{c,\,DNI}$ ($\rho = -0.51$. However, when plotting δDHI over the atmospheric conditions, it gets obvious that the azimuth angle α has a very strong influence on the measurement, too. As Fig 5.8 makes clear, the course of α over δDHI is not monotonic, and, hence, not spotted by Spearman's rank correlation coefficient. Compared to the influence of $k_{c,\,DNI}$ in Fig 5.9, the deviation resulting from the azimuth angle is bigger than the one from $k_{c,\,DNI}$: The 50^{th} percentile of δDHI ranges between a max. value of -6% and a min. value of -17% when plotted over α, and between a max. value of 0% and a min. value of -12% when plotted over $k_{c,\,DNI}$. Consequently, α is characterized as the main influence. The conspicuous course of the measurement deviation of the DHI over the azimuth angle was already detected in [14] and explained in Section 2.4. Nevertheless, the outcomes from calculating Spearman's rank correlation coefficients should not be rejected. In contrast to the DNI measurement, the SPN1 shows no relationship between DHI and circumsolar radiation, at least on the used data set[3]. Rather, in combination with the influence of the azimuth angle, the DNI clear sky index $k_{c,\,DNI}$ influences the DHI

[3] If time stamps with DNI < 100 W/m² are excluded, it is noticeable that the correlation with CSI also increases for δDHI. Thus, for a data set that covers a particularly large number of clear-sky days in the summer months, the results may vary. Also, see [14].

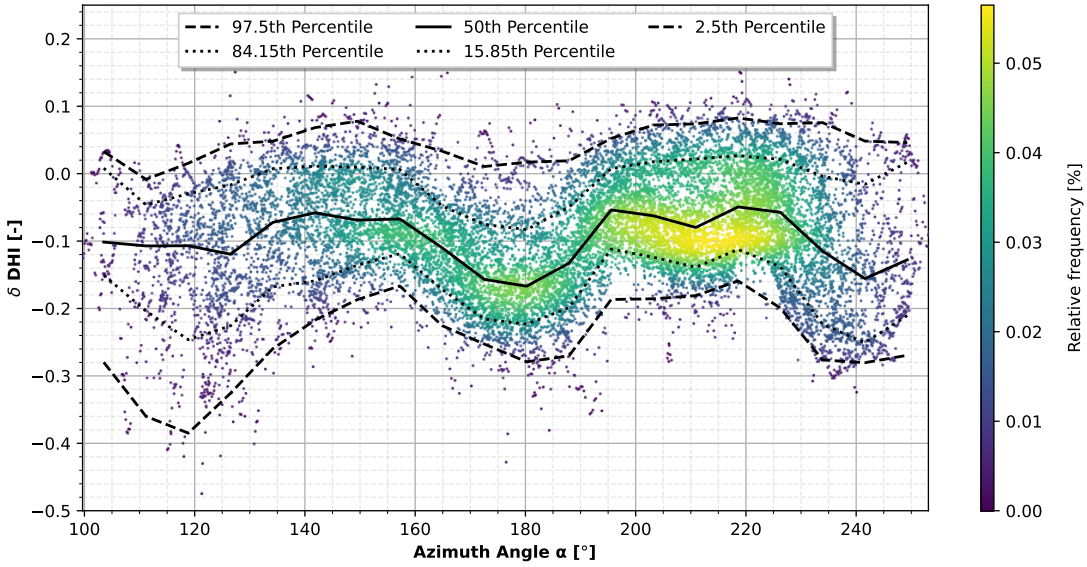

Figure 5.8: Influence of the azimuth angle on the SPN1's DHI measurement

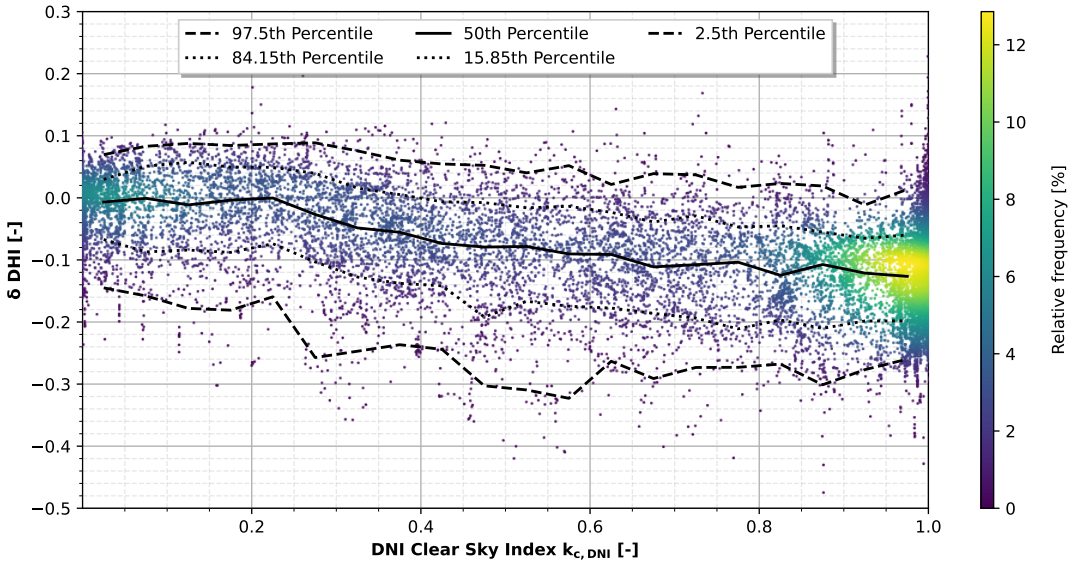

Figure 5.9: Influence of the DNI clear sky index on the SPN1's DHI measurement

measurement in the strongest way. The reason for this is also described in Badosa et al.'s study [14]; SPN1's spectral sensitivity, which is visualized in Fig 2.12, is not fully homogeneous but falls stepwise to the shorter wavelengths. Since the diffuse spectrum changes between clear sky and overcast conditions (Fig 2.6), SPN1's DHI measurement varies, too.

As was the case for the DNI measurement, the MS-90's DHI readings also show the greatest dependence on the circumsolar radiation ($\rho = $-0.67), whereby the elevation angle ϵ ($\rho = 0.29$), the ambient temperature ϑ_{amb} ($\rho = 0.30$), the DNI clear sky index $k_{c,\,DNI}$ ($\rho = 0.41$), as well as the effective wavelength λ_{eff} ($\rho = 0.29$), are all evaluated as meteorological secondary influences. At least for the DNI measurement, [34] explains that the MS-90 shows shortcomings

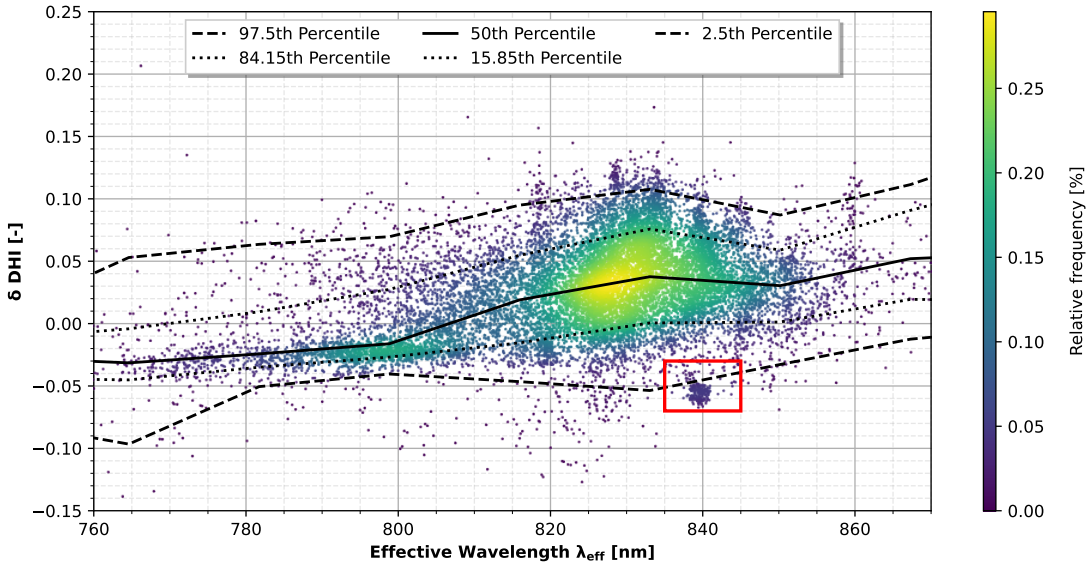

Figure 5.10: Influence of the spectral composition of light on the DHI measurement of the PyranoCam method

when it comes to low DNI situations. This knowledge clarifies the correlation with the $k_{c,\,DNI}$ for DHI.

PyranoCam's main influence factor for DHI is the DNI clear sky index $k_{c,\,DNI}$ ($\rho = 0.53$), likewise, the for DNI. It is noticeable, however, that the effective wavelength λ_{eff}, as a representative of the spectral composition of radiation, also has a high correlation coefficient of $\rho = 0.43$ with δDHI. At this point, the cause-effect logic should be considered. Although the parameter $k_{c,\,DNI}$ has a higher correlation coefficient, the cloudiness of the sky is the cause of a changing solar spectrum. As found before (cf. Chapter 4), PyranoCam apparently underestimates DNI in the presence of red clouds, and, hence, overestimates DHI. This assumption is verified by Fig 5.10, which shows a positive correlation between λ_{eff} and DHI deviation in conjunction with a positive correlation coefficient of $\rho = 0.43$. The dependence of the DHI measurement on λ_{eff} is probably caused by affecting the output signal's intensity of the three RGB color channels. A subsequent application of a correction function for the PyranoCam method is therefore recommended. The data point cloud, marked by the red rectangular in Fig 5.10, comes from the extremely high value of circumsolar radiation on 03/10/2022. The corresponding correlation coefficient after adjusting the data set is $\rho = 0.17$ and, thus, corresponds to a weak to moderate correlation. Although a value of $\rho = 0.2$ is used as a threshold for this evaluation in order to define a secondary influence, it should not go unnoticed that high values of CSI lead to an underestimation of the DHI, despite the increasing red portion of the light's spectrum. Additionally, only a few data points, for high-measured CSI values ($CSI > 30\,W/m^2$), exist. A larger data set covering a broader range of atmospheric conditions could therefore produce a correlation coefficient $\rho \geq 0.2$ for CSI.

Table 5.4: Comparison of the original and the newly calculated Spearman correlation coefficients for DHI, based on the relative measurement deviations and the meteorological influence factors. The main influences are colored in and the secondary influences are marked in . Secondary influences are characterized by a correlation coefficient $\rho > 0.2$ with the measurement deviation (on the adjusted data set).

	RSP		SPN1		MS-90		PyranoCam	
	Original	New	Original	New	Original	New	Original	New
Elevation Angle	0.23	0.01	-0.03	0.16	0.07	0.29	0.18	0.06
Azimuth Angle	-0.09	-0.08	0.08	0.13	-0.04	0.01	-0.04	-0.11
DNI Clear Sky Index	-0.003	-0.05	-0.51	-0.02	0.54	0.41	0.53	0.04
Linke Turbidity	0.04	-0.02	0.02	-0.02	-0.43	-0.02	-0.17	-0.11
Ambient Temperature	0.1	-0.01	0.001	0.13	-0.11	0.30	0.16	0.07
Effective Wavelength	0.19	0.18	-0.34	0.03	0.41	0.29	0.43	0.05
Circumsolar Irradiance	0.03	0.01	-0.004	-0.12	-0.67	0.03	-0.25	-0.18

5.3 Discussion of the Correlation Analysis

Summarizing the findings from the correlation analysis, the following can be stated:

The presence of high turbidity values leads to noticeable data point clouds with large deviations in the scatter density plots for all sensors except the RSP. However, the data set used covers only a few days with extreme turbidity values greater than 8, which is why a general association between high turbidity values and increasing dispersion width, can only be suspected.

For SPN1, it was assumed, based on [14] and [6], that this radiometer shows an increased dependence on the circumsolar radiation for the DNI measurement, due to the increased effective aperture. This supposition can clearly be confirmed, as CSI represents the main influence for DNI. The hypothesis set up in Chapter 4, that there has to be some meteorological influence existing or appearing stronger in Tabernas than in Payerne, which negatively influences the SPN1's DNI measurement can hence be maintained. However, since no turbidity data are available for Payerne, no verification can be made.

The dependence of the SPN1 on the effective wavelength and the cloudiness of the sky, when measuring DHI, can also be reproduced in this work, as can the non-monotonic main influence of the azimuth angle.

The MS-90 exhibits CSI for both, the DNI and DHI measurement, as the main influence. Additionally, the elevation angle, the DNI clear sky index, the ambient temperature, and the effective wavelength represent secondary influences for DHI. Expected and confirmed was the dependence of MS-90's δDHI on $k_{c,\,DNI}$ [34].

As expected, the RSP shows the main dependence on the elevation angle. This behavior was already observed in [6] and [19], but should have been eliminated by applying the cosine correction. Furthermore, since the correction function is only applied to the GHI, an additional correction for the DHI signal is recommended, if possible. A dependence of the DNI

signal of the RSP on the azimuth angle could be disproved. The correlation follows with high probability from the partial shadowing of the RSP by the Sun Tracker placed next to it.

Based on the anomalies in the scatter density plots of the PyranoCam method investigated in the performance analysis, it was hypothesized that the radiometer overestimates the DHI due to a higher weighting of the solar spectrum in the red region. This assumption is supported by the main influence $k_{c,\,DNI}$ as it correlates strongly with λ_{eff}. Affecting the output signals' intensity of the RGB color channels is suspected. The predicted influence of the haze and the soiling of the lens on the DNI measurement cannot be verified in the correlation analysis. Rather, the DNI clear sky index $k_{c,\,DNI}$ interferes with PyranoCam accuracy.

6 Conclusion

The present thesis investigated the performance of a total of four radiometers for solar application by using the deviation metrics RMSD, MAD, BIAS, and R^2-Score, placing them in relation to each other and determining the measurement uncertainty in the form of a 95% prediction interval. Furthermore, this thesis dealt with the question of whether, and if true, to what extent the DNI and DHI measurement of the individual sensors is influenced by external atmospheric conditions. Examined were the radiometers:

- SPN1
- MS-90
- RSP
- PyranoCam

Considered meteorological parameters were:

- Ambient Temperature ϑ_{amb}
- Elevation Angle ϵ
- Azimuth Angle α
- Circumsolar Irradiance CSI
- Linke Turbidity T_L
- Effective Wavelength λ_{eff}
- DNI Clear Sky Index $k_{c,DNI}$

The rough procedure was as follows:

- Data acquisition was made for both, radiometers as well as meteorological parameters, on CIEMAT's PSA in the time from 01/08/2022 to 11/12/2022.
- The plausibility and accuracy of the data were ensured, among other things, with the help of manual and automatic daily data checks. In addition, all sensors were cleaned on a weekday basis. A zenith filter of 85° was applied to the data set.
- In the entire data set for the performance and correlation analysis, only time stamps were evaluated for which a value was available for all the parameters examined.

- Due to the distance between the locations of the radiometers and the WISERs (for measuring the spectral composition of radiation), only stable sky conditions were available for the correlation analysis, where the DNI varied by less than 10 W/m^2 in a 15-minute period.
- The metrics were evaluated in the period from 01/08/2022 to 11/12/2022. Since the measurement deviations did not show a normal distribution, the measurement uncertainty was specified using a 95% prediction interval.
- The correlation of the measurement deviation to the atmospheric conditions was investigated mathematically and visually with a combination of Spearman's rank correlation coefficients and scatter density plots due to a non-existing normal distribution. Examined were time stamps in the period 01/10/2022 to 11/12/2022, as measurements of CSI were only available since October.

With regard to performance, based on the RMSD and MAD, it can be stated that the PyranoCam method, newly developed by DLR, is the most suitable overall for DNI measurement (RMSD = 3.4%, MAD = 2.4%). In addition, it shows nearly no BIAS (0.2%). The physics-based method is followed by the RSP, which has already been investigated in many previous studies, and the still relatively unknown MS-90. RSP exhibits an RMSD of 5.7% and a MAD of 3.8%, MS-90 of 11.8% (RMSD), and 7.6% (MAD). The SPN1 performs worst (RMSD = 13.2%, MAD = 10.4%). In terms of measurement uncertainty, the RSP, which provides the most accurate results for DNI measurement (-39.2 to 11.4 W/m^2), is closely followed by PyranoCam (-35.5 to 26.2 W/m^2). Since RSP's MAD results nearly completely from its BIAS, it is plausible, that it's PI_{95} is narrower than the one from PyranoCam, even though PyranoCam shows a smaller MAD value for DNI. The same applies to the MS-90 and the SPN1, whose uncertainties are between -60.9 and 135.6 W/m^2 for MS-90 and -32 and 140.2 W/m^2 for SPN1.

When measuring DHI the ranking changes. RSP performs best, with an RMSD of 4.7% and a MAD of 3.6%. PyranoCam is in second place(RMSD = 4.8%, MAD = 3.5%), and SPN1 (RMSD = 13.5%, MAD = 10.2%) and MS-90 (RMSD = 22.9%, MAD = 14.5%) show due to their high RMSD and MAD values the worst results. Nevertheless, the MS-90 shows almost no BIAS (-1.3%), compared to the other radiometers. In terms of measurement uncertainty, however, the order of the sensors does not change, although the values do. RSP measures DHI within an uncertainty of 16.7 to 3.2 W/m^2. For PyranoCam a range between -8.3 and 18 W/m^2 was determined. SPN1's PI_{95} is within -53.2 and 11.8 W/m^2, and the largest measurement uncertainty occurs when measuring DHI with the MS-90 (-71.4 to 56.2 W/m^2).

Examining the evolution of the RMSD and MAD over time resolution reveals that, averaging the sensor data to 10 minutes provides a good compromise between temporal resolution and accuracy of the data, as long as the time resolution is not specified. Furthermore, it was found that the MS-90 in particular seems to be susceptible to rapidly changing atmospheric conditions.

The results for the correlation analysis agree with almost all findings from the performance analysis and the detection of anomalies in the scatter density plots. Thus, the PyranoCam method is most strongly influenced by the DNI clear sky index, which reflects the cloudiness level, in both the DNI and DHI measurements. However, since the cloudiness of the sky has a significant influence on the spectral composition of the radiation, it is assumed that the overestimation of PyranoCam's DHI is presumably caused by a higher weighting of the solar spectrum in the red region. The RSP shows for both, the DNI and DHI measurement, a moderate dependence on the Sun's elevation angle, which is assumed as a shortcoming in the respective correction function of the silicon sensor. Because of its technical design and the shortcoming in the spectral response, the circumsolar radiation distracts SPN1's DNI measurement the most. For DHI it is the DNI clear sky index representative for the effective wavelength, which marks the main influence. The last sensor evaluated is the MS-90. Not much is known about its technical details at the moment. However, based on the fundamentally described measurement principle, it seems plausible that the circumsolar radiation is the main influence here for the measurement of both the DNI and the DHI.

7 Possible Sources of Error and Outlook

The work presented here is not free of potential sources of error. Some of these were accepted at the beginning of the work, while other suggestions for improvement emerged during data collection and processing. Regarding the hardware and the physical measuring setup, the possible shortcomings are as follows:

- The test stand is located on a former scrap yard on CIEMATS's PSA. Therefore, until a big clean-up event on 07/10/2022, there was a not insignificant amount of glass and fragments of mirrors lying around on the floor, which could have influenced the measurement of all sensors except the WISERs by reflections.
- As described in the thesis, data logger programs were updated during the ongoing measurements.
- The measuring apparatus for circumsolar irradiance was installed during the ongoing measurements and the GHI pyranometer was relocated.
- The sun tracker is located close to the test sensors. This caused shading of the RSP and maybe other sensors.

With respect to the evaluation of the data, the following possible sources of errors and shortcomings can be stated:

- The period under consideration of 4.5 and 2.5 months for the performance and correlation analysis is too short to obtain representative results. Even if the behavior of the radiometers is consistent with previous works and the results from the performance and correlation analysis are consistent, a longer period is needed to include a wide range of weather conditions, such as dusty conditions, rainfall, strong winds, changing temperatures as well as more extreme elevation and azimuth angles.
- The distribution of the measured and determined values for the meteorological parameters is also not homogeneous, as the respective histograms in the Appendix B.3 make clear. For instance, it was stated by [14], that SPN1 might show some shortcomings for small zenith angles. The respective histogram shows, however, that only an angle range between 40° and 85° is covered instead.
- On top of that, It is questionable whether extremely variable weather conditions as listed above even occur in such a semi-desert climate as Tabernas.

- Sporadic large outliers were detected for the RSP, due to the sun trackers' shadowing. For this reason, it is recommended to raise the threshold for an invalid measurement.
- Since the WISERs are set up almost 840m away from the test sensors, only stable conditions could be considered for the correlation analysis within the scope of this thesis. Unstable conditions are characterized by, among other things, rapidly changing DNI irradiances. In order to determine the DNI correctly under such conditions, a fast response time of the sensors is required.
- Additionally, the comparison of valid values and NaN-values in the histograms in Appendix B.3, indicate, that there exists a heterogeneous or negative skewed distribution of the valid timestamps over the hours per day. Thus, not all times of day are captured in the correlation analysis in the same intensity.

From the possible sources of error in the physical measurement set-up as well as data processing and evaluation presented here, several potentials for improvement arise for a subsequent study covering at least one year. Maintenance measures of the radiometers can never be excluded. However, further improvements to the measurement setup, such as those carried out in this study, should now be fully completed. Only the sun tracker has to be moved further to the east to prevent shading of the adjacent radiometers. It is also recommended to install the WISER spectroradiometers on the actual test site. This way, fewer time stamps have to be filtered out and unstable conditions can also be considered in the correlation analysis. Furthermore, the following additional and complementary measures are recommended for the further investigation of the research questions:

- Generally speaking, this study should be carried out at another site in addition to Tabernas to ensure the broadest possible coverage of each meteorological influence parameter.
- Since the influence of high turbidity values in the individual scatter density plots were particularly noticeable, it is also recommended that this will be investigated more closely. High turbidity values are present in Tabernas, especially during the summer months.
- Furthermore, the influence of the cloud enhancement effect on the DNI measurement of the MS-90, in particular, was predicted. Therefore, in a subsequent study, this effect should additionally be considered as a separate influencing factor.
- The MS-90 should also be checked for its dependence on rapidly changing irradiation and meteorological conditions. The PyranoCam method, on the other hand, suggests a shortcoming in the spectral response. This hypothesis should also be tested in a subsequent study.

Finally, this analysis shown here should ideally also be carried out for the GHI as well as the GTI. In the end, the big idea behind everything is to develop a model that interested

applicants can use as a guide to select the right radiometer depending on the location, the area of application, and the financial investment.

A Additional Explanations

A.1 Air Mass

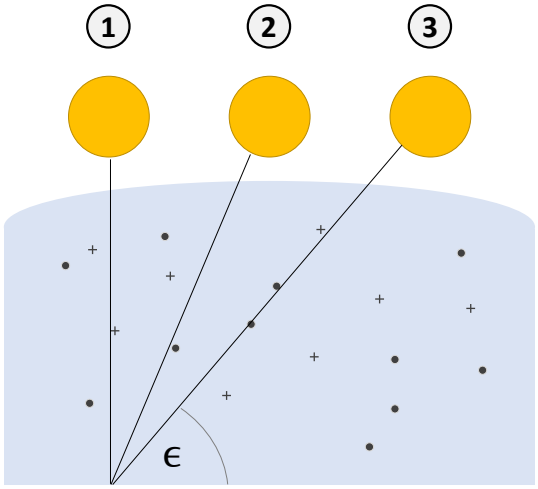

Figure A.1: Illustration of the mass factor. Position (1) indicates the smallest air mass value of AM_1 at 90°. In position (2) the air mass corresponds to the defined standard of $AM_{1.5}$ and in position (3) the sun is somewhere between $\epsilon = 0°$ and ϵ=90°, indicating a variable air mass value (AM_x).

As already described in Section 2.1, the solar spectrum inside and outside the atmosphere differ due to absorption losses, among other things. Consequently, the strength of the absorption is related to the distance that the light has to travel through the atmosphere to reach Earth's surface. Of course, this distance constantly changes with the height of the Sun in the sky, or with its angle of elevation ϵ, respectively. One parameter for describing the distance traveled is the so-called air mass factor AM_x. An air mass of 1 is defined when the Sun is exactly at a 90-degree angle to Earth's surface [13]. As the angle increases or decreases, the air mass factor changes:

$$AM_x = \frac{1}{\sin \epsilon} \tag{A.1}$$

This context is illustrated in Fig A.1. In a clear sky, at a sun height of 41.8°, and on a plane tilted 37° towards the sun, an air mass value of $AM_{1.5}$ is defined. The corresponding spectrum (visible in Fig 2.1) provides an overall irradiance of 1000 W/m². It has been defined as the standard spectrum for the categorization of photovoltaic modules [3].

A.2 ISO 9060

ISO 9060 describes and classifies instruments for the measurement of radiation for solar applications. The respective quality criteria used for classification into the three quality classes (secondary standard, first or second-class pyranometer) are explained in the following Sections.

A.2.1 Response Time

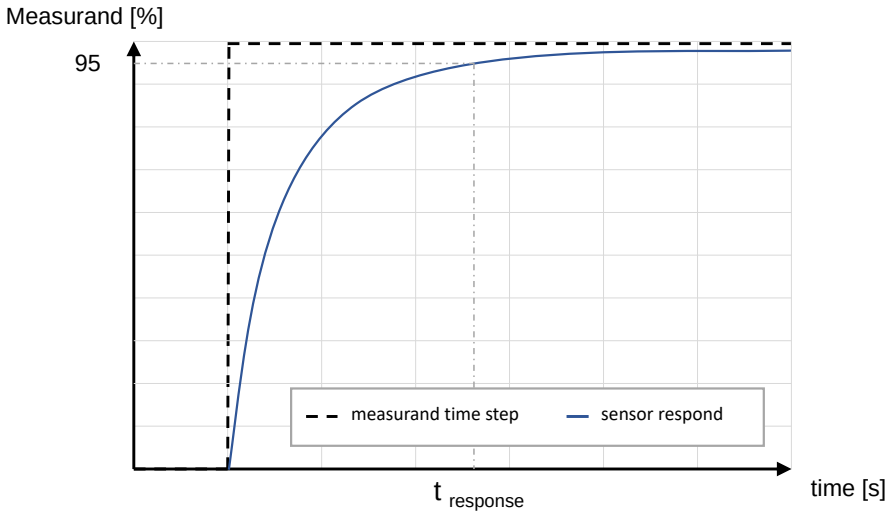

Figure A.2: Exemplary illustration of a sudden change of the measured variable and the corresponding sensor's response time. This figure was created by the author himself but inspired by [69, p.30]

A sensor or an instrument always needs a certain time to react to a change in the parameter it measures. While photodiodes have a very fast response time ($\approx$ 1ms), the thermal compensation process of thermal sensors is comparatively slow (<5s) and can only be defined in a complex way. Since, following the laws of control engineering, a system can respond differently to a step change (possible are, for example, a time-delayed step response or a PT1 behavior as shown in Fig A.2), the response time of a sensor is defined as a finite time step after which the measured value has grown to 95% of the final value [15] [69, p.28ff] [27, p.4].

A.2.2 Zero Offset

Even when there is no irradiation by the Sun, zero offsets in pyranometers' outputs are values that remain constant. They can originate from a variety of sources. [70]. The majority of them may be linked to thermal gradients or temperature variations within the device. As a rule, a distinction is made between three possible causes of zero offset, which are listed in ISO 9060 as a), b) and c) [15]. Origin a) is the offset due to thermal radiation and is also influenced by several other meteorological parameters such as wind, rain, or shadow. Origin b) refers to

the offset, which can be caused by fast temperature changes: Temperature gradients inside the instrument can result in offsets in the output signal when there is a sudden drop or peak in the ambient temperature, since certain components of the pyranometer may change their own temperature more quickly than others. This might happen in the early or late hours around sunrise or sunset and can also be influenced by external factors. Finally, internal electronics and HVU can also cause zero offsets, as they are used to avoid dew and frost on the sensor's dome [70]. The zero offsets, however, can still be substantial in some low-light situations, such as those that arise at sunset or sunrise or when detecting diffuse radiation with a shadow band [70].

A.2.3 Non-Stability and Non-Linearity

The non-stability criterion means the change in responsivity per year expressed in percentage [16, p.266]. On the other hand, when considering the irradiance rising between 100 W/m^2 to 1000 W/m^2, the relative deviation at 500 W/m^2 is known as the non-linearity [15, p.6].

A.2.4 Directional Response

The sensor's output signal varies with the zenith angle ζ of the incident direct radiation. This variation is called the angular, directional or cosine response. The name "cosine response" comes from Lambert's cosine law (Equation A.2), which basically states that $DNI_{hor.}$, measured on a horizontal plane, decreases proportionally to the cosine of the zenith angle ζ [71]:

$$DNI_{\text{hor.}} = DNI * cos(\zeta) \tag{A.2}$$

An ideal sensor would thus have a true angular response. Since such an ideal instrument does not exist, the quality of the glass domes, as well as the spectral and spatial homogeneity of the thermopile detector, control, and influence the angular response of thermopile pyranometers [27, p.5]. Silicon sensors, on the other hand, employ plastic diffusers to deliver a consistent cosine response at various Sun angles [29]. However, these radiometers are usually provided with a cosine correction.

A.2.5 Spectral Error

A spectral error results from the heterogeneous sensitivity of the sensor over the entire wavelength range of the solar spectrum. While thermopile sensors, for instance, have a near homogeny spectral response (between 280nm to 2800nm), silicon sensors do not. They can detect wavelengths in the range between 400nm and 1200nm and are more sensitive to wavelengths in the range between 800 and 900 nm than to wavelengths outside this range. As a result, their spectral response is not flat [27, p.5], and requires corrections.

A.2.6 Temperature Response

The temperature response is defined as the relative deviation due to an increasing or decreasing ambient temperature between 10°C to 40°C. The point of reference is given at 20°C [15]. According to [27, p.4], in thermopile pyranometers as opposed to silicon devices, the impact of temperature on the radiometer's signal is less significant, since the temperature has an influence on the short circuit current of silicon-based sensors; it records greater values at higher temperatures, which are not that easy to compensate, as it is for thermopile sensors. It typically rises by 0.15%/°C [3, p.104].

A.2.7 Additional Signal Processing Errors

As [72] points out, signal processing by data loggers also contributes to the measurement accuracy of any sensor. For this reason, a radiometer's data processing error has to be within a specific range to fulfill the criterion of a secondary standard, first or second-class pyranometer [72, p.4].

A.3 Calculation of the Influence of the MS-90's Oscillation on the RMSD for DNI

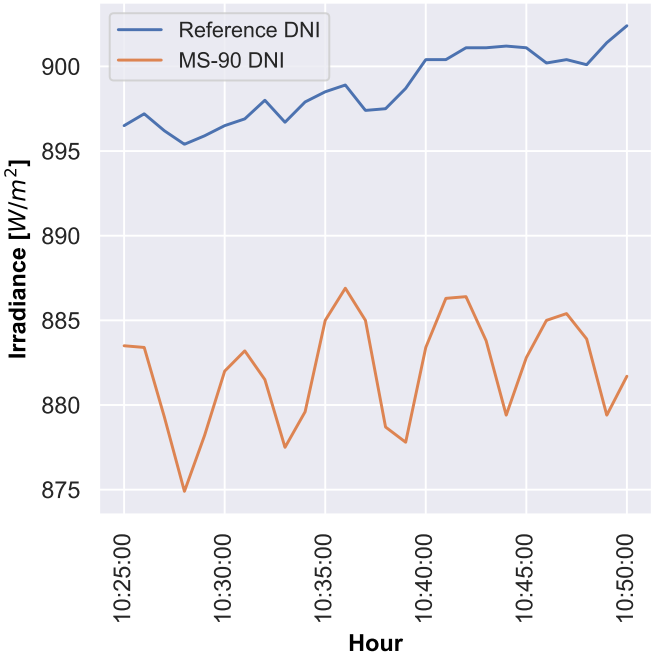

Figure A.3: Visualisation of the noise of the MS-90 DNI signal

A visual inspection of the MS90's DNI signal in Fig A.3 reveals, that the oscillation can be approximated by a sine function of the form:

$$10\mathrm{W/m^2} * \sin(6\mathrm{min}^{-1} * 2 * \pi * t)$$

It is, hence, characterized by an amplitude A of 10 W/m² and a frequency f = $6\mathrm{min}^{-1}$. Calculating the RMSD for a 1-minute resolution, based on the adjusted data set from Table 3.6, gives a value of 53.4 W/m². A transfer of the facts from [73, Section 4.3.6] to the present question yields:

$$\mathrm{RMSD}_{\mathrm{total}}{}^2 = \mathrm{RMSD}_{\mathrm{oscillation}}{}^2 + \mathrm{RMSD}_{\mathrm{no\ oscillation}}{}^2 \tag{A.3}$$

Here, the expression $\mathrm{RMSD}_{\mathrm{oscillation}}$ corresponds to the RMSD value given by the sine wave oscillating around its arithmetic mean. This can be calculated by determining the root mean square (RMS), according to [74]:

$$\begin{aligned} \mathrm{RMSD}_{\mathrm{oscillation}} &= A * \sqrt{\frac{1}{2}} \\ \mathrm{RMSD}_{\mathrm{oscillation}} &= 10\mathrm{W/m^2} * \sqrt{\frac{1}{2}} \\ \mathrm{RMSD}_{\mathrm{oscillation}} &= 7.07\mathrm{W/m^2} \end{aligned} \tag{A.4}$$

Based on Equation A.3, the missing parameter $\mathrm{RMSD}_{\text{no oscillation}}$ is calculated:

$$\begin{aligned} \mathrm{RMSD}_{\text{no oscillation}} &= \sqrt{\mathrm{RMSD}_{\mathrm{total}}{}^2 - \mathrm{RMSD}_{\mathrm{oscillation}}{}^2} \\ \mathrm{RMSD}_{\text{no oscillation}} &= 52.9\mathrm{W/m^2} \end{aligned}$$

Thus, it can be seen that the influence of the sinusoidal noise of the MS-90 signal on the magnitude of the RMSD is negligible.

B Additional Figures

This chapter contains all figures that do not appear in the body text due to their relevance or size. Additional figures are arranged chronologically for Chapters 3, 4, and 5.

B.1 Figures for Chapter 3

The two Figures B.1 and B.2 support the explanations from Section 3.2.3 in the thesis. The first of the two figures shows the comparison of valid values (dark blue) and NaN-values (gray) for the data set of the performance analysis and the three respective data sets of the correlation analysis and marks in yellow the times around sunrise and sunset. Ideally, the number of available values should naturally exceed the number of NaN values and also have a homogeneous distribution over the hours of the day. This is true for Fig B.1a, but not for the remaining three. Data for the correlation analysis indicate a negative skew. This should be taken into account in the discussion of errors in Chapter 7.

Fig B.2, on the contrary, represents the comparison between expected (light-blue) and available (dark-blue) timestamps. What is particularly striking, are the data gaps. These result from invalid measurements or sensor outages. As already described in Chapter 3, all data for a timestamp are rejected if the data of one or more sensors are invalid. The low availability of data for the correlation analysis (Fig B.2b, B.2c and B.2d) is primarily due to the rejection of unstable conditions, to ensure valid spectroradiometer data, as described in Section 3.2.2.1.

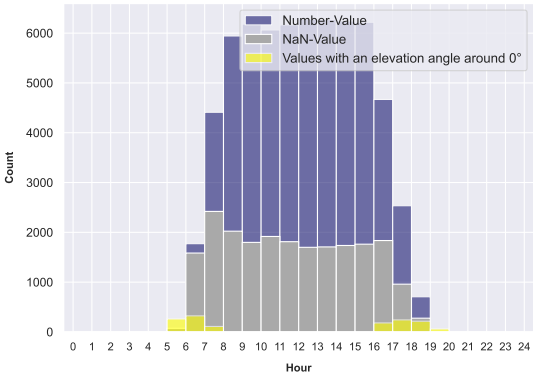

(a) Data for Performance Analysis

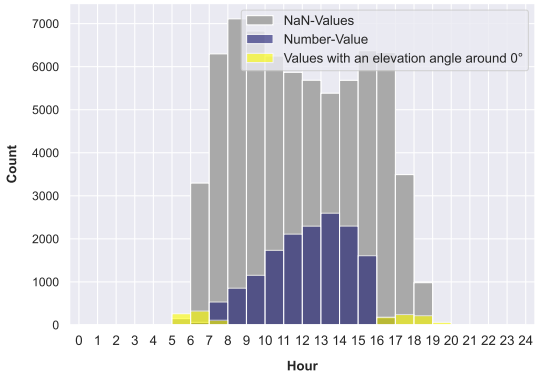

(b) Data for Correlation Analysis without further filter

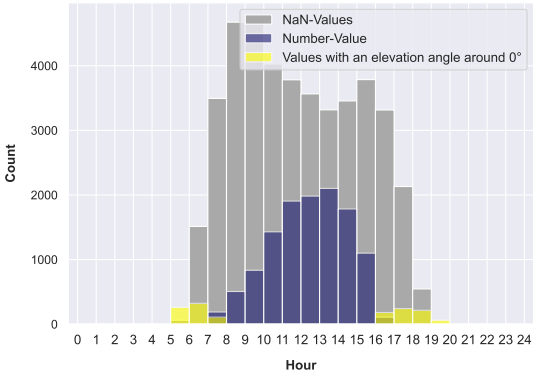

(c) Data for Correlation Analysis with DNI filter

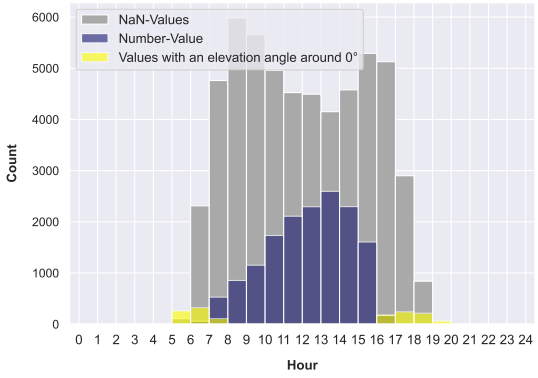

(d) Data for Correlation Analysis with DHI filter

Figure B.1: Distribution of the data of the different data sets over hour per day and comparison of respective NaN-values and valid timestamps

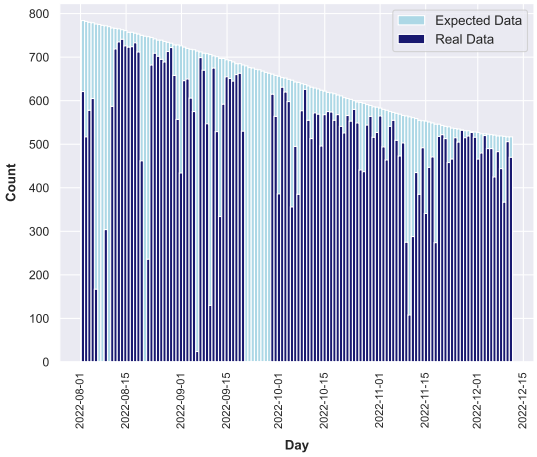

(a) Data for Performance Analysis: 75% of the expected timestamps are available.

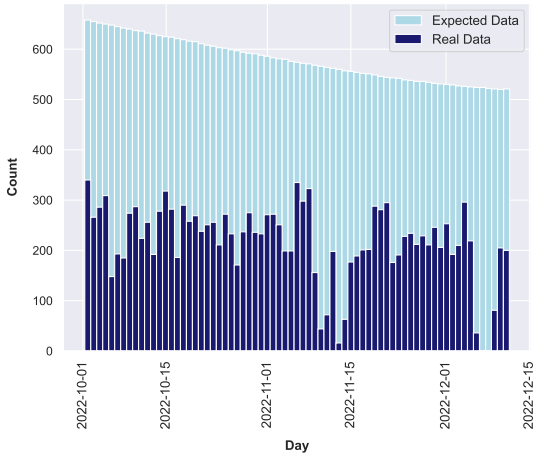

(b) Data for Correlation Analysis without further filter: 37.48% of the expected timestamps are available.

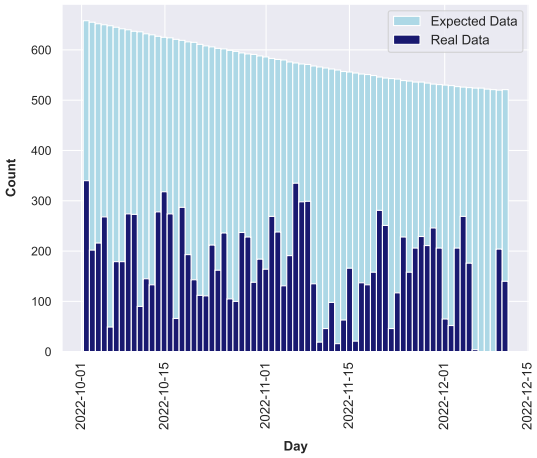

(c) Data for Correlation Analysis with DNI filter: 29.05% of the expected timestamps are available.

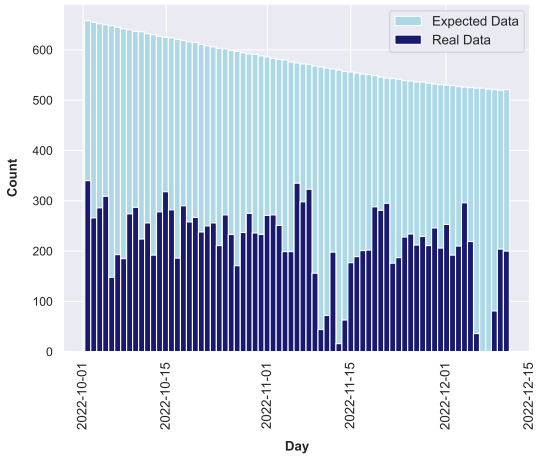

(d) Data for Correlation Analysis with DHI filter: 37.46% of the expected timestamps are available.

Figure B.2: Comparison of the expected and available data for each data set

B.2 Figures for Chapter 4

The three Figures B.3, B.4 and B.5 are the equivalents of Fig. 4.13, showing histograms and probability plots for ΔDNI and ΔDHI, respectively, for the RSP, MS-90, and PyranoCam. The figures prove that the measurement deviations of the radiometer are not normally distributed. The values for skewness and kurtosis also given support this.

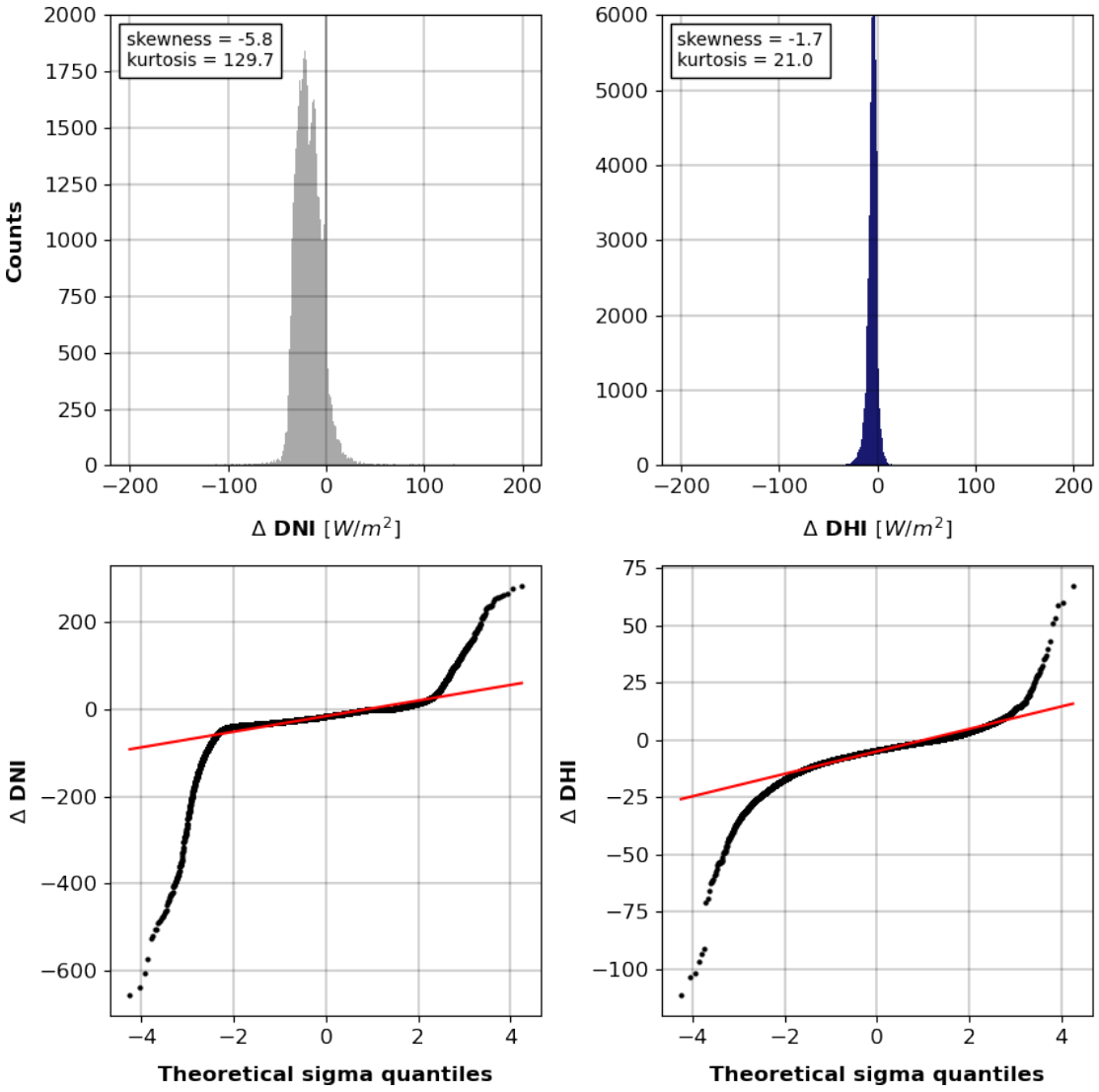

Figure B.3: Graphical check of the DNI and DHI measured values of the RSP for normal distribution using histograms, probability plots and specifying the skewness and kurtosis

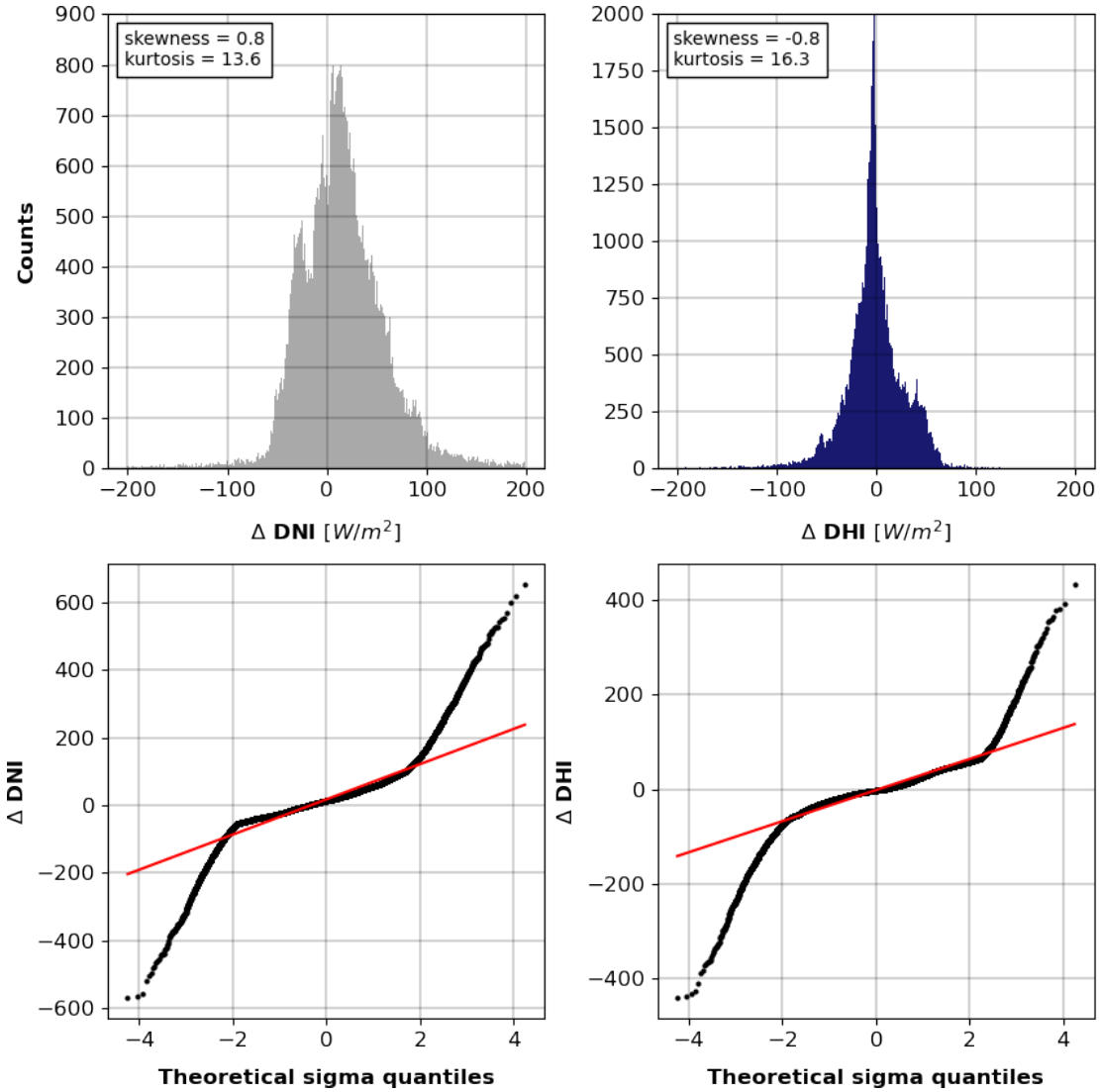

Figure B.4: Graphical check of the DNI and DHI measured values of the MS-90 for normal distribution using histograms, probability plots and specifying the skewness and kurtosis

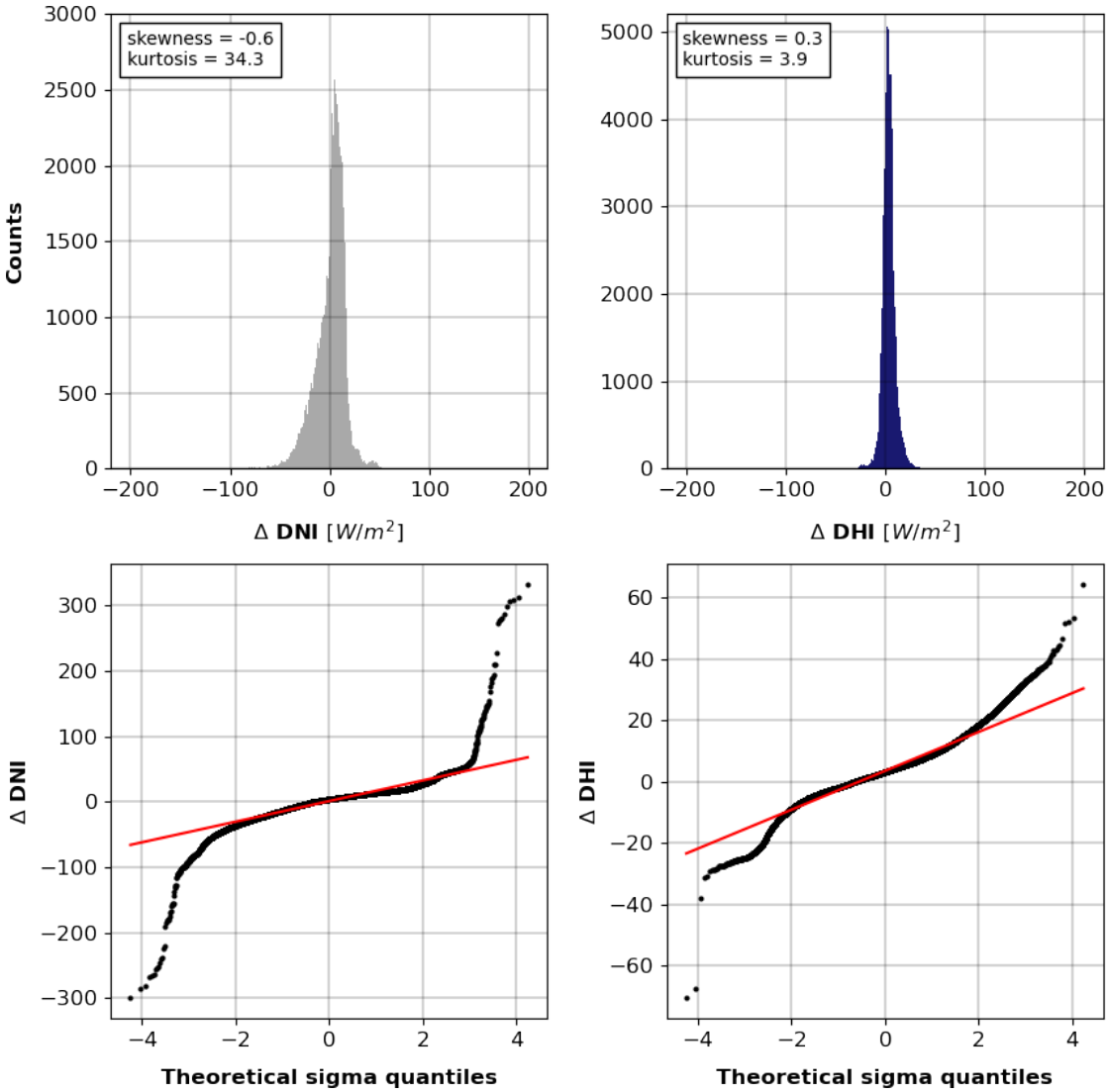

Figure B.5: Graphical check of the DNI and DHI measured values of the PyranoCam for normal distribution using histograms, probability plots and specifying the skewness and kurtosis

B.3 Figures for Chapter 5

Scatter Plot Matrix of the Meteorological Parameters

In the scatter plot matrix in Fig B.6 all meteorological parameters are juxtaposed. The figure is intended to illustrate the correlation and dependence of the parameters on each other, besides the calculated Spearman coefficients in Fig 5.1.

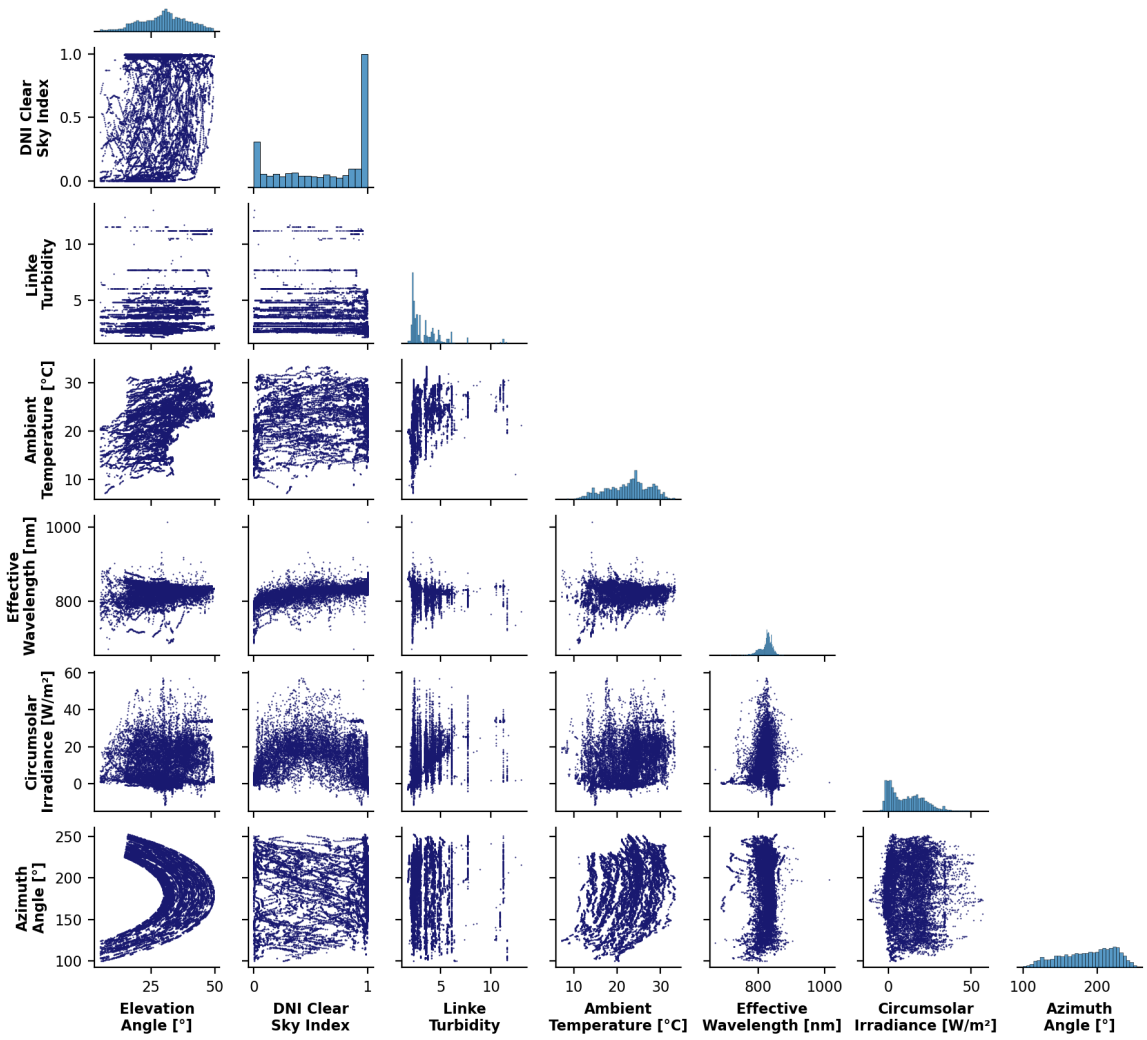

Figure B.6: Scatter plot matrix of the meteorological parameters

Histograms of the Available Data for all Meteorological Parameters

The histograms in Fig B.7 to B.12 serve the transparency of this thesis and demonstrate shortcomings of the available data sets in case of non-homogenous distributions. For instance, Fig B.7 indicates, that only zenith angles between 40° and 85° are considered. Similarly, the distribution for the DNI clear sky index is very one-sided, as shown in Fig B.11. The availability of the atmospheric conditions shown here serves the discussion of errors and the outlook in Chapter 7.

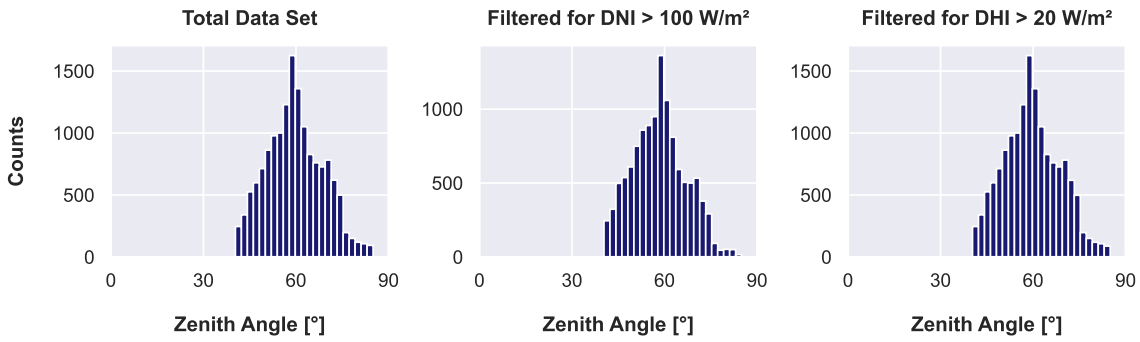

Figure B.7: Histograms of the available zenith angle data for the correlation analysis

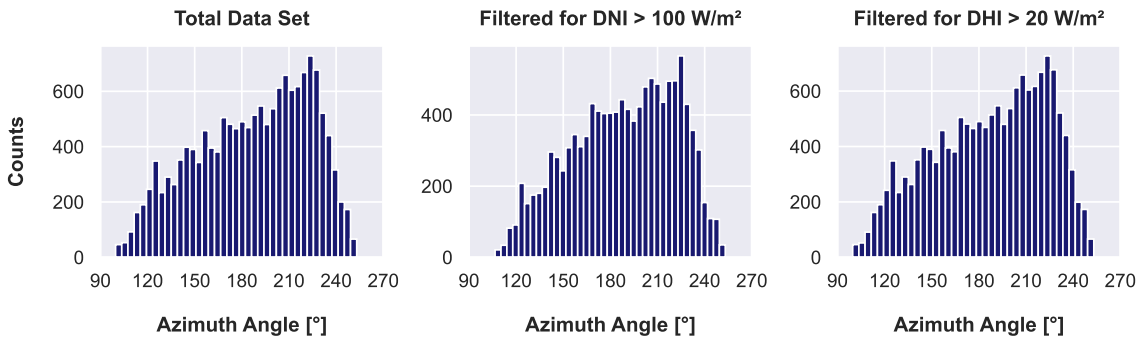

Figure B.8: Histograms of the available azimuth angle data for the correlation analysis

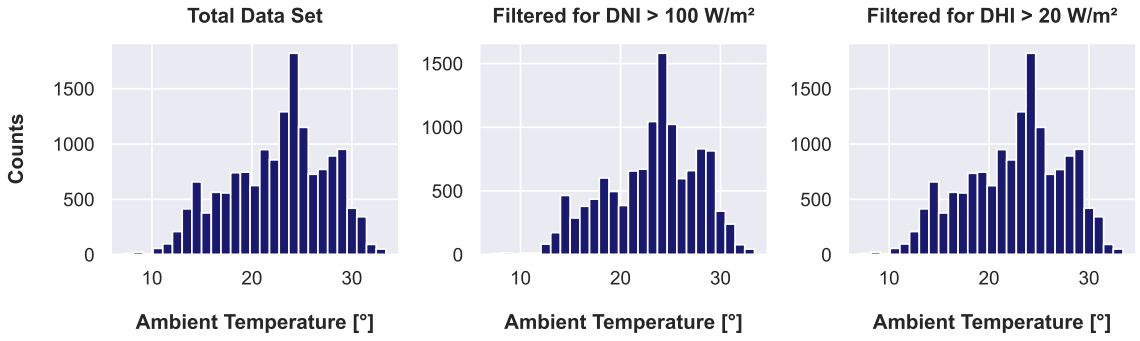

Figure B.9: Histograms of the available temperature data for the correlation analysis

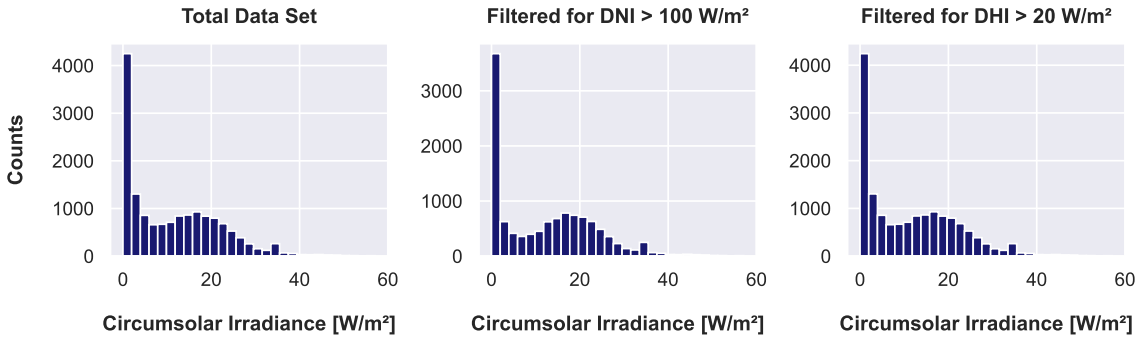

Figure B.10: Histograms of the available circumsolar irradiance data for the correlation analysis

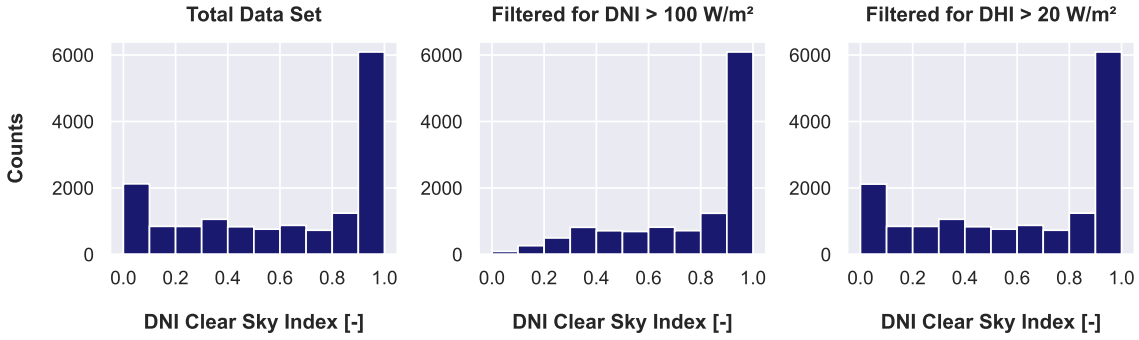

Figure B.11: Histograms of the available $k_{c,\,DNI}$ data for the correlation analysis

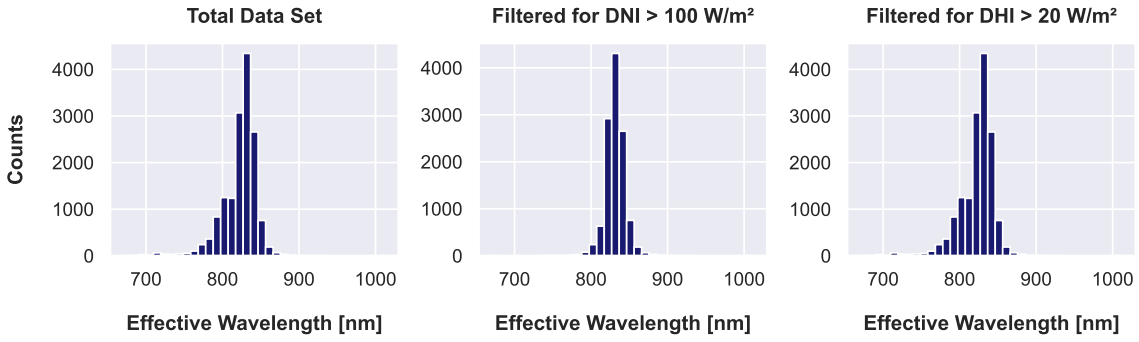

Figure B.12: Histograms of the available effective wavelength data for the correlation analysis

Investigation of Anomalies in Scatter Plots

The figures presented here refer to the investigation of anomalies in the plot of measurement deviation over meteorological influence. In Section 5.1, MS-90's DNI over the circumsolar radiation was used for illustration. Fig B.13 and B.14 show the RSP's δDNI and δDHI over the Linke Turbidity and indicate the presence of extreme high turbidity values (T_L>8) on 03/10/2022. This day thereby also leads to the anomalies, visible in Fig B.15, B.16 and B.17, marked by the red rectangular. Fig 5.2 on the other hand, illustrates the high outliers for RSP's δDNI over the azimuth angle, because of the sun tracker's shading.

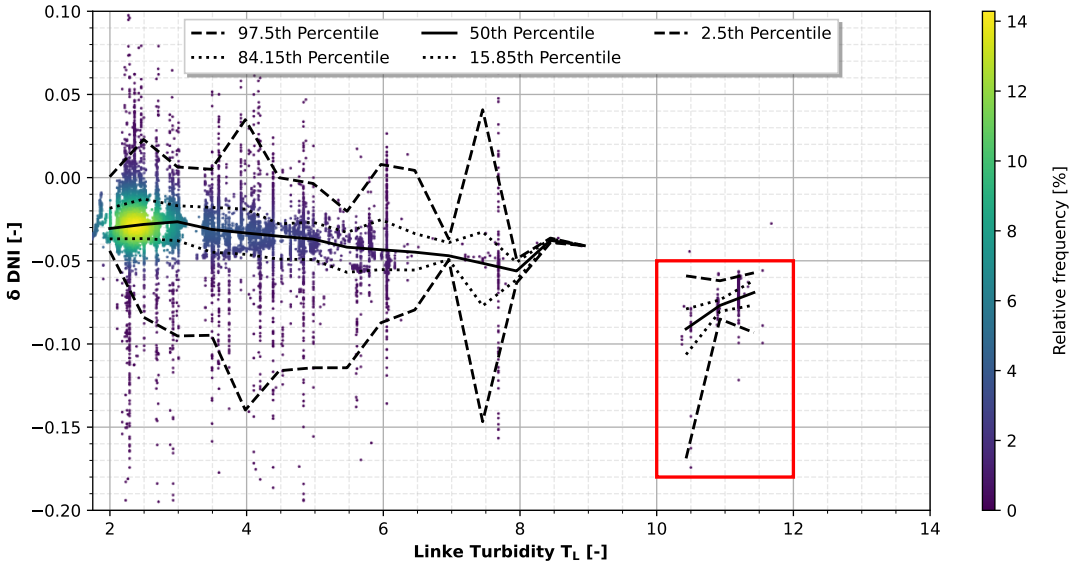

Figure B.13: Anomalies in RSP's DNI measurement under the influence of the Linke turbidity

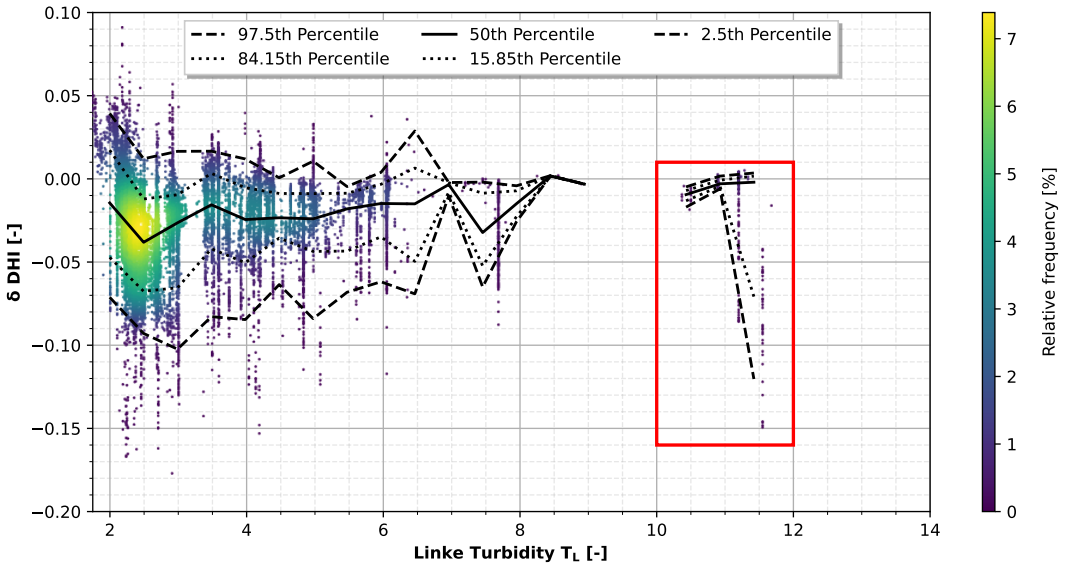

Figure B.14: Anomalies in RSP's DHI measurement under the influence of the Linke turbidity

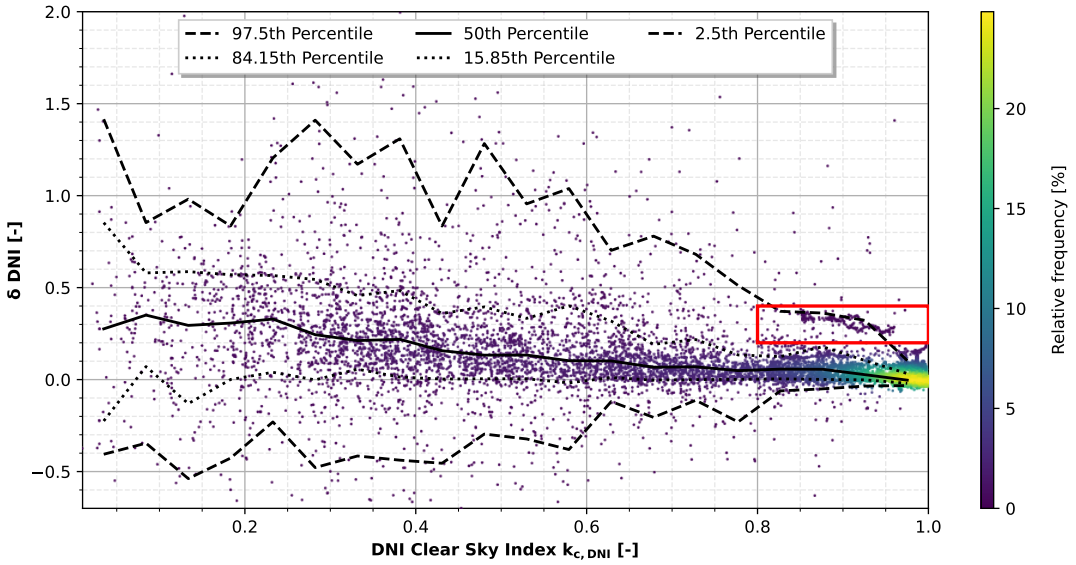

Figure B.15: Anomalies in MS-90's DNI measurement under the influence of the DNI clear sky index

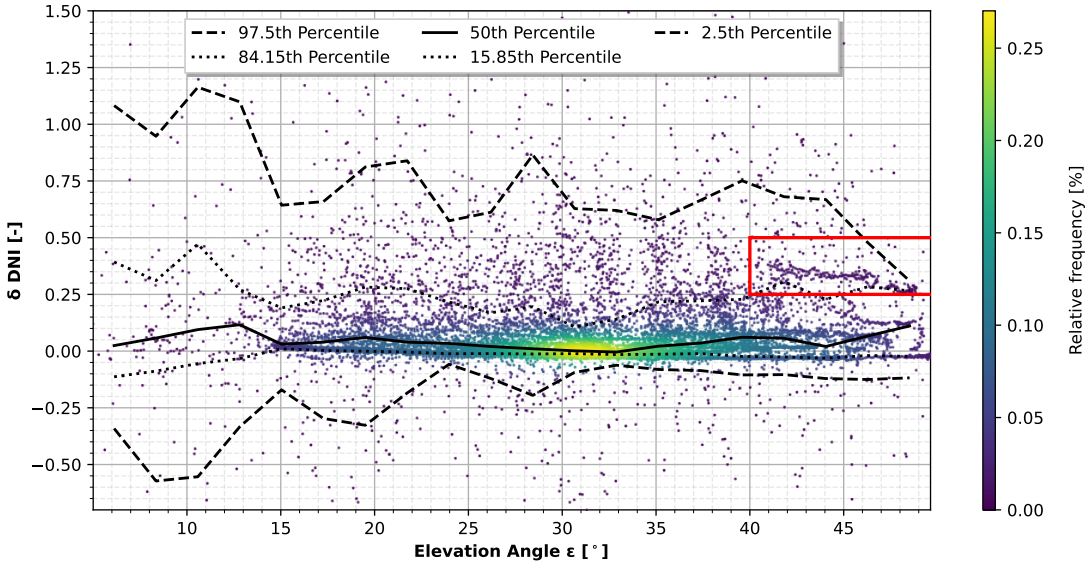

Figure B.16: Anomalies in MS-90's DNI measurement under the influence of the elevation angle

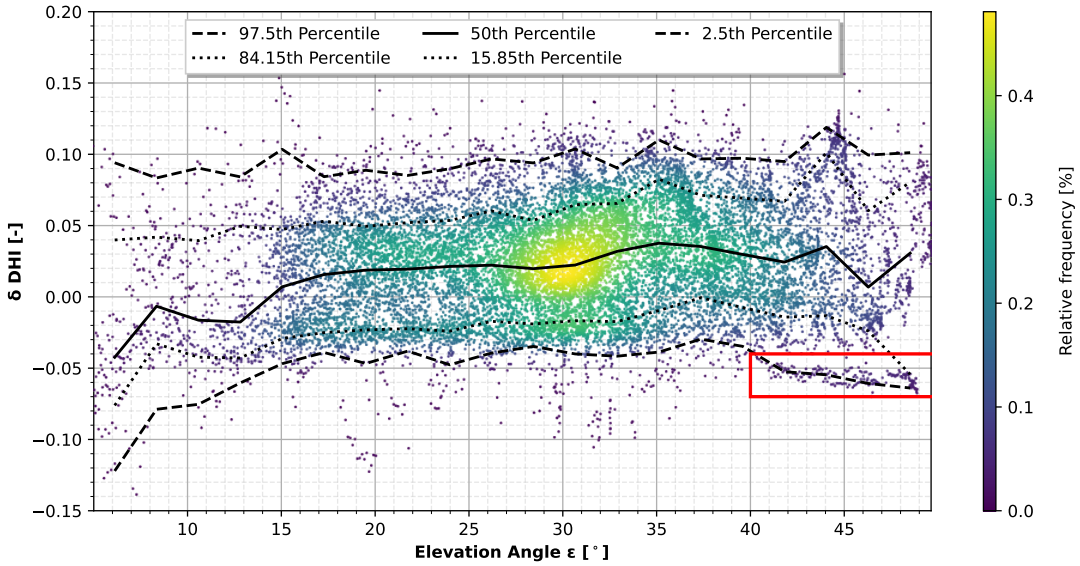

Figure B.17: Anomalies in PyranoCam's DHI measurement under the influence of the elevation angle

Investigation of Main and Secondary Influences

The following figures are all supporting material for the correlation analysis in Chapter 5. For the sensors not discussed in the body text, δDNI and δDHI are plotted above their main influence before and after adjusting the dataset. When existent, the secondary influences are also shown. In addition, it was pointed out in Section 5.2.1 that there may be two peculiarities in the determination of the regression model:

1. A value range is visually determined so that only data points within this interval are considered to build the model.
2. Should the cubic function not be able to correctly capture all data points, this is expressed in the verification polynomial whose parameters do not converge to zero or whose course in the scatter diagram still shows a dependence of the measurement deviation on the influencing factor. In such a case, a second iteration is performed.

Fig B.18 shows the elevation angle ϵ as the main influence of RSP's DNI measurement on the original data set, followed by Fig B.19 on the adjusted data set. Since only values $>$ -0.05, and $<$ 0.05 are considered for a better regression fit, the polynomial parameters do not completely converge to 0. Furthermore, the secondary influence α si visualized in Fig B.20 on the data set corrected for the main influence.

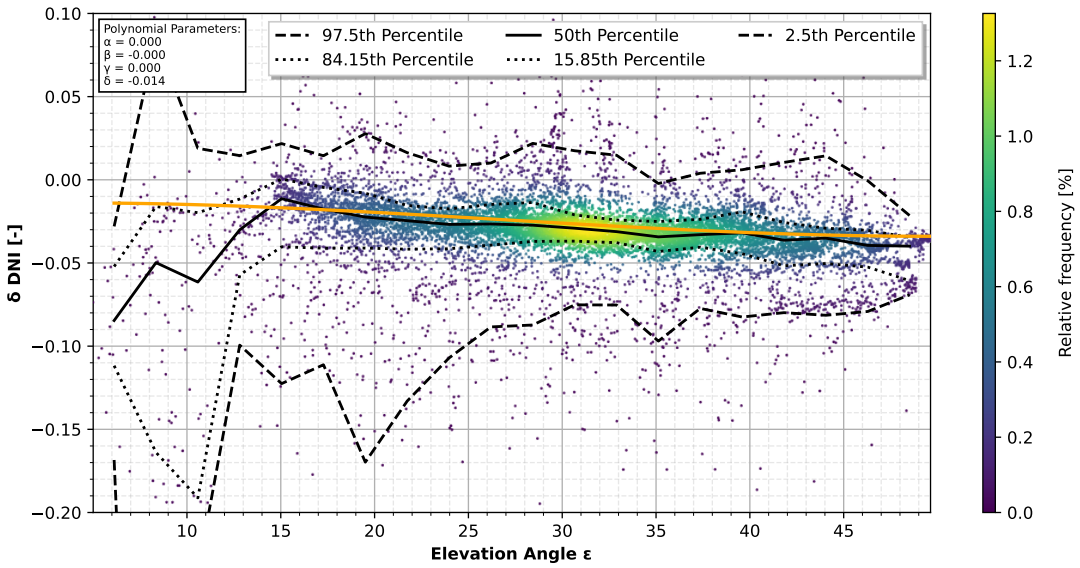

Figure B.18: Plot of the DNI measurement of the RSP over the main influence of the elevation angle on the original, unadjusted data set. The regression corresponds to a polynomial of degree 3.

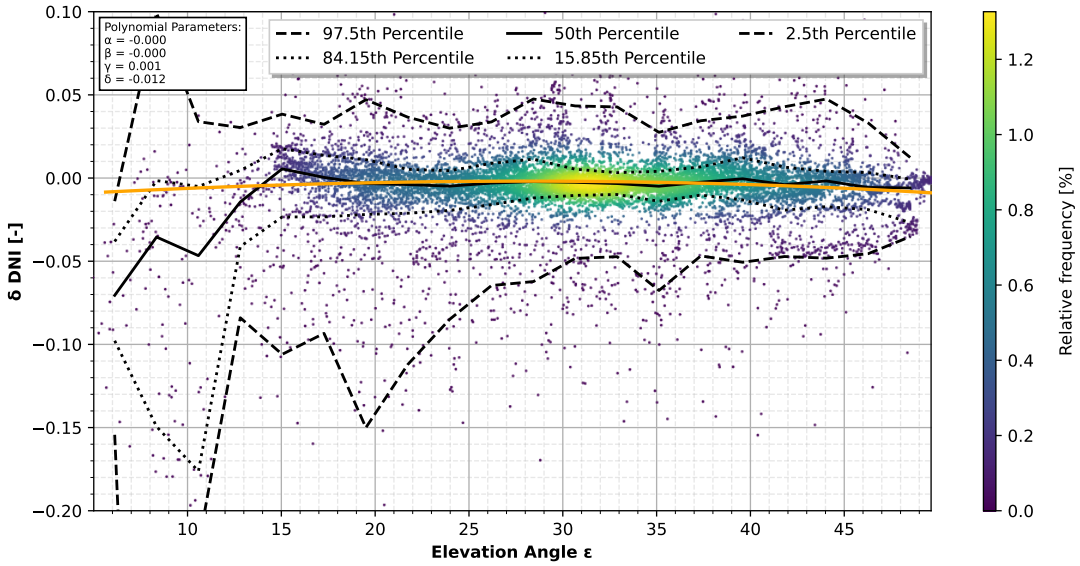

Figure B.19: Plot of the DNI measurement of the RSP over the main influence of the elevation angle on the data set corrected for the main influence. Since only values $>$-0.05, and $<$0.05 are considered for a better regression fit, the polynomial parameters do not completely converge to 0.

The same applies to Fig B.21 and Fig B.22, which illustrate RSP's δDHI over the main influence ϵ on the original and adjusted data set. Here, the regression was applied in the whole value range, and, hence, the polynomial parameters in Fig B.22 completely converge to 0.

SPN1's main influence for the DNI measurement is CSI, as is shown in Fig B.23 on the original data set. Since only values $>$-0.1, and $<$0.3 are considered for a better regression fit, for a better fit, the polynomial parameters do not completely converge to 0 in Fig B.24. Besides that, a polynomial of the third degree is not able to take all data points into account for a perfect fit. For this reason, a second iteration is performed, with the result given in Fig B.25. For DHI SPN1's main influence is the DNI clear sky index. The respective plots are given in Fig. B.26 and B.27.

Equivalent to the SPN1, the MS-90's main influence (CSI) cannot be removed from the data set within one iteration. Hence, a second one is required. The whole procedure is visualized in Fig B.28, B.29 and B.30.

For the DHI measurement of the MS-90, the main influence (CSI, given in Fig B.31 on the original data set) could be removed from the data set in the first iteration. Fig B.32 shows therefore the δDHI over the circumsolar radiation on the adjusted data set. All other detected secondary influences are plotted in Figures B.33 (elevation angle), B.34 (ambient temperature), B.35 (effective wavelength), and B.36 (DNI clear sky index).

PyranoCam shows the strongest dependence on the DNI clear sky index. The plot δDHI over $k_{c,\,DNI}$ can hence be seen in Fig B.37 on the original data set and in Fig B.38 on the adjusted data set.

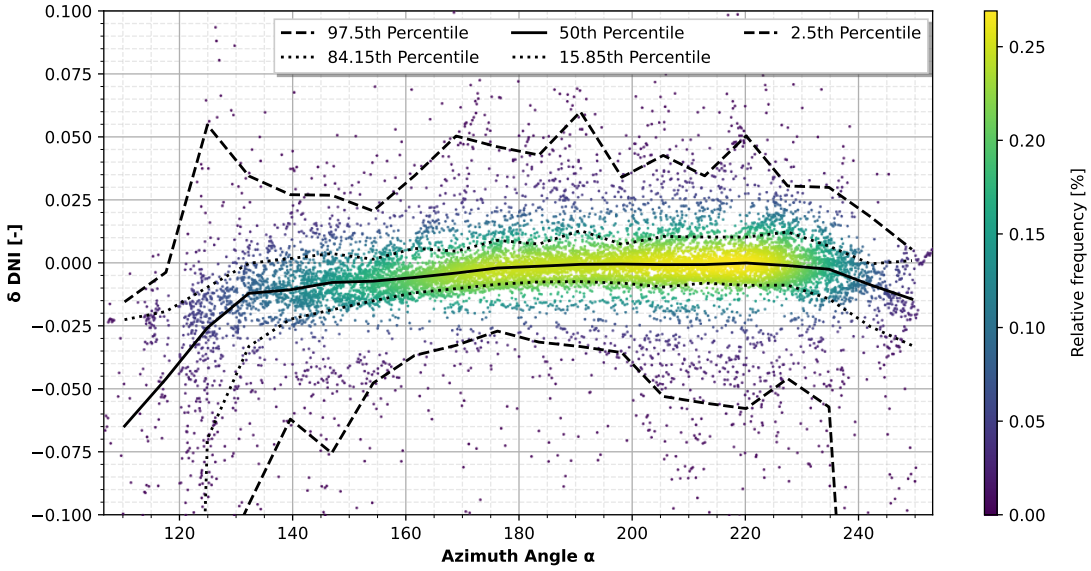

Figure B.20: Plot of the DNI measurement of the RSP over the secondary influence of the azimuth angle on the data set corrected for the main influence.

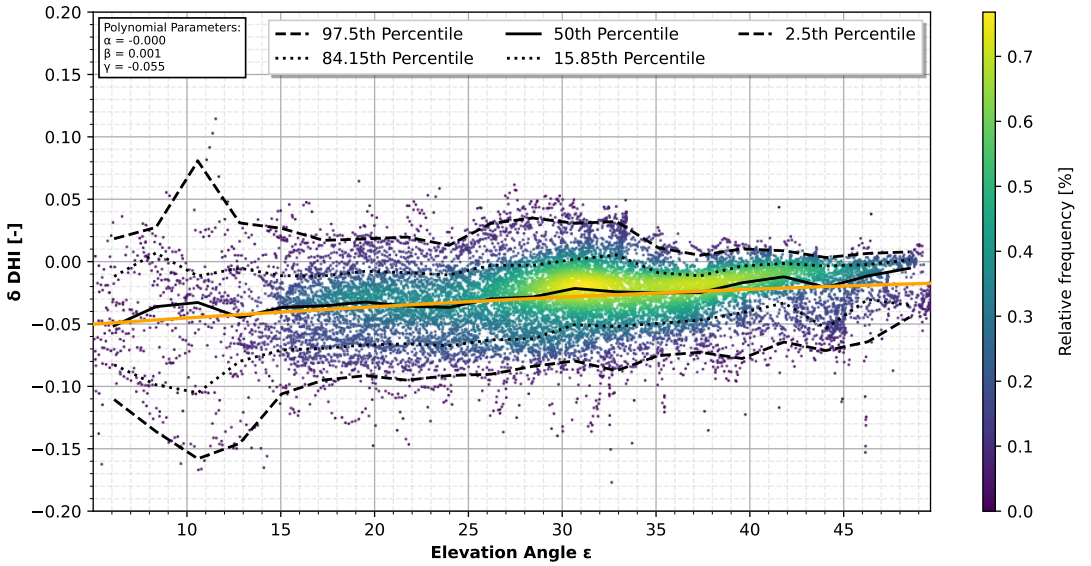

Figure B.21: Plot of the DHI measurement of the RSP over the main influence of the elevation angle on the original, unadjusted data set. The regression corresponds to a polynomial of degree 3.

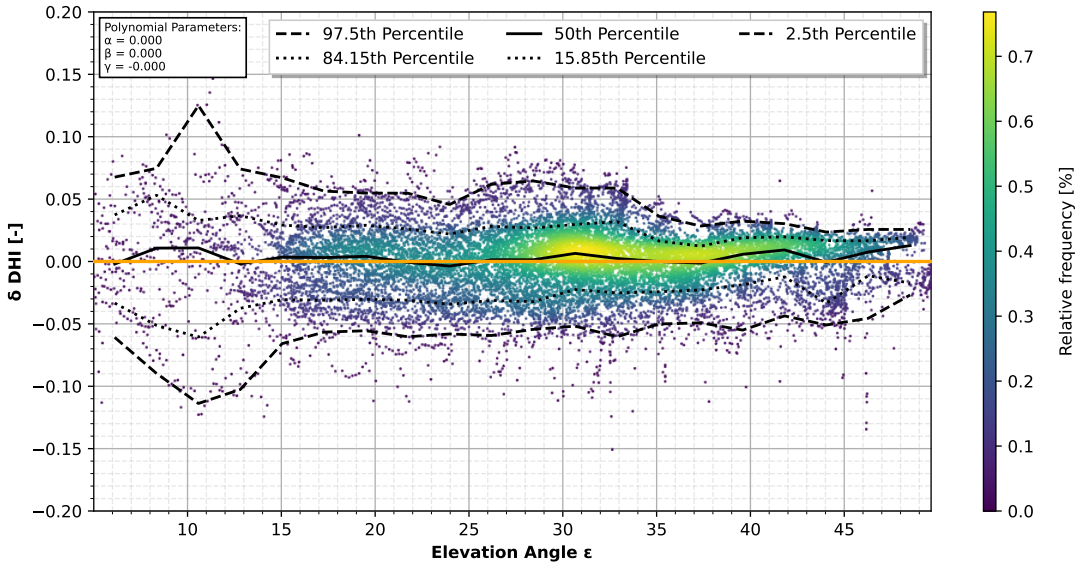

Figure B.22: Plot of the DHI measurement of the RSP over the main influence of the elevation angle on the data set corrected for the main influence. Since the regression was applied in the whole value range, the polynomial parameters completely converge to 0.

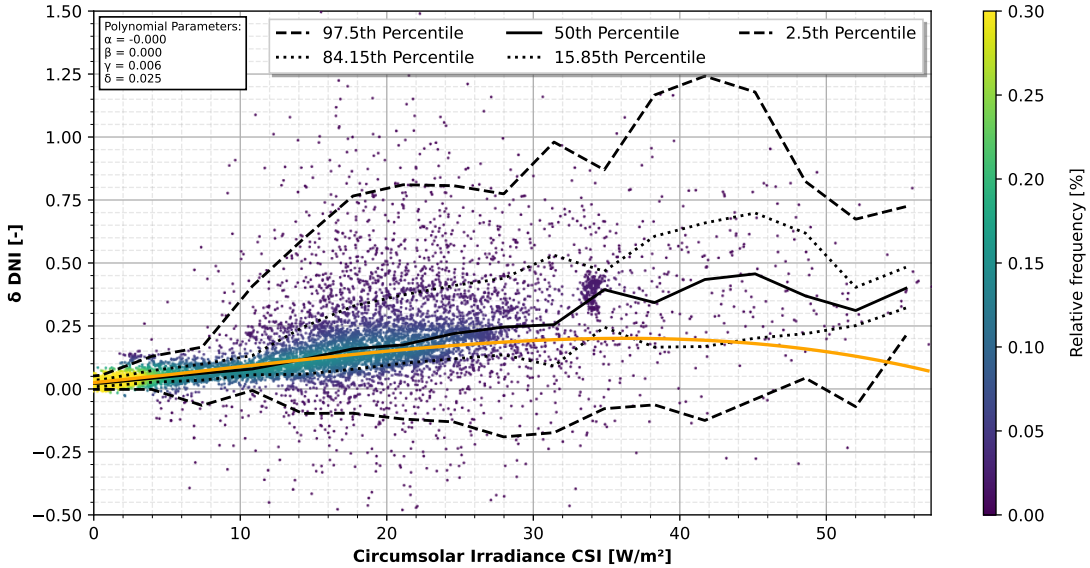

Figure B.23: Plot of the DNI measurement of the SPN1 over the main influence of the circumsolar irradiance on the original, unadjusted data set. The regression corresponds to a polynomial of degree 3.

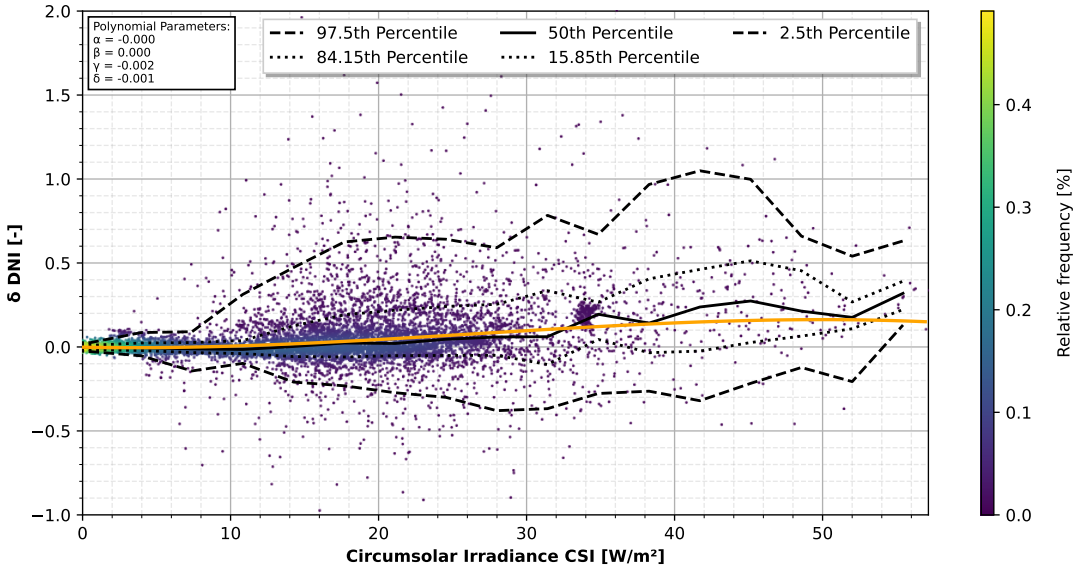

Figure B.24: Plot of the DNI measurement of the SPN1 over the main influence of the circumsolar irradiance on the data set corrected for the main influence in the first iteration. Since only values $>$-0.1, and <0.3 are considered for a better regression fit, the polynomial parameters do not completely converge to 0. Besides that, a polynomial of the third degree is not able to take all data points into account for a perfect fit.

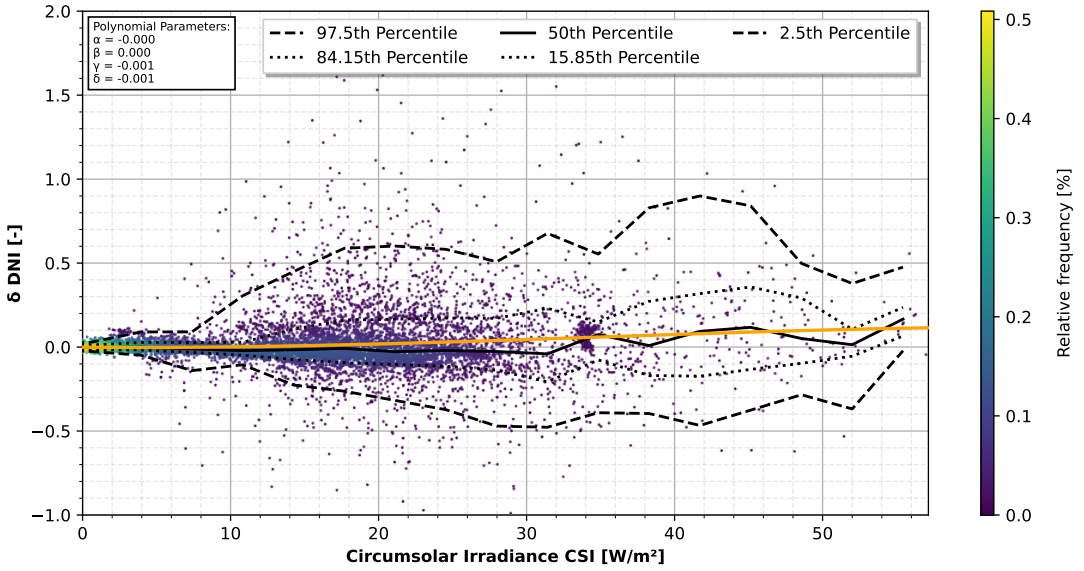

Figure B.25: Plot of the DNI measurement of the SPN1 over the main influence of the circumsolar irradiance on the data set corrected for the main influence in the second iteration. Since only values $>$-0.1, and <0.3 are considered for a better regression fit, the polynomial parameters do not completely converge to 0. After a second iteration, the main influence can be completely eliminated from the data set.

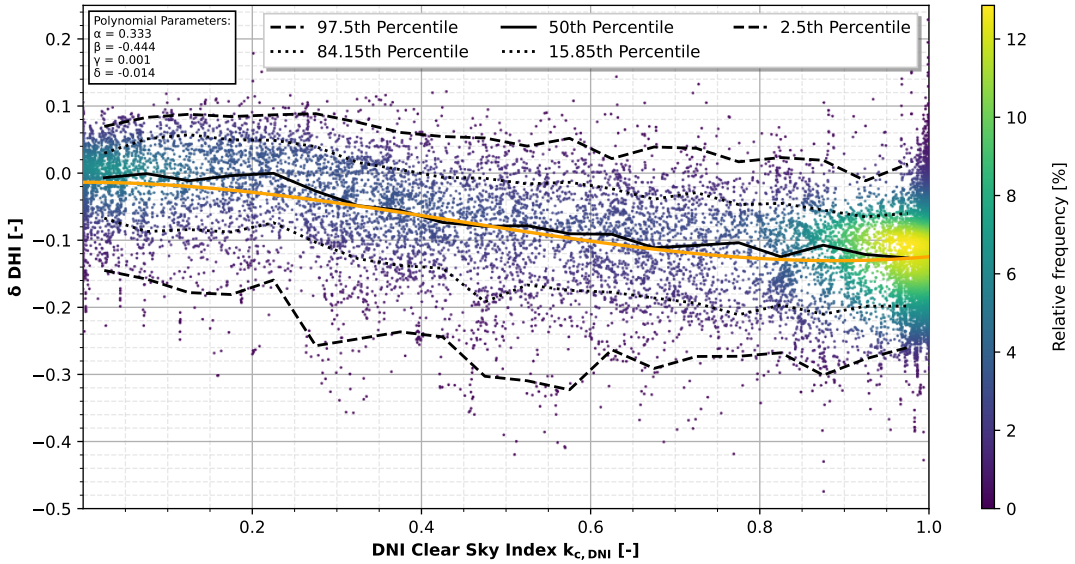

Figure B.26: Plot of the DNI measurement of the SPN1 over the main influence of the DNI clear sky index on the original, unadjusted data set. The regression corresponds to a polynomial of degree 3.

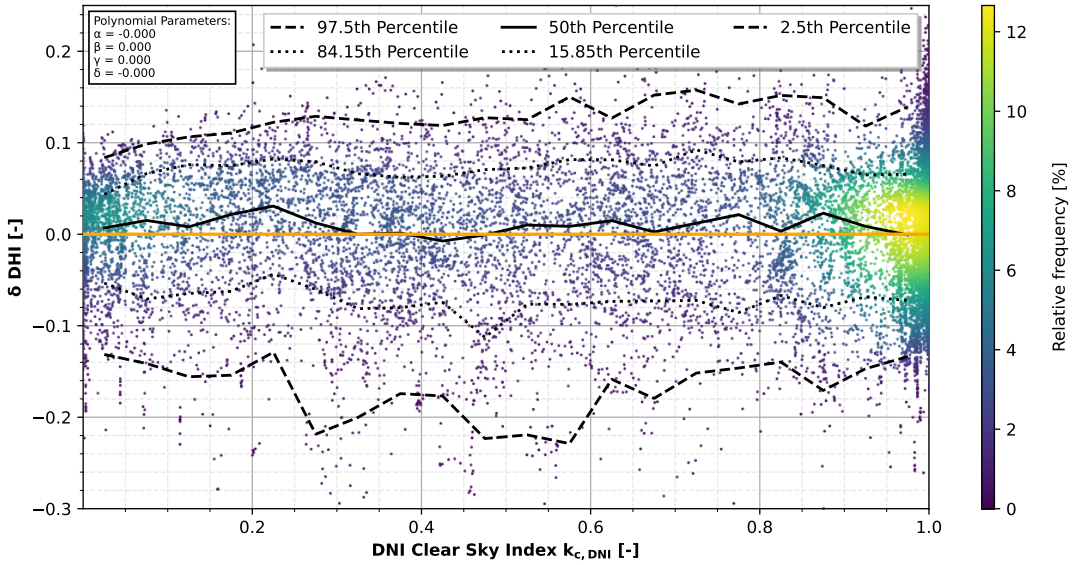

Figure B.27: Plot of the DHI measurement of the SPN1 over the main influence of the DNI clear sky index on the data set corrected for the main influence. Since the regression was applied in the whole value range, the polynomial parameters completely converge to 0.

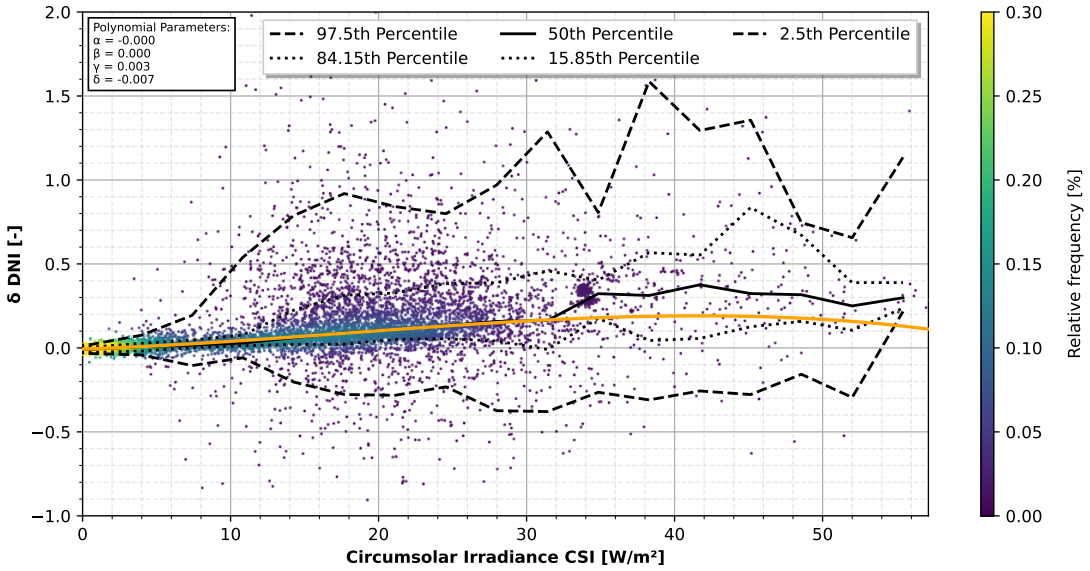

Figure B.28: Plot of the DNI measurement of the MS-90 over the main influence of the circumsolar irradiance on the original, unadjusted data set. The regression corresponds to a polynomial of degree 3.

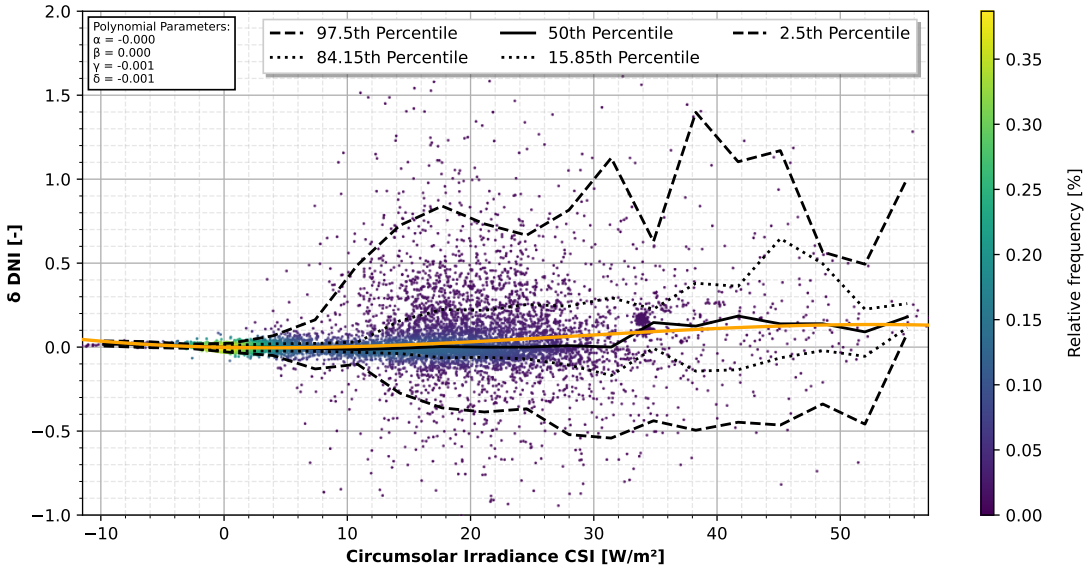

Figure B.29: Plot of the DNI measurement of the MS-90 over the main influence of the circumsolar irradiance on the data set corrected for the main influence in the first iteration. Since only values $>$-0.1, and <0.3 are considered for a better regression fit, for a better fit, the polynomial parameters do not completely converge to 0. Besides that, a polynomial of the third degree is not able to take all data points into account for a perfect fit.

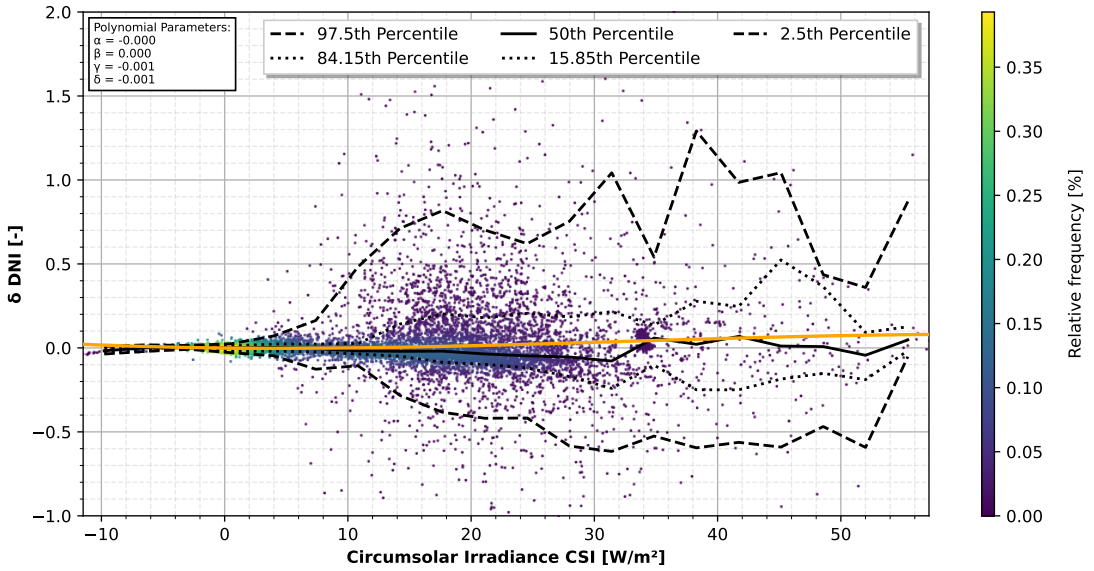

Figure B.30: Plot of the DNI measurement of the MS-90 over the main influence of the circumsolar irradiance on the data set corrected for the main influence in the second iteration. Since only values $>$-0.1, and $<$0.3 are considered for a better regression fit, for a better fit, the polynomial parameters do not completely converge to 0. After a second iteration, the main influence can be completely eliminated from the data set.

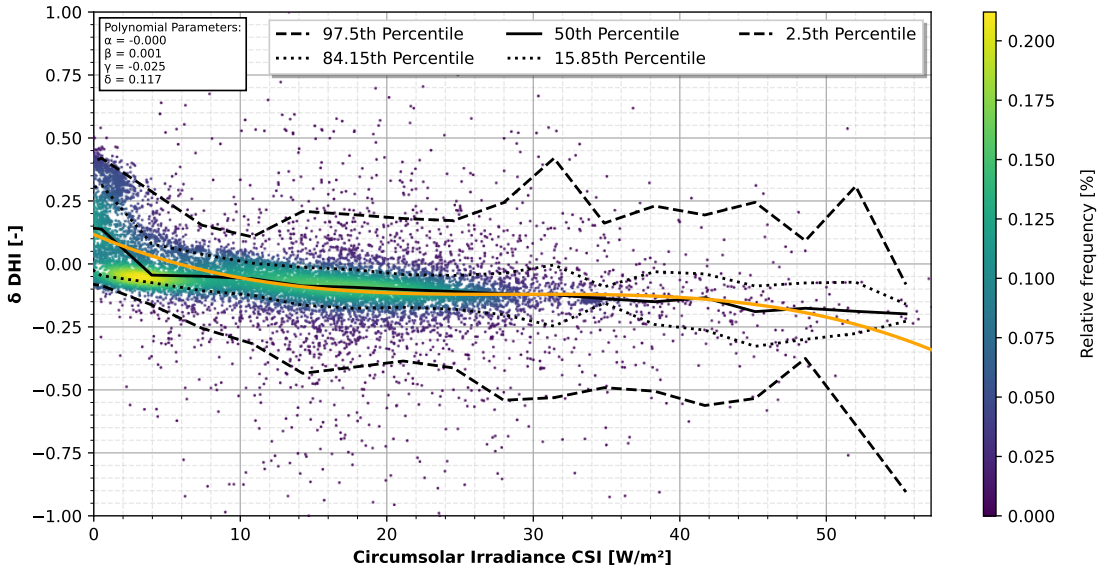

Figure B.31: Plot of the DHI measurement of the MS-90 over the main influence of the circumsolar irradiance on the original, unadjusted data set. The regression corresponds to a polynomial of degree 3.

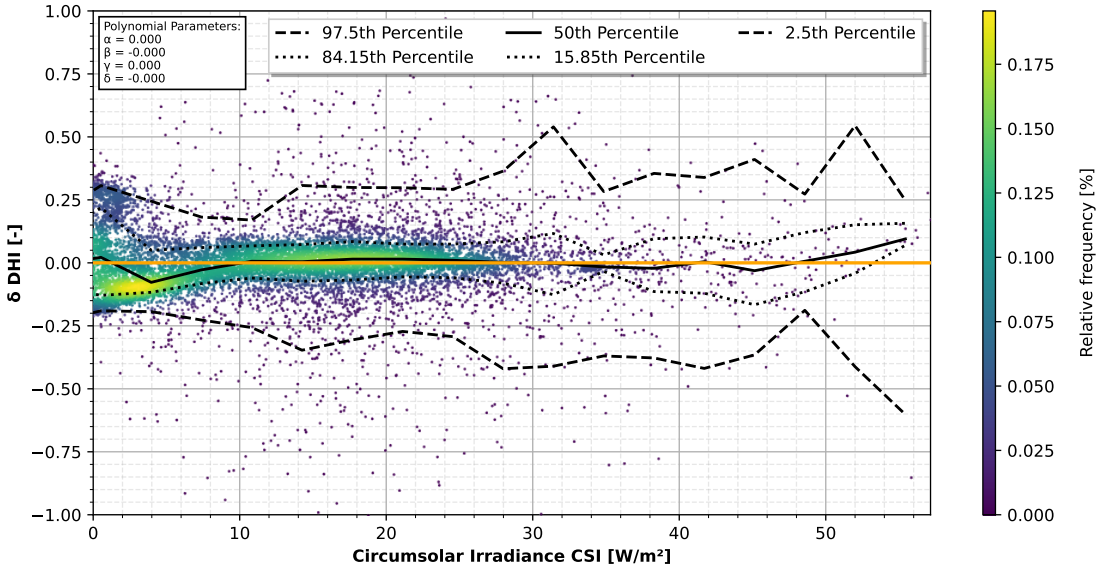

Figure B.32: Plot of the DNI measurement of the MS-90 over the main influence of the circumsolar irradiance on the data set corrected for the main influence. Since the regression was applied in the whole value range, the polynomial parameters completely converge to 0.

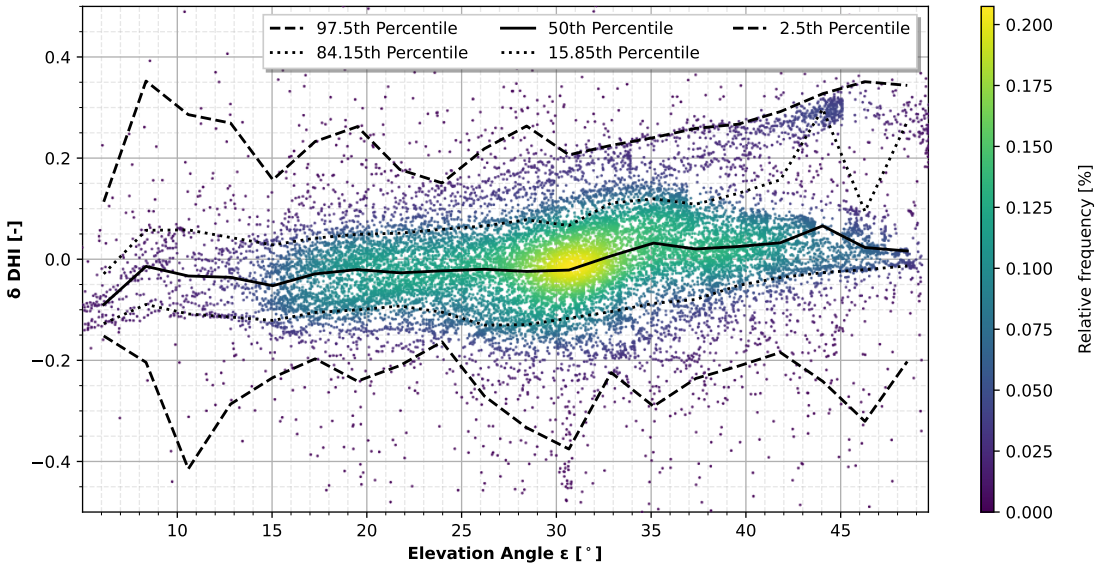

Figure B.33: Plot of the DHI measurement of the MS-90 over the secondary influence of the elevation angle on the data set corrected for the main influence.

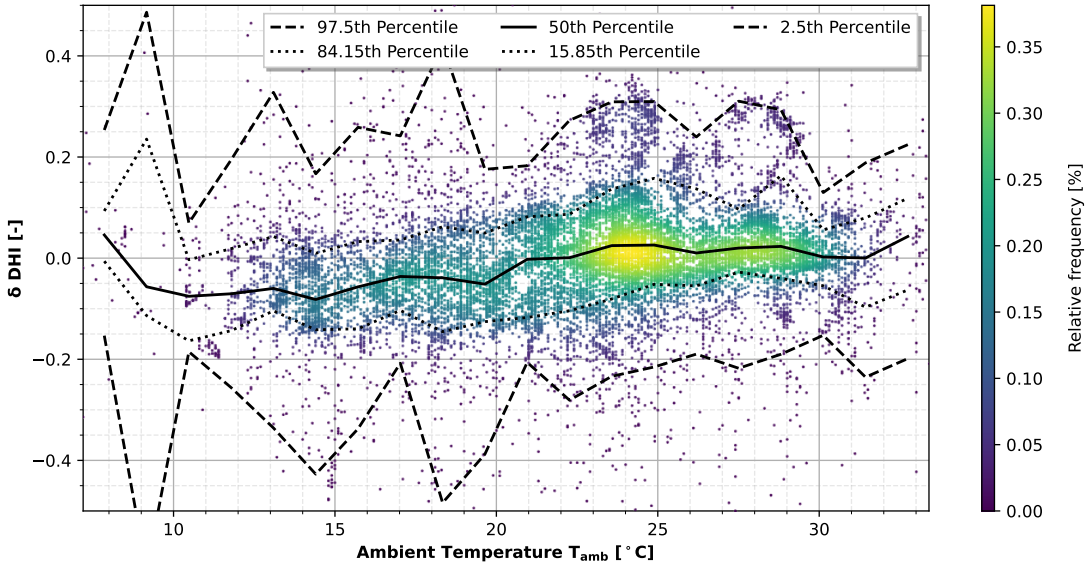

Figure B.34: Plot of the DHI measurement of the MS-90 over the secondary influence of the ambient temperature on the data set corrected for the main influence.

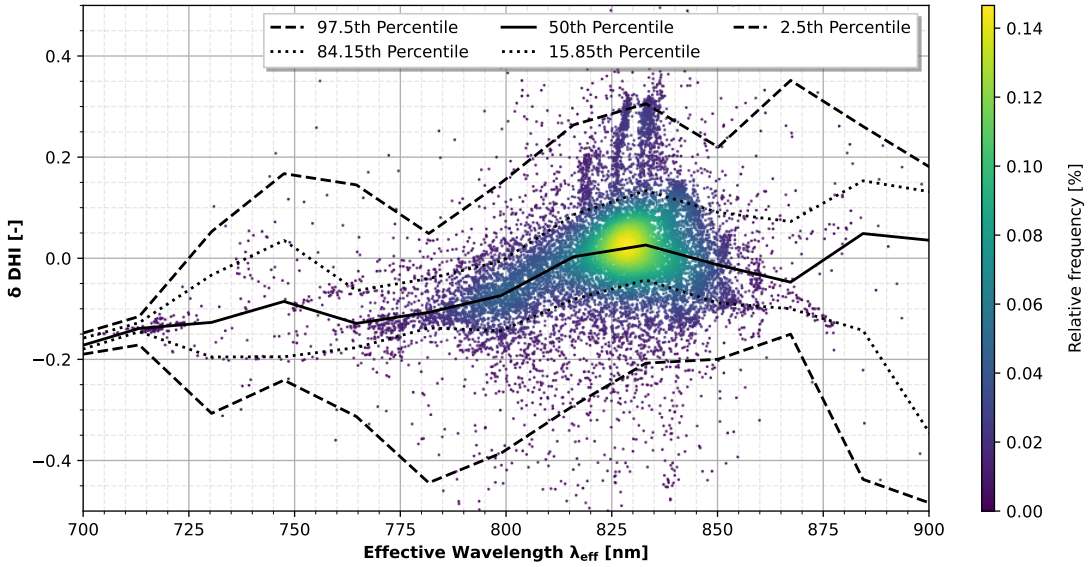

Figure B.35: Plot of the DHI measurement of the MS-90 over the secondary influence of the effective wavelength on the data set corrected for the main influence.

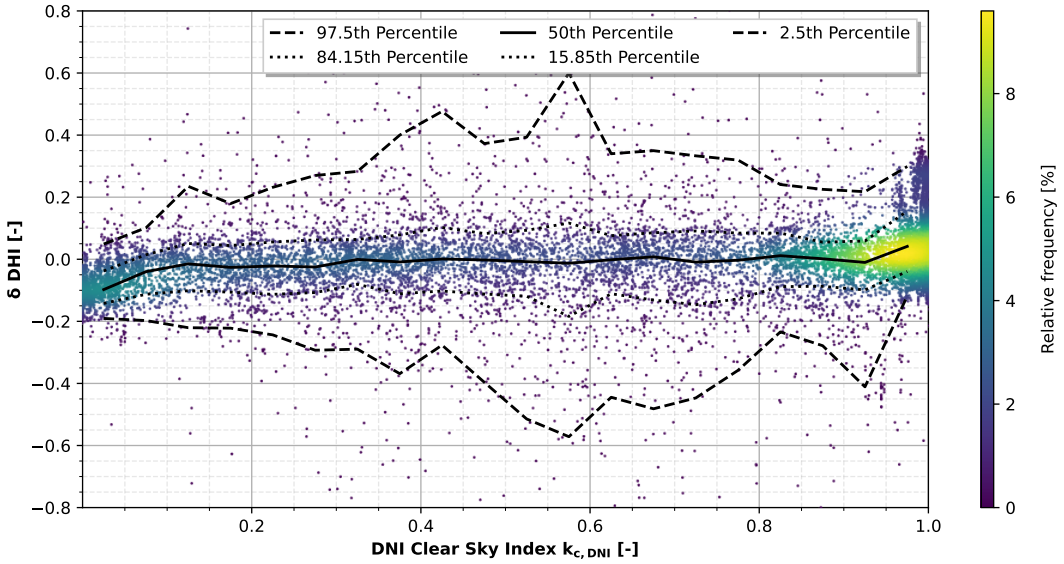

Figure B.36: Plot of the DHI measurement of the MS-90 over the secondary influence of the DNI clear sky index on the data set corrected for the main influence.

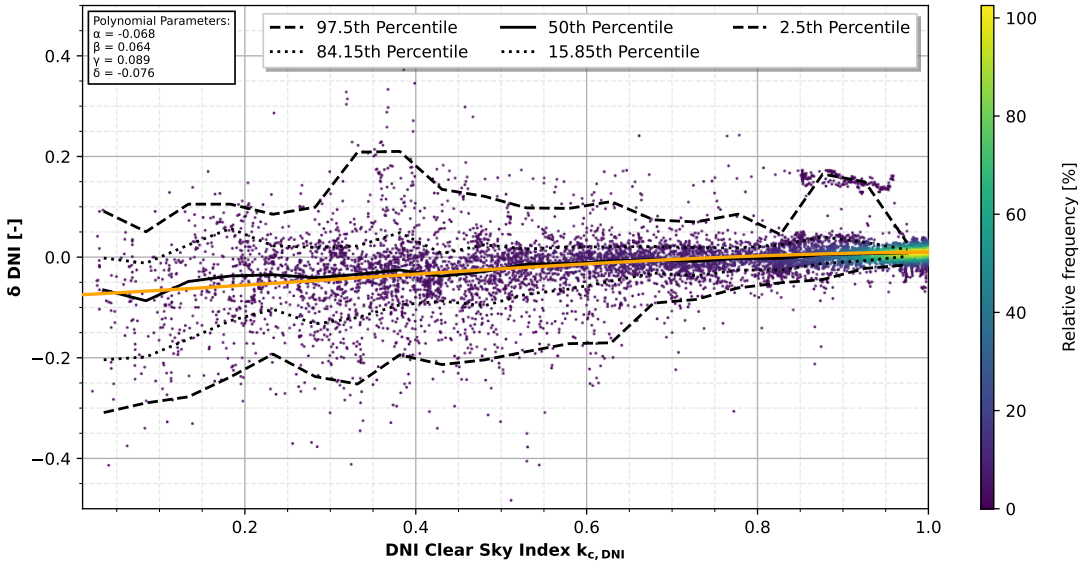

Figure B.37: Plot of the DNI measurement of the PyranoCam over the main influence of the DNI clear sky index on the original, unadjusted data set. The regression corresponds to a polynomial of degree 3.

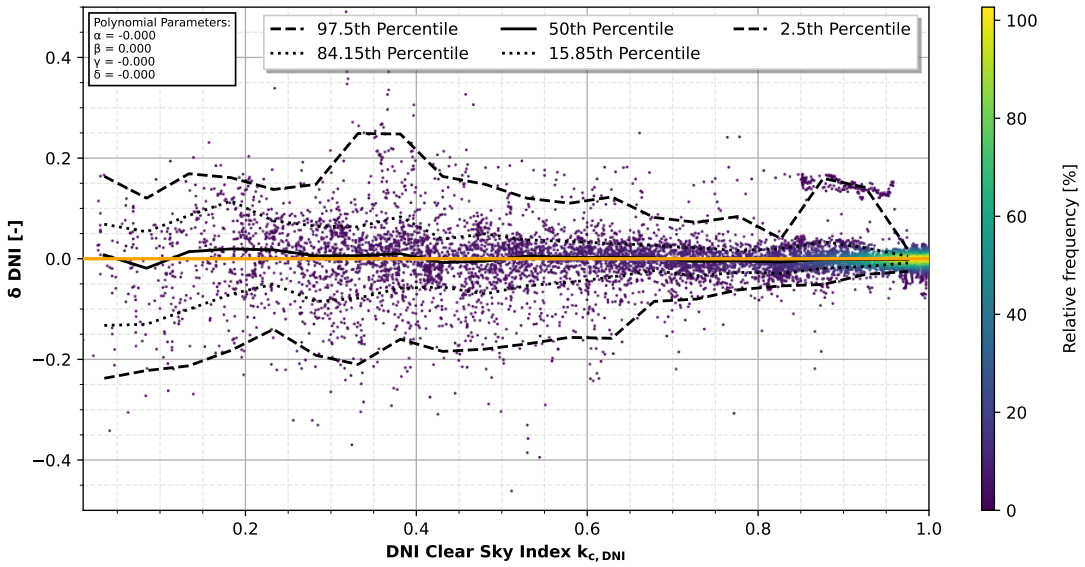

Figure B.38: Plot of the DNI measurement of the PyranoCam over the main influence of the DNI clear sky index on the data set corrected for the main influence. Since the regression was applied in the whole value range, the polynomial parameters completely converge to 0.

Double-Check Measurement Set Up Leveling

(a) Checking the leveling of the LI-COR 200R with the bubble level in position 0°

(b) Checking the leveling of the LI-COR 200R with the bubble level in position 180°

Figure B.39: Checking the leveling of the LI-COR 200R with the bubble level in position 0° and 180°, in order to make up for any potential ground plate imperfections [68]. The photographs were taken on 13/01/2023 by Sergio Gonzalez Rodriguez

To check for a dependence of the RSP on the azimuth angle, the leveling of the LI-COR200R was double-checked after the end of the measurement period. The bubble level is shown in Fig B.39 for a position of 0° and 180°, in order to make up for any potential ground plate imperfections [68].

C Additional Tables

C.1 Tables for Chapter 2

Table C.1 compares all sensors with regard to the requirements of ISO 9060 as well as the criteria uncertainty, spectral range, and price.

Table C.1: Comparison of all sensors with regard to the requirements of ISO 9060 and the spectral range

		ISO 9060						Used radiometers						
		Secondary Standard		First Class		Second Class		Reference					PyranoCam	
Criteria	**Unit**	**Pyranometer**	**Pyrheliometer**	**Pyranometer**	**Pyrheliometer**	**Pyranometer**	**Pyrheliometer**	**CMP21**	**CHP1**	**SPN1**	**MS90**	**LI-COR 200R**	**CMP21**	**ASI Camera**
Response Time 95%	s	< 10	< 10	< 20	< 15	< 30	< 20	< 5	< 5	0.1	n.a.	< 0.001	< 5	-
Zero Offset a)	W/m²	± 7	± 1	± 15	± 3	± 30	± 6	± 7	n.a.	< 3	n.a.	0	± 7	-
Zero Offset b)	W/m²	± 2	± 1	± 4	± 4	± 8	± 7	± 2	< 1	< 3	n.a.	0	± 2	-
Zero Offset c)	W/m²	± 10	-	± 21	-	± 41	-	± 9	-	0.6	n.a.	0	± 9	-
Non-Stability	%	± 0.8	± 0.5	± 1.5	± 1	± 3	± 2	< 0.5	< 0.5	< 1	n.a.	< 2	< 0.5	-
Non-Linearity	%	± 0.5	± 0.2	± 1	± 0.5	± 3	± 2	< 0.2	< 0.2	< 1	± 2.5	1	< 0.2 %	-
Directional Response	W/m²	± 10	-	± 20	-	± 30	-	< 10	-	± 20	n.a.	n.a.	< 10	-
Spectral Error	%	± 0.5	± 0.2	± 1	± 1	± 5	± 2	< 0.1	n.a.	± 10	n.a.	Note[a]	< 0.1	Note[b]
Temperature Response	%	± 1	± 0.5	± 2	± 1	± 4	± 5	< 3	< 0.5	± 1	n.a.	± 0.15	< 3	Note[c]
Tilt Response	%	± 0.5	± 0.2	± 2	± 0.5	± 5	± 2	< 0.2	n.a.	<2	± 5	0	< 0.2	-
Spectral Range	nm							270 - 3000	200 - 4000	400 - 2700	300 - 2500	400 - 1100	270 - 3000	390 - 700

[a]The spectral response, as described in Chapter A.2.5, defines the sensor's sensitivity to light of various wavelengths. Silicon sensors do not react to all incoming wavelengths equally, unlike thermopile pyranometers. As a result, their spectral response is not flat and therefore leads to a high spectral error, whose magnitude is a multiple of the error defined in ISO.

[b]There is no completed evaluation of this new measurement method yet. However, since DHI's estimation is linked to the output signal's intensity of the RGB color channels, the existence of a spectral error is possible.

[c]An increase in temperature causes an increase in noise in cameras. Whether this has an effect on the measurement is currently unknown.

List of Figures

List of Tables

List of Equations

Nomenclature

Greek Symbols

Symbol	Meaning	Unit
α	Azimuth angle	°
δ	Relative deviation	%
ΔT	Temperature difference	°C
ϵ	Elevation angle	°
ζ	Zenith angle	°
ϑ_{amb}	Ambient temperature	°C
λ	Wavelength	nm
λ_{eff}	Effective wavelength	nm
$\lambda_{\mathrm{eff,\ t_i}}$	Effective wavelength at an time increment	nm
μ	Expected value	W/m²
ρ	Spearman's rank correlation coefficient	-
σ	Standard deviation	W/m²

Lowercase Latin Symbols

Symbol	Meaning	Unit
a	Lower wavelength limit	nm
b	Upper wavelength limit	nm
c	Speed of light	m/s
f	Frequency	Hz
h	Planck's constant	Js
i	Increment	-
j	Time period of 15s	s
k	Multiplication factor for uncertainty	-
kc_{DNI}	DNI clear sky index	-
m_i	Main influence	$(d.o.p)$
n	Sample size	-
n_{out}	Set of values outside of an imaginary Gaussian bell curve	-
n.a.	not available	
p	Polynomial value (when calculating squared error)	%
$p_{97.5}$	97.5^{th} percentile	-
$p_{2.5}$	2.5^{th} percentile	-
$r_{x,\,i}$	Rank of the x-variable for determining the correlation coefficient	$(d.o.p)$
$r_{y,\,i}$	Rank of the y-variable for determining the correlation coefficient	$(d.o.p)$
rMAD	Relative Mean-Averaged-Deviation	%
rRMSD	Relative Root-Mean-Squared-Deviation	%
s	standard deviation of a sample size	W/m^2
u	standard uncertainty	W/m^2
x_i	Arithmetic mean of an input quantity $\overline{X}_i$	W/m^2
y	Deviation of the measurement (when calculating squared error)	%
y_i	Measured sensor value	W/m^2
y_{ref}	Measured reference value	W/m^2

Uppercase Latin Symbols

Symbol	Meaning	Unit
AM	Air mass	-
$C0_2$	Carbon dioxide	-
CI	Confidence interval	-
CSI	Circumsolar irradiance	W/m^2
DHI	Diffuse horizontal irradiance	W/m^2
DNI	Direct normal irradiance	W/m^2
$DNI_{hor.}$	Direct normal irradiance measured on a horizontal plane	W/m^2
DNI_j	Maximum direct normal irradiance measured within one revolution	W/m^2
DNI_{meas}	Measured direct normal irradiance	W/m^2
DNI_{theo}	Theoretically possible direct normal irradiance	W/m^2
E	Squared Error	W/m^2
E_{em}	Electromagnetic energy	J
E_G	Total radiation power	W/m^2
GHI	Global horizontal irradiance	W/m^2
H_20	Water	-
I_{e^-}	Short-Circuit Current	A
MAD	Mean-Averaged-Deviation	W/m^2
N_2	Nitrogen	-
O_2	Oxygen	-
O_3	Ozone	-
T_L	Linke turbidity	-
PI_{95}	Prediction interval 95%	-
RMSD	Root-Mean-Squared-Deviation	W/m^2
U	Expanded uncertainty	W/m^2

U	Electric voltage	V
U_j	Electric voltage measured within one revolution	V
U_{max}	Maximum electrical voltage	V
U_{min}	Minimum electrical voltage	V
U_{th}	Thermoelectric voltage	V
$\overline{X}_i$	Input quantity	W/m^2

Acronyms

Symbol	Meaning
Addr. Unk.	Address Unknown
ASI	All-Sky-Imager
cf.	confer
CIEMAT	Centro de Investigaciones Energéticas, Medioambientales y Tecnológicas
CNN	Convolutional Neural Network
CSP	Concentrating Solar Power
CSPS	CSP Services GmbH
DLR	Deutsches Zentrum für Luft- und Raumfahrt e.V.
d.o.p.	depending on parameter
FOV	Field of View
GCOS	Global Climate Observing System
HVU	Heat and Ventilation Unit
IPR	Interpercentile Range
ISO	International Organization for Standardization
JCGM	Joint Committee for Guides in Metrology
Ltd.	Limited Company
NaN	Not a Number
NREL	National Renewable Energy Laboratory
PSA	Plataforma Solar de Almería
PV	Photovoltaics
RGB	Red, Green, Blue (Color Space)
RSP	Rotating Shadowband Pyranometer
SSPS	Small Solar Power System
Temp.	Temperature

UV	Ultraviolet
WMO	World Meteorological Organization
Yr. Unk.	Year Unknown

Bibliography

[1] María Isabel Roldán Serrano; "Concentrating Solar Thermal Technologies"; Springer International Publishing, Tabernas (Spain) [2017]; DOI: http://dx.doi.org/10.1007/978-3-319-45883-0

[2] R. Guerrero-Lemus et al.; "Bifacial solar photovoltaics – A technology review"; Renewable and Sustainable Energy Reviews, La Laguna (Tenerife, Spain) [2016]; DOI: http://dx.doi.org/10.1016/j.rser.2016.03.041

[3] Volker Quaschning; "Regenerative Energiesysteme: Technologie - Berechnung - Klimaschutz"; Carl Hanser Verlag, Munich (Germany); 11^{th} edition [2022]; ISBN: 978-3-446-47163-4

[4] Aron Habte et al.; "Intercomparison of 51 radiometers for determining global horizontal irradiance and direct normal irradiance measurements"; Solar Energy, Golden (USA) [2016]; DOI: http://dx.doi.org/10.1016/j.solener.2016.03.065

[5] Marion Schroedter-Homscheidt et al.; "Classifying ground-measured 1 minute temporal variability within hourly intervals for direct normal irradiances"; Gebrüder Borntraeger Science Publishers, Stuttgart (Germany) [2018]; DOI: http://dx.doi.org/10.1127/metz/2018/0875

[6] Laurent Vuilleumier et al.; "Performance Evaluation of Radiation Sensors for the Solar Energy Sector"; Energy Meteorology, Payerne (Switzerland) [2017]; DOI: http://dx.doi.org/10.1127/metz/2017/0836

[7] Niklas Benedikt Blum et al.; "Measurement of diffuse and plane of array irradiance by a combination of a pyranometer and an all-sky imager"; Solar Energy, Almería (Spain) [2021]; DOI: https://doi.org/10.1016/j.solener.2021.11.064

[8] Norbert Geuder and Volker Quaschning; "Soiling of irradiation sensors and methods for soiling correction"; Solar Energy, Almería (Spain) [2006]; DOI: http://dx.doi.org/10.1016/j.solener.2006.06.001

[9] Frank Vignola; Joseph Michalsky and Thomas Stoffel; "Solar and Infrared Radiation Measurements"; Taylor & Francis Group LLC, Boca Raton (USA); 2^{nd} edition [2020]; ISBN: 978-1-138-09629-5

[10] National Renewable Energy Laboratory (NREL); "Solar Spectra"; NREL; [Online] source is available at: https://www.nrel.gov/grid/solar-resource/spectra.html, Accessed on: 09.12.2022.

[11] Deutsches Zentrum für Luft-und Raumfahrt e.V. (DLR); "Thema Licht"; DLR; [Online] source is available at: https://www.dlr.de/schoollab/desktopdefault.aspx/tabid-17395/, Accessed on: 09.12.2022.

[12] Konrad Mertens; "Photovoltaik - Lehrbuch zu Grundlagen, Technologie und Praxis"; Carl Hanser Verlag, München (Germany); 5^{th} edition [2020]; ISBN: 978-3-446-46404-9

[13] Manajit Sengupta et al.; "Best Practices Handbook for the Collection and Use of Solar Resource Data for Solar Energy Applications"; IEA PVPS Task 16, Paris (France); 3^{rd} edition [2021]; ISBN: 978-3-907281-19-2

[14] J. Badosa et al.; "Solar irradiances measured using SPN1 radiometers: uncertainties and clues for development"; Atmospheric Measurement Techniques (AMT), Palaiseau (France) [2014]; DOI: http://dx.doi.org/10.5194/amtd-7-8149-2014

[15] International Organization for Standardization (ISO); "ISO 9060 - Solar energy — Specification and classification of instruments for measuring hemispherical solar and direct solar radiation"; ISO, Geneva (Switzerland); 2^{nd} edition [2018]

[16] World Meteorological Organization (WMO); "Guide to Instruments and Methods of Observation: Volume I –Measurement of Meteorological Variables"; Chair, Publications Board, Geneva (Switzerland); WMO-No. 8 [2020]; ISBN: 978-92-63-10008-5

[17] Karl Wilhelm Franz Linke; "Transmissions-Koeffizient und Trübungsfaktor"; Pubr. Unk., Addr. Unk. [1922]; beitr. Phys. fr. Atmos. 10, 91–103

[18] Pierre Ineichen and Richard Perez; “A New Airmass Independent Formulation for the Linke Turbidity Coefficient”; Solar Energy, Geneva (Switzerland) [2002]; DOI: https://doi.org/10.1016/S0038-092X(02)00045-2

[19] Stefan Wilbert et al.; “Uncertainty of Rotating Shadowband Irradiometers and Si-Pyranometers Including the Spectral Irradiance Error”; SolarPACES, Almería: Spain [2016]; DOI: http://dx.doi.org/10.1063/1.4949241

[20] Martin Maly; “Spectral Selectivity vs. Spectral Error: Shedding Light on ISO 9060:2018”; OTT HYDROMET [2021]; [Online] source is available at: https://blog.otthydromet.com/en/spectral-selectivity-vs-spectral-error-shedding-light-on-iso-9060/?utm_source=direct_industry&utm_medium=microsite&utm_content=&utm_campaign=2022_ott_c-solared_, Accessed on: 11.12.2022.

[21] G. Nofuentes et al.; “Is the average photon energy a unique characteristic of the spectral distribution of global irradiance?”; Solar Energy, Jaén (Spain) [2017]; DOI: http://dx.doi.org/10.1016/j.solener.2017.03.086

[22] Christian A. Gueymad; “Daily spectral effects on concentrating PV solar cells as affected by realistic aerosol optical depth and other atmospheric conditions”; Solar Consulting Services, Colebrook (USA) [2009]; DOI: http://dx.doi.org/10.1117/12.826071

[23] Kipp & Zonen B.V.; “Instruction Manual SOLYS2 Sun Tracker”; Kipp & Zonen B.V., Delft (Netherlands) [2017]

[24] Kipp & Zonen B.V.; “Sun Trackers for Solar-Tracking and PC-Based Positioning Operations”; Kipp & Zonen B.V., Delft (Netherlands) [Yr. Unk.]

[25] Rudolf Busch; “Elektrotechnik und Elektronik - Für Maschinenbauer und Verfahrenstechniker”; Springer Vieweg, Wiesbaden (Germany); 7^{th} edition [2015]; DOI: http://dx.doi.org/10.1007/978-3-658-09675-5

[26] Albert Einstein; “Über einen die Erzeugung und Verwandlung des Lichtes betreffenden heuristischen Gesichtspunkt”; Verlag von Johann Ambrosius Barth, Leipzig (Germany) [1905]; DOI: https://doi.org/10.1002/andp.19053220607

[27] Riyad Mubarak; Holger Schilke and Gunther Seckmeyer; “Improving the Irradiance Data Measured by Silicon-Based Sensors”; energies, Hanover (Germany) [2021]; DOI: https://doi.org/10.3390/en14102766

[28] Delta-T Devices; SPN1 Sunshine Pyranometer; Delta-T Devices, Cambridge (England); 7^{th} edition [Yr. Unk.]

[29] LI-COR Biosciences; “Sensor Design”; LI-COR Biosciences [2022]; [Online] source is available at: https://www.licor.com/env/products/light/science, Accessed on: 13.11.2022.

[30] Kipp & Zonen B.V.; “Instruction Manual for CMP series Pyranometer and CMA series Albedometer”; Kipp & Zonen B.V., Delft (Netherlands) [2016]

[31] Kipp & Zonen; “CHP1 Pyrheliometer Instruction Manual”; Kipp & Zonen, Delft (Netherlands) [2008]

[32] John Wood; “SPN1 Measurement Best Practices”; Delta-T Devices Ltd., Burwell (England); 3^{rd} edition [Yr. Unk.]

[33] EKO Instruments Co. Ltd.; “Instruction Manual DNI Sensor”; EKO Instruments Co. Ltd., Tokyo (Japan) [2018]

[34] Mário Pó et al.; “Direct Normal Irradiance Measurements using a tracker-less Sunshine Duration Measurement Concept”; EKO Instruments Co. Ltd., Tokyo (Japan) [2018]; DOI: http://dx.doi.org/10.4229/35thEUPVSEC20182018-6DO.10.5

[35] Ekbert Hering and Gert Schönfelder; “Sensoren in Wissenschaft und Technik-Funktionsweise und Einsatzgebiete”; Vieweg & Teubner Verlag, Wiesbaden (Germany); 1^{st} edition [2012]; DOI: http://dx.doi.org/10.1007/978-3-8348-8635-4

[36] Dietrich Sonntag and Klaus Behrens; “Ermittlung der Sonnenscheindauer aus pyranometrisch gemessenen Bestrahlungsstärken der Global- und Himmelsstrahlung”; Selbstverlag des Deutschen Wetterdienstes, Offenbach am Main (Germany) [1992]; ISSN: 2194-5969

[37] EKO Instruments Co. Ltd.; “MS-90 DNI Sensor Technical Specifications”; EKO Instruments Co. Ltd., Tokyo (Japan) [2018]

[38] EKO Instruments Co. Ltd.; “MS-90 Plus+”; EKO Instruments Co. Ltd.; [Online] source is available at: https://www.eko-instruments.com/eu/categories/products/solar-monitoring-stations/ms-90-plus, Accessed on: 27.11.2022.

[39] Georgi Hristov Yordanov et al.; “Over-Irradiance (Cloud Enhancement) Events at High Latitudes”; IEEE, Leuven (Belgium) [2012]; DOI: http://dx.doi.org/10.1109/PVSC-Vol2.2012.6656797

[40] CAMPBELL SCIENTIFIC; “RSR2-KIT - Rotating Shadowband Radiometer”; CAMPBELL SCIENTIFIC; [Online] source is available at: https://www.campbellsci.asia/rsr2-kit, Accessed on: 27.11.2022.

[41] Norbert Geuder et al.; “Corrections for rotating shadowband pyranometers for solar resource assessment”; SPIE, Tabernas (Spain) [2008]; DOI: https://doi.org/10.1117/12.797472

[42] Norbert Geuder et al.; “Comparison of Corrections and Calibration Procedures for Rotating Shadowband Irradiance Sensors”; SolarPACES, Almería (Spain) [2008]

[43] CSP Services GmbH; “Rotating Shadowband Irradiometer CSPS Twin-RSI”; Cologne (Germany) [Yr. Unk.]; Available as PDF: https://www.cspservices.de/wp-content/uploads/Folleto_Twin_RSI.pdf, Accessed on: 02.02.2023

[44] Inc. Yankee Environmental Systems; “Thermopile Shadowband Radiometer Model TSR-1”; Montague (USA) [2009]; Available as PDF: http://windup.pt/resources/Tsr-1ds.pdf, Accessed on: 02.02.2023

[45] Rafal Broda; “Development of A Machine-Learning-Based Correction for Cloud-Camera-Based Solar Radiation Measurement”; Almería (Spain) [2022]; (Work is not published yet)

[46] CIEMAT; “SSPS-CRS” [2022]; [Online] source is available at: https://www.psa.es/es/instalaciones/receptor_central/crs.php, Accessed on: 19.01.2023.

[47] György Major; “Circumsolar Correction for Pyrheliometers and Diffusometers”; World Meteorological Organization, Budapest (Hungary) [1994]

[48] Niklas Benedikt Blum et al.; "DiffNI Documentation"; DLR, Tabernas (Spain) [2022]; (Work is not published yet)

[49] Norbert Geuder et al.; "MDMS Operation Maintenance Manual"; CSP Services GmbH), Köln (Germany) [2014]

[50] Norbert Geuder et al.; "Screening and flagging of solar irradiation and ancillary meteorological data"; Energy Procedia, Almería (Spain) [2014]; DOI: https://doi.org/10.1016/j.egypro.2015.03.205

[51] Sandia National Laboratories and pvlib python Development Team; "pvlib python" [2021]; [Online] source is available at: https://pvlib-python.readthedocs.io/en/stable/, Accessed on: 29.12.2022.

[52] Sandia National Laboratories and pvlib python Development Team; "pvlib.solarposition.getsolarposition" [2021]; [Online] source is available at: https://pvlib-python.readthedocs.io/en/v0.4.3/generated/pvlib.solarposition.get_solarposition.html, Accessed on: 29.12.2022.

[53] Bijan Nouri et al.; "Real-Time Uncertainty Specification of All Sky Imager Derived Irradiance Nowcasts"; Remote Sensing, Almería (Spain) [2019]; DOI: http://dx.doi.org/10.3390/rs11091059

[54] Markus Kottek et al.; "World Map of the Köppen-Geiger climate classification updated"; Gebrüder Borntraeger, Berlin (Germany) [2006]; DOI: https://doi.org/10.1127/0941-2948/2006/0130

[55] T. Chai and R.R. Draxler; Root mean square error (RMSE) or mean absolute error (MAE)? – Arguments against avoiding RMSE in the literature; NOAA Center for Weather and Climate Prediction, College Park (USA) [2014]

[56] The World Bank Group; "Global Solar Atlas" [2022]; [Online] source is available at: https://globalsolaratlas.info, Accessed on: 29.12.2022.

[57] Yankee Environmental Systems; "Automatic Total Sky Imager Model TSI-880"; Yankee Environmental Systems [2004]; [Online] source is available at: https://www.yesinc.com/index.php/products/sky-imaging, Accessed on: 22.01.2023.

[58] Joint Committee for Guides in Metrology (JCGM); "JCGM 100:2008 - Evaluation of measurement data — Guide to the expression of uncertainty in measurement"; JCGM, Sèvres (France); 2^{nd} edition [2008]

[59] Richard Hogan; "Type A and B Uncertainty - Guide to Evaluate Uncertainty Components" [2017]; [Online] source is available at: https://www.isobudgets.com/type-a-and-type-b-uncertainty/#:~:text=Difference%20Between%20Type%20A%20and%20Type%20B%20Uncertainty,-There%20is%20a&text=Type%20A%20uncertainty%20is%20evaluated,not%20how%20it%20is%20evaluated, Accessed on: 25.01.2023.

[60] Rebecca Roy; "Lambacher Schweizer Kursstufe"; Ernst Klett Verlag GmbH, Stuttgart (Deutschland) [2022]; ISBN: 978-3-12-735310-5, Available as PDF: https://www.klett.de/inhalt/media_fast_path/32/735310_Stochastik_Normalverteilung_und_Sigma_Regeln.pdf, Accessed on: 02.02.2023

[61] Suleyman Demir; "Comparison of Normality Tests in Terms of Sample Sizes under Different Skewness and Kurtosis Coefficients"; IJATE, Sakarya (Turkey) [2022]; DOI: https://doi.org/10.21449/ijate.1101295

[62] The SciPy community; "scipy.stats.skew" [2022]; [Online] source is available at: https://docs.scipy.org/doc/scipy/reference/generated/scipy.stats.skew.html, Accessed on: 03.01.2022.

[63] The SciPy community; "scipy.stats.kurtosis" [2022]; [Online] source is available at: https://docs.scipy.org/doc/scipy/reference/generated/scipy.stats.kurtosis.html, Accessed on: 03.01.2022.

[64] Iain Weir; "Spearman's correlation"; statstutor, Loughborough (England) [Yr. Unk.]; Available as PDF: https://www.statstutor.ac.uk/resources/uploaded/spearmans.pdf, Accessed on: 02.02.2023

[65] Joost C.F. De Winter; S. D. Gosling and J.P. Potter; "Comparing the Pearson and Spearman correlation coefficients across distributions and sample sizes. A tutorial using simulations and empirical data"; American Psychological Association, Delft (Netherlands) [2014]; DOI: http://dx.doi.org/10.1037/met0000079

[66] Jacob Cohen; "Statistical Power Analysis for the Behavioral Sciences"; LAWRENCE ERLBAUM ASSOCIATES, New York (USA); 2^{nd} edition [1988]; ISBN: 0-8058-0283-5

[67] NumPy Developers; "numpy.polyfit" [2022]; [Online] source is available at: `https: //numpy.org/doc/stable/reference/generated/numpy.polyfit.html`, Accessed on: 29.12.2022.

[68] Stefan Wilbert; David Schüler and Laurent Vuilleumier; "Direct Normal Irradiance Nowcasting methods for optimized operation of concentrating solar technologies"; DNICast, Addr. Unk. [2015]; Grant agreement ID: 608623

[69] R. Giles Harrison; "Meteorological Measurements and Instrumentation"; John Wiley Sons, Ltd, Chichester (England); 1^{st} edition [2015]; ISBN: 9781118745809

[70] Hukseflux Thermal Sensors BV; "What are pyranometer offsets?"; Hukseflux Thermal Sensors BV, Delft (Netherlands) [2006]

[71] Illuminating Engineering Society (IES); "ANSI-IES LS-1-22, Lighting Science: Nomenclature and Definitions for Illuminating Engineering"; IES, New York (USA) [2021]; [Online] source is available at: `https://www.ies.org/definitions/lamberts-cosine-law`, Accessed on: 13.11.2022.

[72] S.R Wilcox and D.R Myers; "Evaluation of Radiometers in FullTime Use at the National Renewable Energy Laboratory Solar Radiation Research Laboratory"; National Renewable Energy Laboratory, Golden (USA) [2008]; Technical Report: NREL/TP-550-44627

[73] Glyn A. Holton; "Value-at-Risk Theory and Practice"; Academic Press, Amsterdam (Netherlands); 2^{nd} edition [2013]; ISBN: 0-12-354010-0

[74] John Clayton Rawlings; "Basic AC Circuits"; Newnes, Addr. Unk.; 2^{nd} edition [2000]; DOI: `https://doi.org/10.1016/B978-075067173-6/50003-1`